Single molecule experiments on DNA with novel silicon nanostructures

Cover image

DNA molecule between two platinum electrodes spaced by 40 nm on silicon oxide. The three-dimensional view was rendered from the Atomic Force Microscope (AFM) image shown in Fig. 6.2a at page 87.

Single molecule experiments on DNA with novel silicon nanostructures

P R O E F S C H R I F T

ter verkrijging van de graad van doctor
aan de Technische Universiteit Delft,
op gezag van de Rector Magnificus prof.dr.ir. J.T. Fokkema,
voorzitter van het College voor Promoties,
in het openbaar te verdedigen
op maandag 17 mei 2004 om 10:30 uur

door

Arnoldus Jan STORM

doctorandus in de natuurkunde,
geboren te Groenlo.

Dit proefschrift is goedgekeurd door de promotor:
Prof.dr. C. Dekker

Samenstelling van de promotiecommissie:

Rector Magnificus	Voorzitter
Prof.dr. C. Dekker	Technische Universiteit Delft, promotor
Prof.dr. J.A. Golovchenko	Harvard University, Verenigde Staten
Prof.dr. P.H. Kes	Universiteit Leiden
Prof.dr.ir. J.E. Mooij	Technische Universiteit Delft
Prof.dr.ir. W. van Saarloos	Universiteit Leiden
Prof.dr. S. de Vries	Technische Universiteit Delft
Prof.dr. H.W. Zandbergen	Technische Universiteit Delft

Het onderzoek beschreven in dit proefschrift is mede gefinancierd door de stichting voor Fundamenteel Onderzoek der Materie (FOM).

Published and distributed by: DUP Science

DUP Science is an imprint of
Delft University Press
P.O. Box 98
2600 MG Delft
The Netherlands
Telephone: +31 15 2785678
Telefax: +31 15 2785706
E-mail: info@library.tudelft.nl

ISBN: 90-407-2485-7

Keywords: Nanotechnology, nanopore, DNA

Printed in the Netherlands.

Table of contents

Table of contents **v**

1 Introduction and outline **1**
1.1 Nanotechnology 1
1.2 The structure and function of DNA 3
1.3 Theme 1: DNA threading through small pores 5
1.4 Theme 2: Electronic properties of DNA 6
1.5 Theme 3: Electrochemistry at the nanometer scale . . 8
1.6 Outline of this thesis 8

2 Fabrication of solid-state nanopores with single-nanometer precision **11**
2.1 Fabrication 12
2.2 Results 12
2.3 Surface tension model 16
2.4 Discussion and conclusions 18

3 Electron-beam-induced deformations of SiO_2 nanostructures **21**
3.1 Introduction 22
3.2 Materials and methods 23
3.2.1 Fabrication of silicon oxide nanostructures . . . 23
3.2.2 Electron microscopy 27
3.3 Results 27
3.3.1 Geometry of fabricated structures before modification 28
3.3.2 TEM-induced shape changes of rectangular pores 30

3.3.3 Direct observation of the 'critical size' 30
3.3.4 Deforming a narrow slit 35
3.3.5 Elemental analysis on deforming pores 36
3.4 Discussion 39
3.5 Conclusion 41

4 Translocation of double-strand DNA through a silicon oxide nanopore 43
4.1 Introduction 44
4.2 Materials and methods 46
4.2.1 Fabrication of solid-state nanopores 46
4.2.2 DNA material 47
4.2.3 Experimental set-up and techniques for DNA translocation experiments 47
4.2.4 Analysis of translocation events 50
4.3 Results 55
4.3.1 Translocation of linear ds-DNA 55
4.3.2 Influence of the voltage driving the translocation 62
4.3.3 Circular DNA translocation events 64
4.3.4 Nanopore experiment on a polydisperse DNA mixture 64
4.4 Discussion 66
4.5 Conclusions 69

5 Fast DNA translocation through a solid-state nanopore 71
5.1 Introduction 72
5.2 Experimental results 72
5.3 Slow versus fast translocations 74
5.4 Prior work on slow translocations 76
5.5 Fast translocations 77
5.6 Model 77
5.7 Concluding remarks 80

6 Insulating behavior for DNA molecules between nanoelectrodes at the 100 nm length scale 83
6.1 Introduction 84
6.2 Experiments and results 84
6.3 Conclusions 89

7 Electrochemistry at lithographically fabricated nanometer-scale electrodes 91
7.1 Introduction 92
7.2 Materials and methods 93
7.2.1 Electrode fabrication 93
7.2.2 Chemicals 96
7.2.3 Electrochemical apparatus 97
7.3 Results and discussion 98
7.3.1 Scanning electron microscopy 98
7.3.2 Steady-state cyclic voltammetry 99
7.3.3 Theoretical determination of the limiting current 101
7.4 Conclusions 105

Bibliography 107

Summary 111

Samenvatting 115

Nawoord 119

List of publications 123

Curriculum vitae 125

Chapter 1

Introduction and outline

> "There is already one highly successful nanotechnological system: We call it life. All the goals of nanotechnology are already fulfilled in living systems, and most of our attempts at nanotechnological applications can be called biomimetic, either applying the structural principles of living systems to different compounds or using the compounds of living systems for different purposes."
>
> *Nadrian C. Seeman, New York University*

1.1 Nanotechnology

Nanotechnology can be defined as the development and use of devices that have a characteristic size of only a few nanometers. The ultimate goal is to fabricate devices that have every atom in the right place. Such technology would give the opportunity to minimize the size of a device and to reduce the material, energy and time necessary to perform its task. Potential applications include electrical circuits, mechanical devices and medical instruments. Molecular biology is a source of inspiration in this field of research: Living cells can synthesize a wide variety of macromolecules with atomic precision, that all have a specific function in the cell. This can be considered as the proof that there are no physical laws that forbid the construction of structures with atomic precision.

Essentially, there are two approaches towards the fabrication of structures at or near the atomic level: The first is the 'top down' approach where the precision of existing macroscopic techniques is improved. This concept has been demonstrated in semiconductor industry, where lithographic processes are nowadays used to make integrated circuits with critical dimensions smaller than 100 nm. This precision will be improved further, but true atomic precision can not be obtained with this approach. The second 'bottom up' approach strives to build structures using atoms or molecules as building blocks. Most striking are experiments where individual atoms are positioned on an atomically flat substrate using scanning-probe techniques. Patterns of atoms have even been demonstrated to act as simple logic gates. Such scanning-probe techniques however are not very practical: Assembly by placing a single atom at a time is a very time-consuming process.

A particularly interesting 'bottom up' approach is to assemble structures from molecular building blocks. Using synthetic chemistry, large amounts of identical building blocks can be obtained at low cost. One of the most promising ideas is to use building blocks from living systems: The advantages are that these molecules are intensively studied and that they can be synthesized with atomic precision. Moreover, DNA building blocks have been used to assemble three-dimensional structures from small synthetic building blocks.

This thesis describes experiments where we use silicon nanotechnology to address the physical properties of individual molecules. A first set of experiments probes the polymer dynamics of DNA threading through small pores. In order to fabricate holes with a diameter on the order of the diameter of DNA we have developed a new technique to controllably shrink larger silicon oxide pores with direct visual feedback. We have also addressed the question whether a single DNA molecule can carry an electrical current. This is an important issue for potential DNA-based electronics. The last topic is electrochemistry using nanometer-scale electrodes, fabricated using silicon processing. A standing goal is to develop the technology to perform electrochemical experiments on a single molecule. After a short review of the properties of DNA we give a short introduction to the three research subjects of this thesis.

1.2 The structure and function of DNA

Most experiments in this thesis are performed on DeoxyriboNucleic Acid (DNA). This section contains a brief review of the relevant properties of this unique molecule. The structure and function have been intensively studied and the basics can be found in many biological textbooks (See for example Ref. [1]). In Fig. 1.1a the chemical structure is shown schematically for a small piece of double-strand DNA. It consists of two polymer chains. Each monomer consists of a sugar ring, a phosphate group, and one of the four bases Adenine (A), Guanine (G), Thymine (T) or Cytosine (C). Watson and Crick [2] were the first to determine the double-helical structure of DNA. They found that DNA consists of two strands, running anti-parallel. On the outside are the sugar-phosphate chains, also known as the 'backbone' of the molecule. On the inside of the helix are the bases, occurring in specific pairs: Adenine (A) specifically binds to Thymine (T) and Guanine (G) to Cytosine (C). From X-ray diffraction experiments on fibers of DNA, Watson and Crick were able to deduce the double helical structure depicted in Fig. 1.1b.

The structure as reported by Watson and Crick became known as the 'B-DNA' helix. The diameter is about 2 nm and the distance between two bases is 0.34 nm. Each 10.4 bases or 3.6 nm, DNA makes a full helical turn. The structure is stabilized by the base-specific hydrogen bonds between the strands and the hydrophobic interactions between adjacent bases. This B-DNA helix is the structure for DNA with a mixed sequence at physiological conditions. It should be noted that these properties are averaged over many subunits, and that the structure can vary with temperature, buffer conditions and the local sequence of bases. An intriguing property of double-strand DNA is its moderate flexibility: It can be smoothly bent or twisted with very little influence on the helical properties. An important property for our work is the fact that DNA in solution is highly charged at neutral pH. Each phosphate group on the backbone has a negative charge, resulting in a linear charge density of 5.9 e^- per nanometer. The effective charge density however is considerably lower due to counterion condensation [3, 4].

The function of DNA is to carry genetic information. The information contained in the base-pair sequence can be transcribed to messenger ribonucelic acid (RNA), which is then used to synthesize

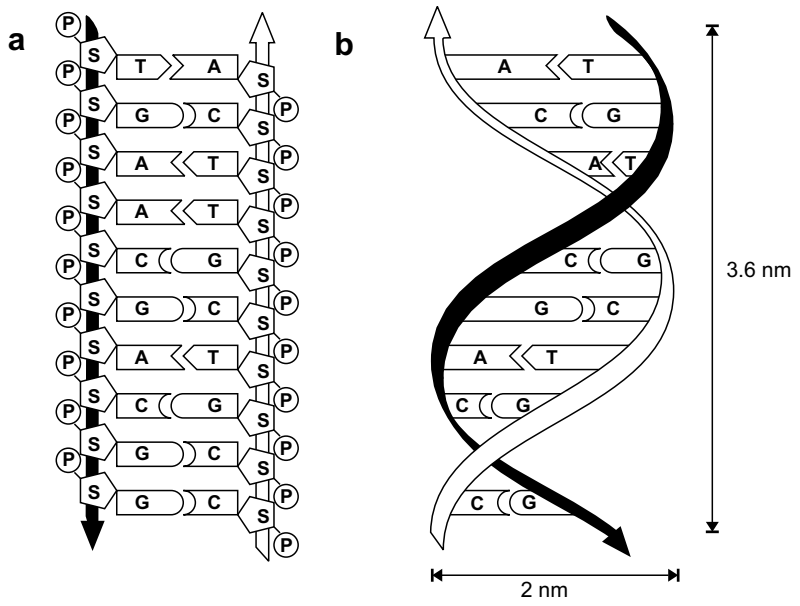

Figure 1.1: Schematic structure of double-strand DNA. (a) A double-strand DNA molecule consists of two polymer strands running anti-parallel. The pentagons labeled with an 'S' denote the sugar rings and the 'P'-labeled circles are negatively-charged phosphate groups. One of the four bases (Adenine, Thymine, Guanine or Cytosine) is attached to each sugar. The genetic information is carried in the sequence of these four bases in the molecule. (b) Double-helical structure of double-strand DNA. It forms a polymer with a diameter of about 2 nm and contains one full helical turn for each 3.6 nm or 10.4 base pairs.

functional proteins by the ribosome of the cell. During cell division, the two strands of DNA separate, and each acts as a template for a newly synthesized DNA strand, based on the specific base-pairing properties. This process duplicates a DNA molecule including all the information contained in the sequence of bases.

1.3 Theme 1: DNA threading through small pores

The driven transport of DNA through nanometer-sized pores (nanopores) in a fluid is the main subject of this thesis. It is a complex process that involves hydrodynamic and electrostatic effects in addition to polymer physics. The primary motivation is a better understanding of the physics underlying biopolymer translocation through pores in vivo. Examples are the transport of messenger RNA through the nuclear pore complex, the injection of viral DNA into cells and the import of DNA for gene therapy. A secondary motivation is to explore the potential of nanopores for the analysis of DNA.

Recently, nanopore-based detectors have attracted considerable attention. They can be considered as a Coulter counter at the nanometer scale. A Coulter counter consists of a channel of typically a few microns in diameter. Particles flowing through the channel reduce the conductivity between the reservoirs and this effect can be used to determine the size distribution of the suspended particles. A nanopore detector employs essentially the same mechanism, but uses an aperture small enough to detect individual macro-molecules in solution.

The first experiment on forced translocations of nucleic acids were carried out by Kasianowicz, Brandin, Branton and Deamer [5]. They proved that single-strand DNA and RNA molecules can be driven through the α-hemolysin protein complex incorporated in a lipid membrane, see Fig. 1.2 for a typical setup for such experiments. The highly charged polymers were pulled through the pore by an externally applied electric field. The passages of molecules are detected as short depressions of the ionic current flowing through the pore. Thus by a simple measurement of the ionic current through the system, one can detect the molecules entering and leaving the pore one by one, see Fig. 1.3. This has become an active field of research, studying

the dynamics of the process at the single-molecule level as a function temperature, concentration, polymer length, and base sequence. The observation that the dynamics of the process depends strongly on the base sequence has led to the speculation that nanopores can be used to sequence DNA, i.e. determine the exact base sequence of a DNA molecule.

1.4 Theme 2: Electronic properties of DNA

The 3D structure of DNA has been resolved some 50 years ago by Watson and Crick [2]. Its electronic properties however are still under considerable debate. In particular the question whether a DNA molecule can carry an electrical current has been addressed in a number of experimental and theoretical works. A number of reasons for the particular interest in DNA can be identified:

1. It has been suggested that overlap between π-orbitals from adjacent bases could lead to a delocalization of electrons over considerable length [7]. This could provide a pathway for electron transport along the DNA chain.

2. The specific base-pairing properties can be used to synthesize structures much more complex than a linear polymer. A synthetic DNA cube synthesized by Seeman *et al.* [8] is just an example. Clever use of DNA synthesis, hybridization and purification can in principle lead to complex three-dimensional networks of DNA. Combined with suitable electronic properties, this could lead to functional electronic devices that are built bottom-up from small molecular building blocks.

3. DNA molecules can be synthesized using readily available technologies developed for microbiological applications.

4. A large library of DNA modification enzymes is available, that can be used for sequence-specific restriction and ligation of molecules.

First reports of a high electron mobility were reported by Barton *et al.* [9]. In this experiment electron donor and acceptor groups

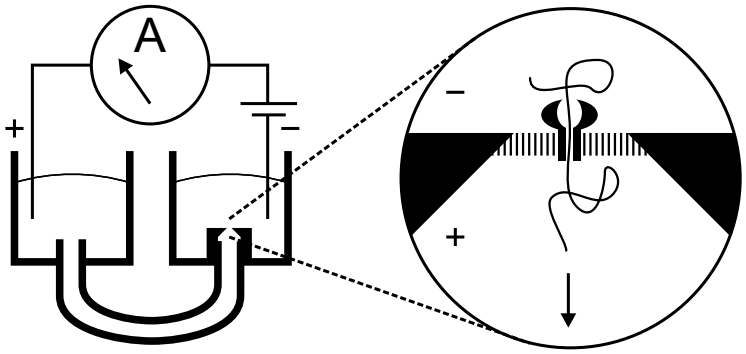

Figure 1.2: Example of a setup for translocation experiments on single-strand DNA through an α-hemolysin pore. The picture is adapted from Ref. [6].

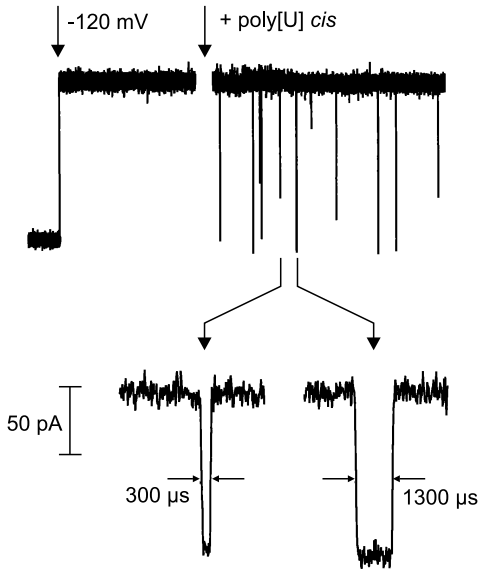

Figure 1.3: Ionic current versus time measured in a nanopore experiment. In the top panel a measurement is shown before and after the addition of the poly(U) RNA molecules. Clearly short blockades of the current are observed in the presence of the RNA. Two blockades are shown with an increased time resolution at the bottom. This picture is reproduced from Ref. [5] by Kasianowicz *et al.*

were attached to DNA molecules. Fluorescence experiments were performed on molecules in solution. In the absence of an electron acceptor group, the donor shows fluorescence after absorption of a photon. If there is the possibility of electron transfer from the donor to acceptor, no fluorescence is observed. Based on the observed quenching of fluorescence, it was concluded that electron transfer is mediated by the double-strand DNA over a length of several nanometers.

Inspired by this claim a number of electron-transport experiments were performed to determine the properties of dry DNA molecules on larger length scales, using a range of techniques. Results from experiments on the conductivity of DNA however varied drastically: Reported values for the conductivity of a single DNA molecule range from 300 kΩ [10] to 10^{16} Ω [11], a difference of more than 11 orders of magnitude! Even more intriguingly, Kasumov *et al.* [10] reported supercurrents carried by a DNA molecule at temperatures below 1 K.

1.5 Theme 3: Electrochemistry at the nanometer scale

Cyclic voltammetry is an analytical technique to study electrochemically active molecules. Miniaturization of the electrodes can extend its capabilities: With electrodes on the nanometer scale, one can reach shorter equilibration times and can study the kinetics at the electrode. So far, electrodes have been fabricated by partially coating a sharp metal tip with an insulator. The diffusion of molecules towards and away from the electrode is an important process that depends critically on the geometry of the electrode. The geometry of the electrode and surrounding insulator however, is largely unknown in the experiments performed with coated tips. A standing goal in electrochemistry is to sufficiently reduce the size of the electrode to study the electrochemical activity of a single molecule. Of particular interest here are redox proteins such as cytochrome-c.

1.6 Outline of this thesis

In **chapter 2** we report a new technique for the fabrication of nanometer-sized pores, with single-nanometer precision. We show that a transmission electron microscope can be used to shrink silicon

oxide pores with a starting size between 20 nm and 50 nm to any desired dimension. The process takes place during imaging and changes of the pore can be followed in real-time at sub-nanometer resolution. When the pore has shrunk to its desired diameter, the electron-beam is blanked and the process stops. The underlying mechanism is that the high-dose electron beam induces a fluidized state. The molten silicon oxide deforms under its surface tension resulting in the tightening of sufficiently small apertures.

Chapter 3 gives a more extensive description of the characterization of nanopores. A set of electron-beam deformation experiments is performed on pores with various initial dimensions. The results confirm the proposed mechanism for nanopore deformation discussed in chapter 2. Additionally, we discuss analysis on the composition of our devices. We show that we indeed observe structural deformations and not addition or removal of material in our experiments. Finally, we extend the surface-tension model to explain the evolution of various apertures irradiated by the electron microscope in more detail.

In **chapter 4** we present translocation experiments on DNA through silicon oxide nanopores. We have studied molecules with a contour length between 0.7 μm and 16.5 μm. We report that the DNA molecules can pass the 10 nm wide pore in a number of configurations: Besides linear end-to-end translocations, we observe the translocation of molecules in a folded state. We demonstrate the potential of solid-state nanopores for the DNA sizing: A nanopore experiment with a mixture of DNA molecules with lengths in the range of 0.7 μm to 9.3 μm shows that its composition can be determined from the statistics of the observed translocations. We conclude that the translocation time of DNA molecules scales with the length in a non-linear fashion.

In **chapter 5** we present a new scaling model for driven polymer translocation. Based on well-known principles in polymer physics, we derive a power-law scaling between the translocation time and polymer length. The exponent we find from this model agrees well with the experiments of chapter 4.

Chapter 6 presents experiments probing the electrical transport properties of individual DNA molecules. We used nanofabricated electrodes with various spacings on a planar substrate and subse-

quently deposited various types of DNA. This approach allowed imaging of the device to prove the presence of DNA between the electrodes. A number of experimental parameters were varied: substrate type (SiO_2 and mica), electrode material (gold and platinum) and applied gate voltage. None of our devices showed any sign of DNA conductance at the 100 nm length scale.

In **chapter 7** we show that SiO_2 nanopores between 15 nm and 100 nm can be used for the fabrication of well-defined electrodes for electrochemistry. We present cyclic-voltammetry curves obtained on such devices to determine their diffusion-limited current. The size-dependence of the limiting current can be understood with simulations that take the precise geometry of our electrodes into account.

CHAPTER 2

Fabrication of solid-state nanopores with single-nanometer precision

Abstract

Single nanometer-sized pores (nanopores) embedded in an insulating membrane are an exciting new class of nanosensors for rapid electrical detection and characterization of biomolecules. Notable examples include α-hemolysin protein nanopores in lipid membranes [5, 12], and solid-state nanopores in Si_3N_4 [13]. Here we report a new technique for fabricating silicon oxide nanopores with single-nanometer precision and direct visual feedback, using state-of-the-art silicon technology and transmission electron microscopy. First, a pore of 20 nm is opened in a silicon membrane by using electron-beam lithography and anisotropic etching. After thermal oxidation, the pore can be reduced to single nanometer dimension when it is exposed to a high-energy electron beam. This fluidizes the silicon oxide leading to a shrinking of the small hole due to surface tension. When the electron beam is switched off, the material quenches and retains its shape. This technique dramatically increases the level of control in the fabrication of a wide range of nano devices.[1]

[1]This chapter has been published in Nature Materials:
A. J. Storm, J. H. Chen, X. S. Ling, H. W. Zandbergen, and C. Dekker *Fabrication of solid-state nanopores with single-nanometre precision.* Nature Mat. **2** 537 (2003).

2.1 Fabrication

The fabrication of our 20 nm to 200 nm pores in silicon oxide builds upon earlier work [14] by Gribov *et al.* Silicon-On-Insulator (SOI) wafers with a top single-crystal silicon layer of 340 nm with crystal orientation $\langle 100 \rangle$ were used to fabricate 70×70 μm^2 free-standing silicon membranes, using micromachining techniques. The membranes are thermally oxidized on both sides with a SiO_2 layer of 40 nm thickness. Using electron-beam lithography and reactive-ion etching we open squares with dimensions up to 500 nm in the SiO_2 mask layer at the top. Subsequently, pyramid-shaped holes are etched using anisotropic KOH wet etching. Stripping the 40 nm oxide in buffered hydrogen fluoric acid opens up the pore in the silicon membrane (see Fig. 2.1a). The last processing step is a thermal oxidation to form a SiO_2 surface layer with a thickness of 40 nm. Fig. 2.1b shows a top-view scanning electron micrograph (from a Philips/FEI XL30s SEM) of the pore after the fabrication process. Each device used in the experiments reported in this chapter contains a silicon membrane with up to 400 pyramid shaped holes with various dimensions, from closed to pores of about 200 nm.

2.2 Results

In this chapter we report a new technique to fine-tune the size of pores with nanometer precision. Our main tool here is a commercial transmission electron microscope (TEM), a Philips CM-30UT operated at an accelerating voltage of 300 kV. It is well known in electron microscopy that a high electron intensity can damage or deform the specimen, and in general one tries to minimize this effect. However, we use this effect to modify the dimensions of our silicon oxide nanopores in a well-controlled way. Fig. 2.1c shows a cross-sectional view of a nanofabricated pore in the microscope. We found that an electron beam of intensity around 10^5 to 10^7 Am^{-2} causes pores to shrink if the pore had an initial diameter of about 50 nm or lower. Remarkably, different dynamics were found for pores with initial dimensions of about 80 nm or higher. These pores expand in size instead of the shrinking dynamics observed for small pores. The changes in pore diameter can be monitored in real-time using the

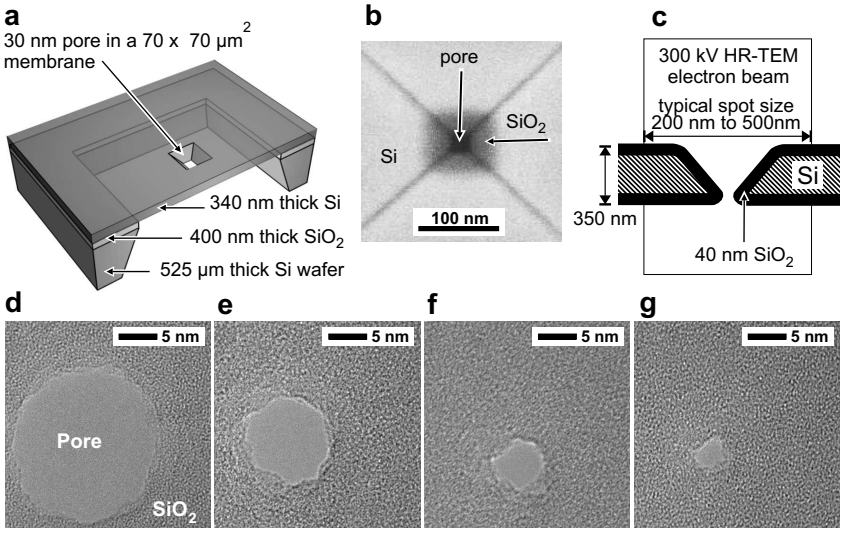

Figure 2.1: Fabrication of silicon oxide nanometer-sized pores. (a) Cross-sectional view of our device. It consists of a 340 nm thick free-standing single-crystalline silicon membrane, supported by a KOH etched wafer 525 μm thick. The membrane contains one or more sub-micrometer, pyramid-shaped pores, anisotropically etched with KOH from the top. (b) Top-view scanning electron micrograph of a nanofabricated pore after thermal oxidation. The pore is about 20×20 nm^2, and is surrounded by a SiO_2 layer of about 40 nm thickness. (c) Cross-sectional view of the pore inside the electron microscope. (d-g). Sequence of micrographs obtained during imaging of a SiO_2 pore in a TEM microscope. The electron irradiation causes the pore to shrink gradually to a size of about 3 nm.

imaging mechanism of the microscope. Figs. 2.1d-g show a sequence of images obtained while imaging a pore with an initial diameter of 19 nm. The surprising effect of growing and shrinking pores can be understood from surface tension effects in the viscous silicon oxide, as discussed below.

The hole closing reported in this chapter is certainly not caused by deposition of carbon-rich material by the electron beam, a common phenomenon in electron microscopy. The observation that large pores expand is in direct contradiction with potential contamination growth. Secondly, electron energy loss spectra (EELS) locally obtained on the material that filled a nanopore clearly show the presence of silicon and oxygen, but the absence of any carbon (detection limit was less than 2 %).

The power of our technique lies in the possibility of fine-tuning the diameter of nanopores with unprecedented precision. By lowering the beam intensity or blanking it, the shrinking process can be stopped within seconds when the desired diameter has been reached. Fig. 2.2 shows the average diameter of the pore versus time. In this experiment the diameter of the pore shrinks at a rate of about 0.3 nm per minute, slow enough to stop at any desired dimension. If favored, coarse shrinking can be done at least an order of magnitude faster by increasing the electron intensity, and can gradually be slowed down for ultimate control. The final precision is limited by the resolution of the microscope (0.2 nm for ours). In practice the resolution is limited to about 1 nm due to the surface roughness of the silicon oxide. The level of control is at least an order of magnitude better than conventional electron-beam lithography, which has an ultimate resolution of about 10 nm. Our technique drastically limits the required dimensional control in the prior lithographic process, because any pore with a diameter below 50 nm can be shrunk to a nanometer-sized pore. The fabricated pores were found to be stable at ambient conditions and in water.

The pore-size tuning technique was further tested on holes fabricated using a different process. In agreement with Chen *et al.* [15], we find that a focused electron beam with a spot size of a few nanometers can be used to drill holes in thin free-standing SiO_2 membranes, with an estimated thickness of about 10 nm (Fig. 2.3a). Figs. 2.3b and 2.3c show a pore that has been drilled using an electron beam

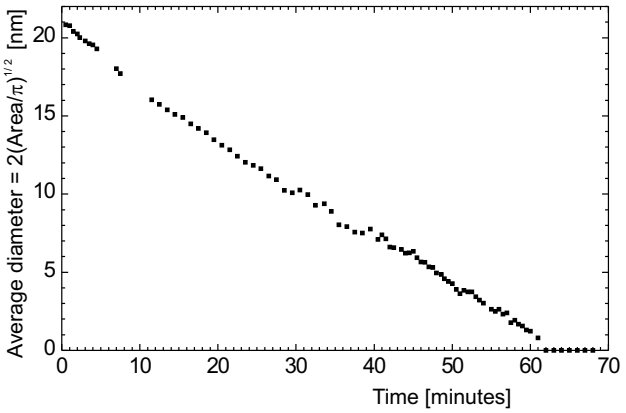

Figure 2.2: Diameter versus time for a shrinking pore with an initial size of about 21 nm. A sequence of TEM micrographs was obtained using a charge-coupled device (CCD) camera during continuous electron irradiation at constant intensity and focus setting. From each image we estimated the area from a polygon tracing the perimeter of the pore. This area was used to calculate the diameter of the pore assuming a circular shape. The absolute error in this measurement is estimated to be 1 nm, which, to a large extent is due to the width of the diffraction ring around the perimeter of the pore.

intensity above $1{\cdot}10^8$ Am^{-2}. Holes as small as 6 nm can be obtained, but this technique does not give full control at the nanometer scale because no images can be recorded during drilling. It is however possible to subsequently fine-tune the size of the drilled pores using the same process as discussed earlier, if the diameter is small enough. As a demonstration, Figs. 2.3d-f shows a sequence of micrographs where a 6 nm pore is reduced down to 2 nm. At the high exposure levels necessary for drilling the hole, the oxygen content of the silicon oxide irradiated by the electrons was strongly reduced [16]. Energy-dispersive X-ray (EDX) analysis shows up to 80 % oxygen depletion during hole drilling. It should be noted that the irradiation levels needed for the controlled pore shrinking are about a factor 100 lower than those used for the hole drilling. EDX experiments at these lower intensities show oxygen depletion rates of less than 10 % per hour.

The effect of electron irradiation at intensities between 10^5 and 10^7 Am^{-2} on amorphous SiO_2 has not yet received much attention. Based on the apparent morphological changes in our nanostructures on imaging, and the absence of changes in the composition of the irradiated material, we conclude that at these electron irradiation levels viscous flow is induced in the amorphous silicon oxide, in agreement with observations by Ajayan and Iijima [17]. Whereas the electron beam clearly provides the energy to soften the material, direct specimen heating alone does not explain the effect [17]. At intensities above 10^7 Am^{-2} another mechanism dominates and oxygen is preferentially lost from the silicon oxide. Radiation with an electron beam focused to a spot of a few nanometers leads to formation of pure silicon structures at the nanometer scale [16], and prolonged irradiation eventually leads to the formation of a hole in thin films [15].

2.3 Surface tension model

The physics of the observed growing and shrinking of nanopores is determined by the surface tension of the viscous silicon oxide. In the fluidized state, the structure will deform to find a configuration with a lower free energy F. For simplicity we model our pore as cylindrical with radius r in a sheet of material with constant thickness h, see Fig. 2.4a. The change in free energy compared with an intact sheet is $\Delta F = \gamma \Delta A = 2\pi\gamma(rh - r^2)$, where γ is the surface tension of the

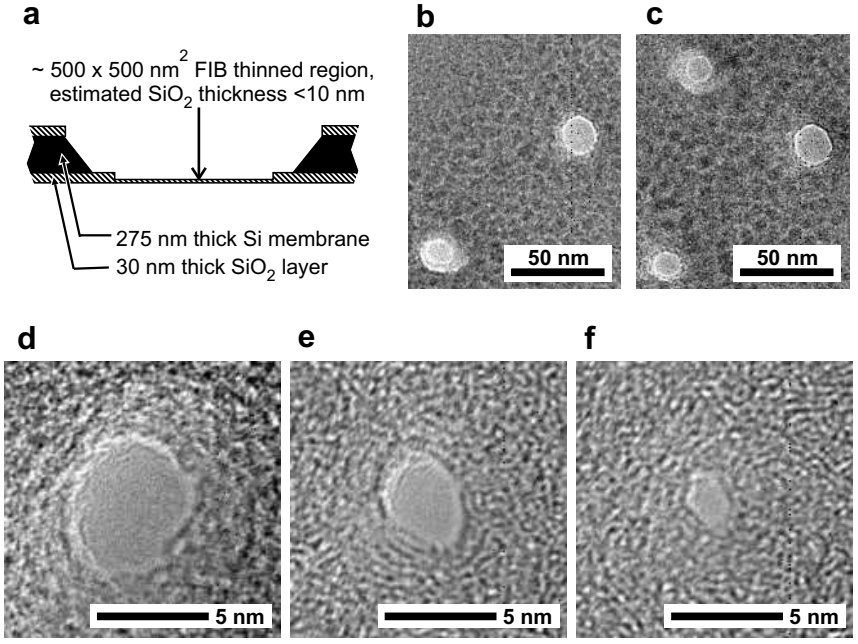

Figure 2.3: TEM-drilled nanopores in thin free-standing SiO_2 membranes. (a) Cross-section of a thin SiO_2 membrane within a silicon-based membrane. Fabrication of this structure starts with a bare silicon membrane, which is oxidized with about 30 nm of SiO_2 on both sides. Using electron-beam lithography and reactive-ion etching we open up 1×1 μm^2 squares in the oxide layer. After a KOH wet etch, we obtain 30 nm thick SiO_2 membranes. Subsequently these were thinned further in a focused ion-beam (FIB, FEI Strata DB235) microscope, to a final estimated thickness of less than 10 nm. (b) TEM micrograph of a part of a membrane with two holes that were drilled by a finely focused electron beam inside the TEM microscope. (c) TEM micrograph after drilling a third hole in the membrane depicted in Fig. 2.3b. (d-f) Sequence of TEM images obtained on a shrinking nanopore with an initial diameter of about 6 nm and a final diameter of only 2 nm.

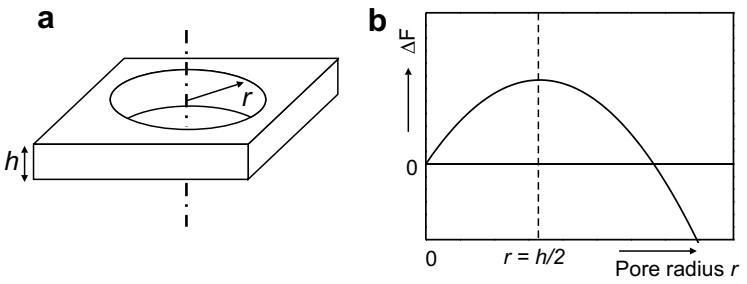

Figure 2.4: A model system explaining nanopore shrinking and expanding dynamics: (a) We model our system as a cylindrical pore with radius r in a sheet of liquid with thickness h. (b) Change of surface free energy on formation of a cylindrical pore in a liquid film. From the graph $\Delta F(r)$ can be seen that pores with radius $r < h/2$ can lower their surface free energy by reducing r, and pores with radius $r > h/2$ by increasing r.

liquid and ΔA is the change in surface area. From the graph $\Delta F(r)$ in Fig. 2.4b, it can be seen that pores with radius $r < h/2$ can lower their surface free energy by reducing r, whereas pores with radius $r > h/2$ do so by increasing size. The 'critical diameter' $2r$ discriminating the two cases is of order of the thickness of the sheet, with the exact value depending on the geometry of the pore. This scaling argument is valid at any scale, and elegantly explains the observed dynamics in our pores. We estimate that in our SOI pores the effective height of the pore is about 40 nm, the thickness of the silicon oxide layer, in good agreement with the observed 'critical diameter' between 50 nm and 80 nm in our experiments. In the experiments on holes in thin silicon oxide films, we observed a much lower critical diameter of around 10 nm, in agreement with the model.

2.4 Discussion and conclusions

Similar dynamics and interpretations were described by Taylor and Michael [18] for holes in films of mercury on the millimeter scale investigated by optical microscopy. Lanxner *et al.* [19] studied similar effects on nanometer sized holes in 20 nm thick crystalline gold

films, before and after annealing. Again the interpretation is surface-tension-driven mass flow. Direct comparison of our results to the TEM work of Ajayan and Iijima [17] shows that the deformation rate is a factor of 10 to 100 slower in our work, which is a striking difference because the material and radiation conditions are similar in both experiments. This apparent discrepancy can be explained from a consideration of the geometry. A curved liquid surface will generate a Laplace pressure inversely proportional to the radius of curvature. The tips described in Ref. [17] had a radius of curvature of the order of 1 nm, whereas our pores have a typical curvature of about 10 nm, leading to lower pressures and slower dynamics.

In summary we have demonstrated a new method to make solid-state nanopores with single-nanometer precision. The advantage of this technique is that nanometer-scale sample modifications are possible with direct visual feedback at sub nanometer resolution. The process is based on standard silicon processing and commercially available TEM microscopes. A modest resolution of about 50 nm is required in the lithography defining the pore, as fine tuning in the electron beam is done as a final step. Using the SOI-based process, it is straightforward to obtain this requirement with electron-beam lithography, and should be attainable even with optical lithography alone. A recent report [13] on 'ion beam sculpting' of nanopores showed for the first time a process for controlled fabrication of pores in silicon nitride, and demonstrated the potential of inorganic nanopores for DNA analysis on the single-molecule level. Our technique has the additional advantages of direct visual feedback as well as the fact that it does not change the chemical composition of the material surrounding the pore. In a way, our technique is like glassblowing at the nanoscale: We use the electron beam to soften the glassy silicon oxide, allowing it to deform slowly driven by the surface tension. The electron microscope provides real time visual feedback, and when the desired morphology has been obtained the electron beam intensity is lowered and the silicon oxide is quenched to its initial glassy state. This technique can greatly increase the level of control in a wide range of nanotechnological applications: nanopore devices for biomolecular analysis, metallic point contacts and electrodes for molecular electronics.

Chapter 3

Electron-beam-induced deformations of SiO_2 nanostructures

Abstract

It was recently found that the electron beam of an electron microscope can induce modifications to nanostructures. This new technique is particularly useful for the fabrication of nanopores with single-nanometer precision, down to 2 nm. Here we study this technique in more detail by irradiation of apertures with various geometries. We test the hypothesis that surface-tension effects drive the modifications. We show that pores that are smaller than a certain critical size shrink and that larger ones expand, in good agreement with the hypothesis. Additionally, we have determined the composition of our devices before and after modifications and find no significant changes. This result proves that contamination growth is not the underlying mechanism of pore closure.

3.1 Introduction

In chapter 2 we have described a new technique for the fabrication of well-defined nanopores in silicon oxide. There, we report the fabrication of pores with an initial diameter between 20 nm and 50 nm using state-of-the-art lithography and etching techniques. Surprisingly, we found that such pores will shrink during imaging in a transmission electron microscope. By blanking the beam we could stop the process to obtain a high yield of round nanopores with a final diameter well below 10 nm, with an estimated precision of about 1 nm. We concluded that the electron beam fluidizes the silicon oxide material and that the surface tension drives the nanopore shrinking.

In this chapter we present a more detailed experimental study of deformations of silicon oxide nanostructures induced by and observed with a transmission electron microscope (TEM). We start with a detailed description of the fabrication process that we use to make the silicon oxide structures. An extensive set of experiments on nanopores with various geometries was performed to strengthen our conclusion that the surface tension of the fluidized silicon oxide drives the observed deformations.

The surface-tension model discussed in chapter 2 explains our main observations: Big pores grow and small pores shrink during electron irradiation. In this chapter we refine this model using *local* Laplace pressures generated at curved, liquid surfaces. We use this formalism to explain and understand the size and shape evolution of our nanopores in more detail.

Another important issue discussed here concerns possible changes in the chemical composition of the materials irradiated with the electron beam, which was only briefly mentioned in chapter 2. First, there is the risk that the electron beam promotes the deposition of carbon-rich material on the device, which could give rise to another mechanism for pore closure. A second effect concerns potential changes in the composition of the silicon oxide by the high-energy electrons bombarding it. To address these issues, a number of control experiments was performed. We show that these effects play only a minor role in the process.

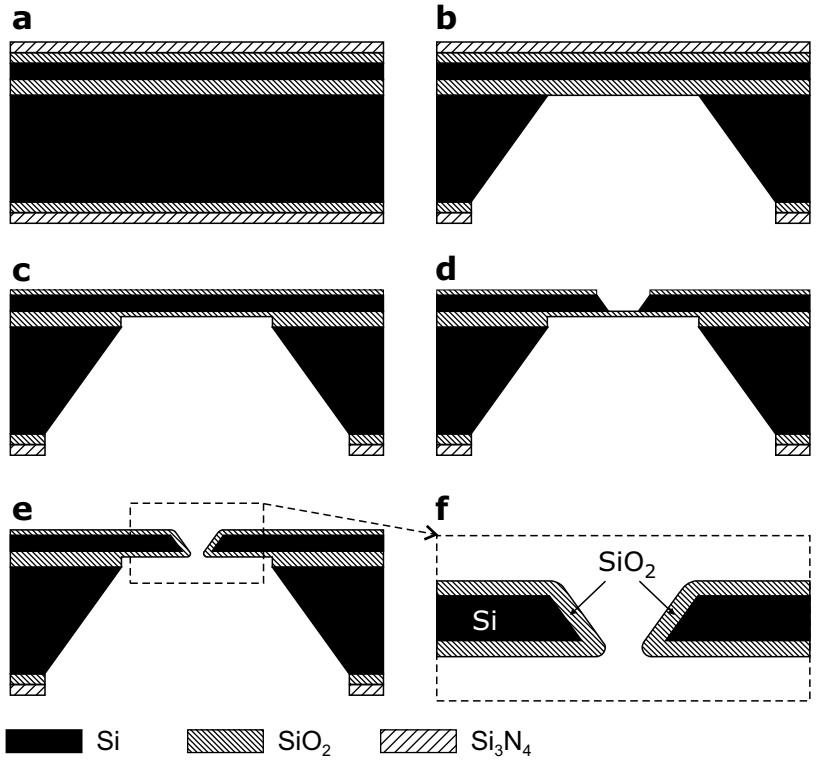

Figure 3.1: Fabrication of silicon oxide nanopores from a silicon-on-insulator (SOI) wafer, see text for details.

3.2 Materials and methods

3.2.1 Fabrication of silicon oxide nanostructures

The starting material for our pore devices is a Silicon-On-Insulator wafer (SOITEC, France) with a diameter of 100 mm. The wafer consists of a 525 μm thick 'handle' wafer, with a buried oxide-layer of 400 nm and a silicon 'device' top layer 340 nm thick. We will further denote the side of the wafer containing the device layer as the front side. Both the handle wafer and the thin device layer are $\langle 100 \rangle$ silicon single crystals and are p-doped with a conductivity of 20-30 Ωcm. The wafer is covered on both sides with a 100 nm thick TEOS silicon oxide layer. Subsequently a 100 nm LPCVD Si_3N_4 layer is deposited on both sides, see Fig. 3.1a. Then we perform electron-beam litho-

graphy and subsequent CHF_3/O_2 plasma etching on the backside of the wafer, see Fig. 3.2a for the exposed pattern. After stripping the residual resist the TEOS oxide is removed in the pattern by a wet buffered-hydrofluoric acid (BHF) etch. Using the remaining silicon nitride as a mask we perform a wet KOH etch (300 gr/l, 80°C) to obtain pyramid-shaped holes through the handle wafer. This results in thin membranes composed of the silicon device layer and the additional protection layers, see Fig. 3.1b. The buried oxide layer can be used as an etch-stop, due to the slow etch rate of silicon oxide in the KOH solution. Next to the membranes, V-shaped grooves are etched at this stage to break the wafer in smaller pieces at a later stage. A quick dip in hydrochloric acid is performed directly after removal from the KOH to prevent residues. The top silicon nitride layer is removed with a SF_6/O_2 plasma etch. At this stage the sample contains membranes formed by the silicon device layer, covered at the top with the TEOS silicon oxide layer and at the bottom by the buried oxide layer. To obtain bare, freestanding silicon membranes we remove both oxide layers using BHF. The silicon membranes are then thermally oxidized at 1000 °C to obtain a high-quality 50 nm thick silicon oxide layer on both sides. In Fig. 3.1c we show a cross-section of the device at this stage. These silicon oxide layers act as a masking layer in the second stage of anisotropic KOH etching, where the actual nanopores are formed. Initially, we attempted to use the original TEOS and buried oxide layers for this purpose, but we found significant bending of the membranes. We attributed this to stress differences between the top and bottom oxide layers. This effect caused serious problems with resist spinning on top of the membranes. With the thermal oxide, these issues were absent.

At this stage the full 100 mm wafer is diced up into smaller samples of 17 × 17 mm^2 using the V-grooves. This dicing can easily be performed by hand by placing the wafer on the edge of a Perspex plate and gently applying some pressure. Each wafer yields 16 dice of 17 × 17 mm^2, and each die contains a total of 16 membranes. In this way, we obtain a total of 256 silicon membranes for each 100 mm wafer.

The second part of the fabrication recipe consists of a second lithography and anisotropic KOH etching step, but at a scale roughly 1000 times smaller. This final fabrication step was performed on

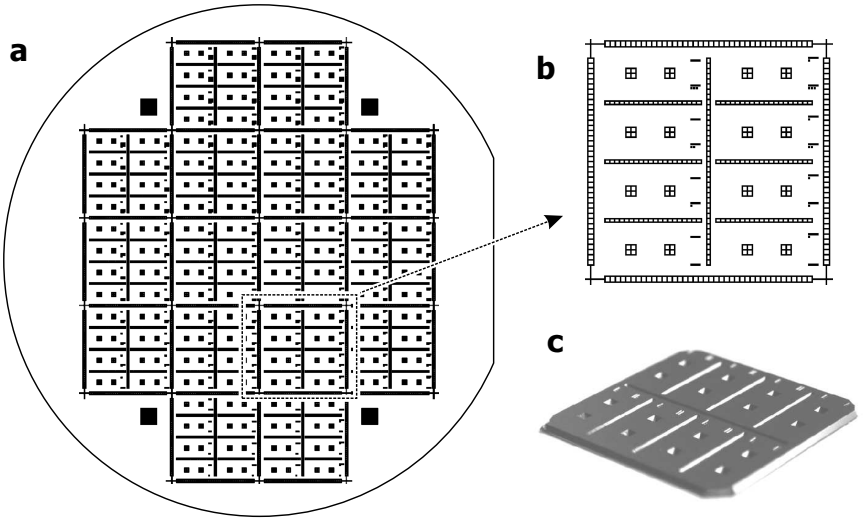

Figure 3.2: (a) Pattern for the fabrication of membranes on the 100 mm SOI wafer. Using electron-beam lithography this pattern is written at the backside of the wafer. After pattern transfer to the silicon nitride layer and silicon oxide layers, a KOH etching is performed. The 770 × 770 μm^2 squares result in 70 × 70 μm^2 membranes on the front side. Additionally a set of breaking lines is fabricated that will be used to break the wafer first into smaller chips of 17 × 17 mm^2, and finally in 5 × 9 mm^2 samples, each containing two membranes. The four large squares aid in visually detecting the end point of the KOH etch through the wafer. Note that the patterns contain large unexposed areas in the interior, to save time in the electron-beam lithography exposure. Theses unexposed regions will be underetched quickly in the hot KOH bath, and the final result is undistinguishable to fully exposed patterns. (b) Close-up of the pattern of a 17×17 mm^2 section of the wafer. The outer lines result in 480 μm wide V-grooves in the wafer. Additionally seven thinner lines are written for later dicing into devices that fit in the transmission electron microscope. Each of these samples contains a set of markers for identification. (c) Photograph of an actual 17 × 17 mm^2 chip, viewed from the backside.

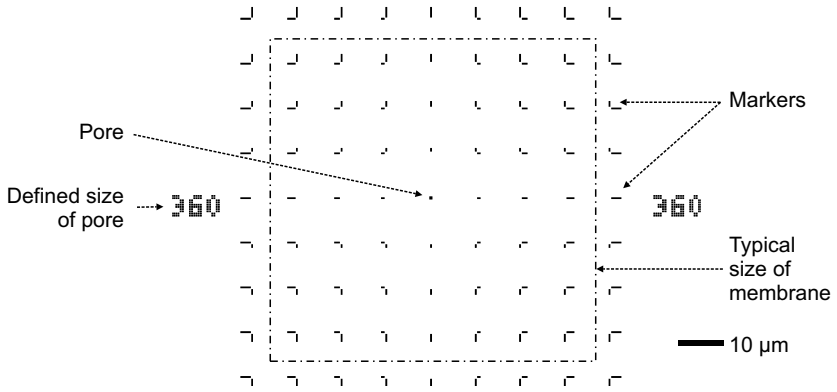

Figure 3.3: Typical pattern written on a membrane for fabrication of a single nanopore. In the center is a square of in this case 360 × 360 nm^2, that will be transferred to the silicon oxide layer. During KOH etching a pyramid-shaped pore will be etched at this position. Around the center square an array of markers is patterned. After KOH etching these markers lead to shallow V-grooves in the silicon layer. These markers help to locate the pore in the electron microscope. Additionally the defined size of the center square is written. Each digit consists of 100 × 100 nm^2 dots and will only etch about 100 nm into the silicon layer of about 300 nm thick.

17 × 17 mm^2 samples. After spinning resist, we pattern the membranes from the front side using electron-beam lithography. On most membranes we used patterns similar to the one shown in Fig. 3.3. Such patterns were used for the fabrication of a single pore in the membrane, as used in the experiments described in chapters 4 and 7. Patterns containing more than a hundred pores with various shapes and sizes were used for experiments described in this chapter. Four membranes on each chip were used as markers to align the exposed patterns with the membranes. After developing, the pattern is transferred to the silicon oxide mask layer by CHF_3/O_2 reactive-ion etching. Now we strip the remaining resist in an oxygen plasma. We then etch the sample two minutes in KOH (330 gr/l, 60°C) to obtain pyramid-shaped holes through the silicon device layer, as shown in Fig. 3.1e. Directly afterwards we rinse in diluted hydrochloric acid and remove the oxide on both sides of the membrane by BHF. Finally,

we again thermally oxidize the device to obtain a layer of silicon oxide on all silicon surfaces. As the final result, the surface of the pore and the membrane will be covered with silicon oxide layer, as shown in Fig. 3.1e and 3.1f. We studied samples with various thicknesses of the final oxide layer.

3.2.2 Electron microscopy

For inspection of the devices at various steps in the fabrication process, we used Scanning Electron Microscopy (SEM). The SEM images shown in this chapter are obtained with a Hitachi S-900 microscope, operated at an acceleration-voltage of 30 kV. This microscope allows tilting of about 50 degrees along one axis.

The deformation of our silicon oxide nanostructures during electron irradiation was studied using Transmission Electron Microscopy (TEM). The majority of experiments is performed using a Philips CM-30UT microscope operated at an accelerating voltage of 300 kV. The nanopore specimen is mounted on a specially developed holder. The electron microscope allows beam parameters such as diameter and current to be varied. Typically we worked with a beam diameter between 200 nm and 500 nm.

The Philips CM-30UT microscope is equipped with an energy-dispersive X-ray (EDX) detector. This technique allows measurements on the chemical composition of the specimen, by measuring the spectrum of the X-rays generated by the electron scattering.

Additionally, electron energy loss spectroscopy (EELS) was performed using a FEI TECNAI200 electron microscope, operated at 200 kV. The obtained spectra can be used to determine the composition of the material. These EELS experiments were performed with the entrance of the spectrometer in the focal plane of the microscope. As a result, all detected electrons are coming from a well-defined part of the specimen.

3.3 Results

We discuss a number of experiments performed to test our hypothesis that the surface tension of the fluidized silicon oxide drives the morphological changes induced by the TEM electron beam. For these

experiments we fabricated silicon membranes with more than 100 pores, in arrays with a pitch of 2 μm. Slits were fabricated within the same membrane as well. These slits are 1 μm long, and the width varies from 20 nm to about 100 nm. With this approach we have a large number of apertures in the membrane, with various sizes and shapes. The effect of the electron beam can be studied on each structure individually, since we use an electron beam of 1 μm diameter or smaller.

3.3.1 Geometry of fabricated structures before modification

Our hypothesis that surface tension drives the observed changes of our nanostructures makes the exact shape of the silicon oxide surface an important experimental parameter. In this section we address this issue based on knowledge of the fabrication process and scanning electron microscopy of our devices.

We first consider the shape of a pore before the last oxidation step. At this stage the pore has a truncated pyramid shape. This geometry is a direct result of the highly anisotropic nature of the wet KOH etch in single-crystal silicon. The surface of the silicon device layer is a (100) crystal plane. The etch rate depends strongly on the crystal direction, and the etch rate in the $\langle 100 \rangle$ direction is at least 100 times faster than in the $\langle 111 \rangle$ direction [20]. This means that the silicon etch will practically stop at the (111) crystal planes. These planes are oriented at an angle of 54.7 degrees with respect to the surface of the membrane. In Fig. 3.4a we show a scanning electron microscope image of a nanopore at this stage. The four sides of the pore are (111) crystal planes. At this stage the silicon edge at the bottom of the pore is almost atomically sharp, see the assumed cross section in Fig. 3.5a. The following step consists of growing a thermal oxide on the silicon surface. Fig. 3.4b shows another nanopore after growth of 50 nm of silicon oxide. This pore has an aperture of about 70×70 nm^2, but now it is surrounded by silicon oxide. This silicon oxide is visible as dark grey around the black pore in the SEM micrograph. The silicon underneath the oxide can be seen as light grey about 40 nm and further away from the pore. Note that the pore is still square after the oxidation process. We note that we never observed any changes in size or shape of the silicon oxide pores in the SEM microscope.

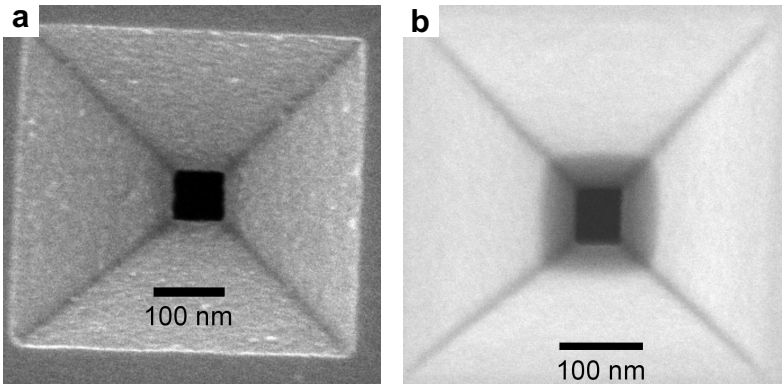

Figure 3.4: Scanning electron micrographs of pores in the silicon membrane before and after the final oxidation step. (a) The black square in the middle is an open pore of about 80 nm in the silicon membrane. The anisotropic KOH etching of the single crystal silicon leads to the inverted pyramid shape of the pore. (b) A different pore after growing a thermal silicon oxide layer of about 50 nm. In this case the pore is about 70 nm wide, and is surrounded by about 40 nm of silicon oxide. Further from the pore the silicon core of the membrane can be seen in light grey. Note that the pore is still square; the oxide layer does not lead to visible rounding of the perimeter of the pore.

We expect that the initially sharp edge at the bottom of the pore rounds significantly during the oxidation process. Oxygen gas diffuses through the oxide layer during oxidation and it reacts with the silicon underneath, 'pushing' the silicon oxide away. In Fig. 3.5b and 3.5c we sketch the assumed cross-section of the pore for a thin and a thick oxide layer. In Fig. 3.5e and 3.5f we show SEM micrographs obtained at a tilt angle of about 30 degrees of a bare silicon pore and a pore with a thermal oxide layer of about 80 nm. Clear rounding in the vertical direction is observed for the oxidized pore. We estimate that the radius of curvature is about equal to the thickness of the silicon oxide.

3.3.2 TEM-induced shape changes of rectangular pores

In all our experiments, we observe the interesting effect that rectangular pores quickly become round, typically within a few minutes. Fig. 3.6 shows a sequence of TEM micrographs of a 40 × 45 nm pore that shows clear rounding during imaging. Clearly the first changes in the pore occur at the corners, not at the straight segments. This effect will be discussed below in section 3.4.

3.3.3 Direct observation of the 'critical size'

We now present a set of experiments to demonstrate the influence of the initial geometry on the nature of deformations of pores. As discussed in chapter 2, we find that pores smaller than a certain 'critical size' shrink while larger ones expand. In this section we show this effect explicitly. Two parameters were varied in the experiments: The initial lateral size of the pore, and the thickness of the oxide grown in the last fabrication step. As discussed in section 3.3.1 the final oxide thickness is important for the shape of the pore.

First we show a series of experiments performed on four pores with a final oxide thickness of 50 nm. All pores were located within the same membrane, and imaged with a similar electron beam. We first obtained a high-resolution image with the slow-scan CCD to determine the initial dimensions of each pore. Subsequently we switched to video-rate imaging with a fast-scan CCD sensor to obtain movies of the deforming pores. In Fig. 3.7 we show three snapshots from each movie, for pores with an initial size of 40 nm, 55 nm, 80 nm

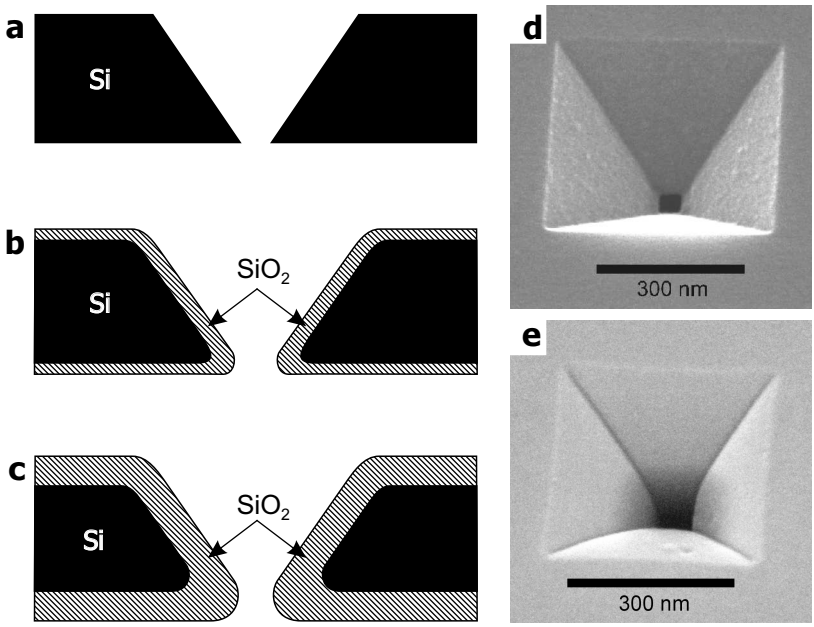

Figure 3.5: Rounding of the pore during thermal silicon oxide growth. (a) Schematic, cross-section view of a silicon membrane with a pore. Note the sharp angle at the bottom. (b) Similar pore after growing a thin oxide layer. We expect the initially sharp corner to round off. (c) Expected pore cross-section after growth of a thick silicon oxide layer. (d) SEM micrograph of a pore before oxidation, at a tilt angle of about 30 degrees to reveal the three-dimensional shape. (e) Pore with a thick silicon oxide layer of about 80 nm. Note the clear rounding of the silicon oxide around the nanopore in the vertical direction.

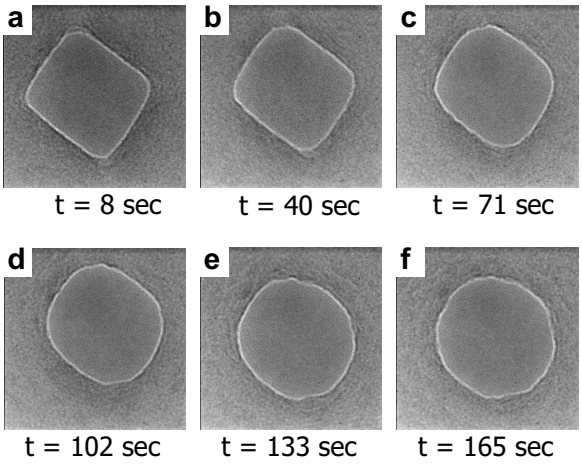

Figure 3.6: (a-f) Rounding of the perimeter of a 40 × 45 nm^2 pore during the first minutes of TEM imaging.

and 100 nm respectively. We denote the initial size as the average of the two sides of the rectangular shape. From the micrographs we see that pores of 40 nm and 55 nm close down and that the 100 nm pore expands. Very little changes other than rounding are observed for the 80 nm pore. This experiment clearly demonstrates the existence of a 'critical size': Smaller pores shrink and larger pores expand. We estimate that the 'critical size' is about 80 nm ± 20 nm for this device. Because a square pore with sides x rounds off quickly to a circular pore with a diameter of about x, the critical size is equivalent to the critical diameter as discussed in chapter 2.

A second sample was prepared with an array of pores of various sizes, but now with a final oxide thickness of only 20 nm. Here we expect a much sharper apex of the pore, and we show how this affects the pore dynamics. The experiment was performed under similar conditions as the previous one. Fig. 3.8 shows the result for four pores with initial sizes of 15 nm, 30 nm, 35 nm and 40 nm. We find that the 15 nm pore shrinks, and the 35 nm and 40 nm ones expand. The size of the 30 nm pore stays quite constant during the experiment. For this device we find a critical size of 25 nm ± 10 nm, which is significantly smaller than for the thick-oxide sample.

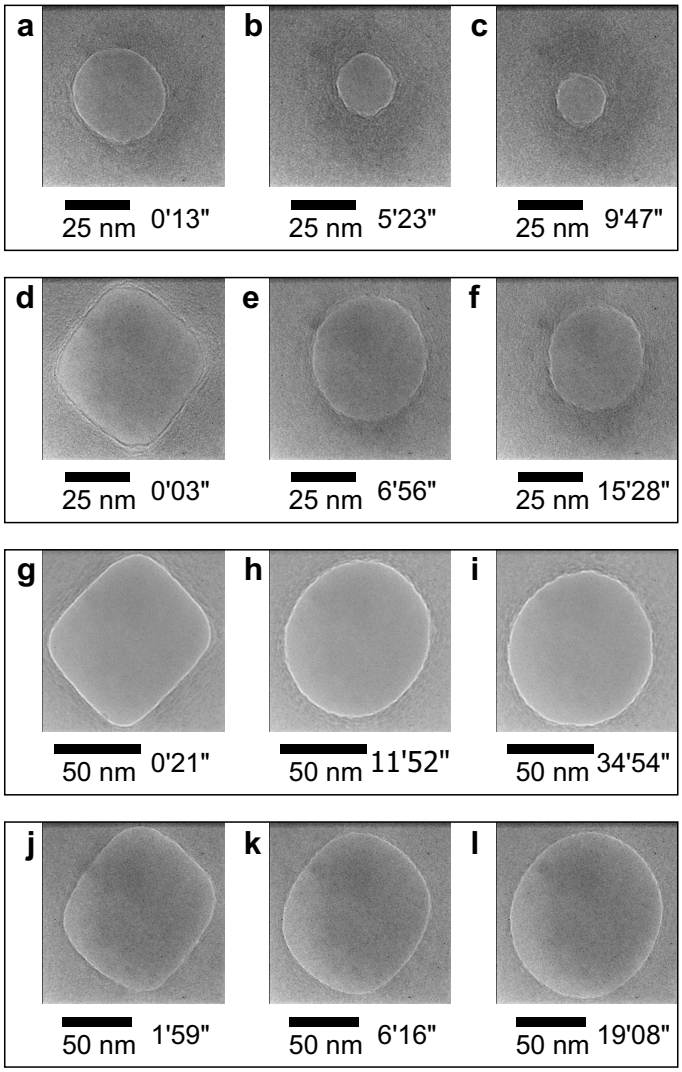

Figure 3.7: (a-c) TEM micrographs of a nanopore with an initial size of about 40 nm. (d-f) TEM micrographs of a nanopore with an initial size of about 55 nm. (g-I) TEM micrographs of a nanopore with an initial size of about 80 nm. (j-l) TEM micrographs of a nanopore with an initial size of about 100 nm.

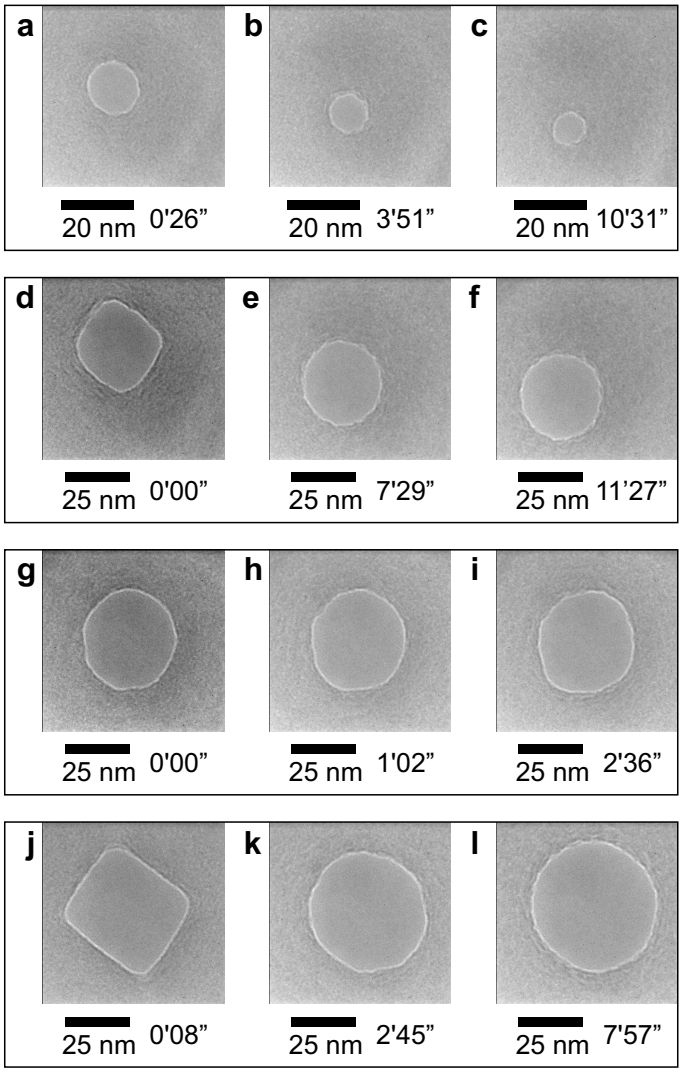

Figure 3.8: (a-c) TEM micrographs of a nanopore with an initial size of about 15 nm. (d-f) TEM micrographs of a nanopore with an initial size of about 30 nm. (g-I) TEM micrographs of a nanopore with an initial size of about 35 nm. (j-l) TEM micrographs of a nanopore with an initial size of about 40 nm.

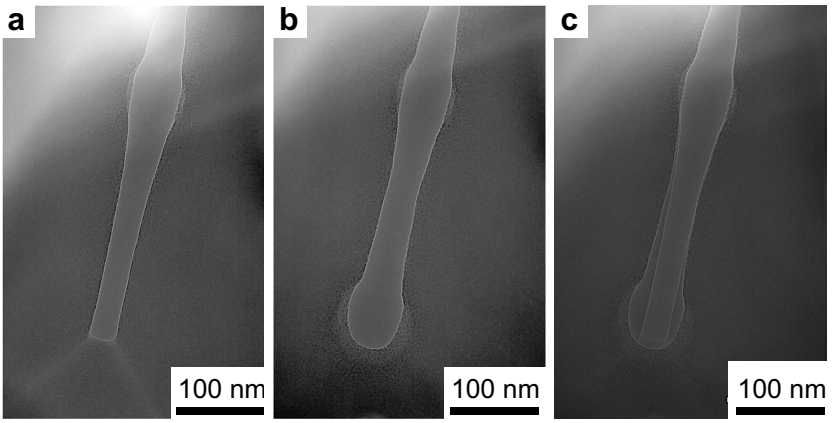

Figure 3.9: (a) TEM micrograph of a slit in silicon oxide after TEM irradiation with an electron beam of about 150 nm. (b) The same slit after irradiation at the end of the slit with an electron beam of about 150 nm. (c) Images a and b superimposed. Here we used the feature from the top of Fig. 3.9a for alignment.

3.3.4 Deforming a narrow slit

The effect of the electron beam on straight edges is demonstrated by imaging a 40 nm wide slit with a spotsize of about 150 nm. The slit was initially rectangular shaped. Figure 3.9a shows the resulting structure at a much lower magnification with a much larger beam. At the location of the electron beam (near the top of the image), the slit has expanded considerably. On the same structure, we then imaged the end of the same slit with a spotsize of again 150 nm. As shown in Fig. 3.9b the slit has become wider and longer at the end. In Fig. 3.9c the two micrographs are superimposed, to demonstrate this even clearer.

This experiment shows that the changes induced in a 40-nm-wide slit are very different to changes observed in a 40×40 nm^2 pore: Only pores show shrinking behavior, slits do not. This difference will be addressed in section 3.4. This experiment also demonstrates that the deformations are very local. The top part of the slit, only 300 nm away from the end, remains unchanged during the deformation of its end.

3.3.5 Elemental analysis on deforming pores

In this section we discuss the possible changes to the material, caused by the high-intensity electron beam. This is an important issue because well-known effects observed in electron microscopy such as the deposition of carbon-rich contamination could provide an alternative mechanism for pore closure. Another issue is electron-beam induced depletion of material. Such an effect could explain the observation of expanding pores. To shed light on these issues we performed control experiments where we measure the composition of the material of our devices inside an electron microscope.

First we discuss a set of energy-dispersive X-ray (EDX) experiments. The material irradiated by the electron beam emits X-rays, and from the spectrum we obtain information on the elements present in the material. The 'detection volume' is limited by the probe size (the beam can be as small as a few nanometers) and the thickness of the specimen. Ideally, we would have liked to solely determine the composition of the material that fills the nanopore by using a small probe on the material that has closed down a nanopore. This however is not possible because for proper spectra we need a direct line-of-sight from the specimen to the detector, see Fig. 3.10. With the current sample layout and orientation, we cannot obtain this configuration.

We obtained EDX spectra during a pore closing experiment. Figure 3.10 shows the orientation of our specimen relative to the beam and the detector in this experiment. The sample was tilted 15 degrees towards the EDX detector. In this experiment, we shrunk a 50 nm pore to about 25 nm in 45 minutes. We used an electron beam of about 1 μm diameter and a dose of about $7{\cdot}10^4$ A/m^2. Fig. 3.11a shows an electron micrograph of the pore at the beginning of the experiment, and Fig. 3.11b at the end. Note that the TEM micrographs show non-circular pores. This is due to the tilt angle of the specimen. Fig. 3.11c shows the EDX spectra obtained, where spectrum 1 is obtained at the start and spectrum 2 after the experiment. Clearly visible are the oxygen peak around 0.5 keV and the silicon peak around 1.8 keV. We find that the silicon peak stays constant, but the height of the oxygen peak is reduced by about 8%. From this experiment we estimate that the rate of oxygen loss is about 10% per hour. The effect of oxygen loss from silicon oxide during electron

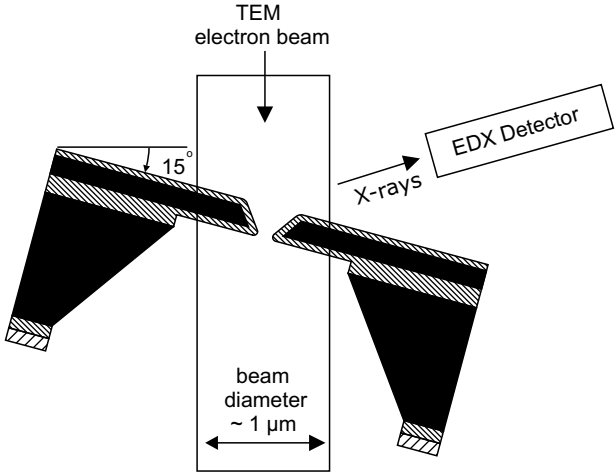

Figure 3.10: Orientation of nanopore device in electron microscope for EDX analysis experiments.

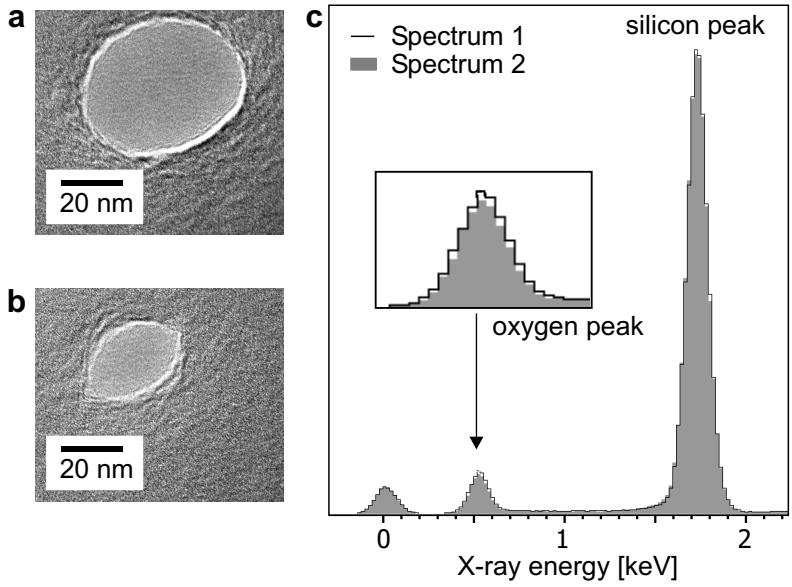

Figure 3.11: (a) Electron micrograph of the the pore at the start of the EDX experiment. (b) The same pore at the end of the EDX experiment, 45 minutes later. (c) The EDX spectra obtained at the beginning(spectrum 1, black line) and at the end (spectrum 2, grey histogram) of the experiment.

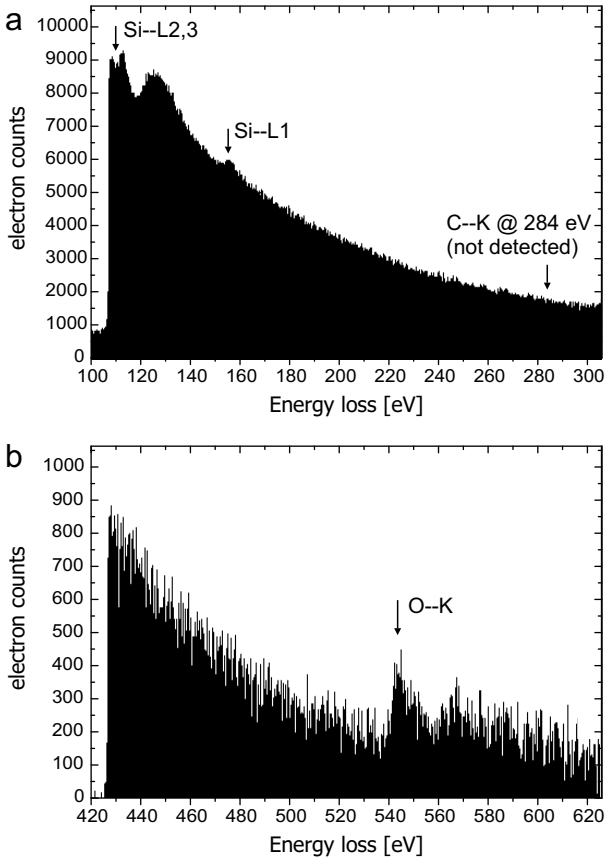

Figure 3.12: (a) and (b) Electron-energy-loss spectra obtained on the material that has filled a nanopore.

irradiation has been studied in more detail by Chen *et al.* [16].

In our TECNAI microscope we performed an electron energy loss spectroscopy (EELS) experiment. We first closed down a nanopore in this microscope. Subsequently we performed an EELS experiment in imaging mode to ensure that only electrons are collected from the material that has filled the pore. The effective probe volume has a diameter of only 4 nm, determined by the magnification and the size of the input of the electron spectrometer. Figure 3.12 shows the result of this experiment. Fig. 3.12a shows very clear peaks caused by silicon between 108 eV and 160 eV. The peaks at 108 eV and

112 eV are the Si-L2,3 peaks, and the peak at 156 eV is the Si-L1 peak. Note that the positions of these peaks are different than those observed for pure silicon (L-2,3 at 101 eV, L-1 at 150 eV). We find no detectable carbon peak around 284 eV (C-K). We estimate that at most two atomic percent of the material consists of carbon. Figure 3.12b shows a peak around 545 eV (O-K), a clear sign of the presence of oxygen. These experiments prove that the material that closes our nanopores is primarily silicon oxide.

3.4 Discussion

The aim of this chapter is to obtain a more detailed understanding of the mechanism driving the deformations of nanostructures. We have studied pores in silicon oxide with various diameters, and we find that small pores shrink, and large ones expand. We define the 'critical size' as the size separating these two effects and have found that it varies with the thickness of the final oxide layer on our devices. In chapter 2, we concluded that surface tension drives deformations in our nanostructures. Here we discuss a more detailed version of the same model, to explain the experiments presented in this chapter.

We start be briefly reiterating the model discussed in chapter 2. The surface tension of a material is defined as the amount of free energy per unit area of surface. An object in a viscous-fluid state will deform to lower the total surface area. We believe that the surface tension of the silicon oxide is the main driving force of the observed changes in our nanostructures. We model our structure as a cylindrical hole with radius r in a film with uniform thickness h. We then calculate the difference in free energy of the perforated film with respect to the intact film. The free energy change ΔF is proportional to the change in surface area ΔA: $\Delta F = \gamma \Delta A = 2\pi\gamma(rh - r^2)$, see figure 2.4. The result is that, according to this model, pores with $2r < h$ can lower their free energy by shrinking and larger pores can do so by expanding. This effect qualitatively explains our experimental observations on deforming nanopores. The critical radius for this model is $r = h/2$.

While this model allows us to understand the simple physics behind the observed critical size, it has a number of limitations. A first point is that the deformation of the pore is taken into account only

as a single parameter r. A perfect cylindrical shape during shrinking is thus assumed. A second issue is that the total volume of the film is not constant in this model.

A number of these limitations can be overcome by looking at local forces generated by the surface tension. Laplace calculated that a curved surface under tension leads to a pressure difference over the interface. For a sphere this pressure difference is $\Delta P = 2\gamma/R$, where γ is the surface tension and R the radius of the sphere. On an arbitrary curved surface the pressure can be calculated with the Laplace-Young equation: $\Delta P = \gamma(1/R_1 + 1/R_2)$. Here R_1 and R_2 are the two local radii of curvature taken at perpendicular directions along the surface. Note that the sign of the radii should be taken into account; the net pressure at a 'saddle' point with two opposite but equal curvatures will be zero. Fig. 3.13 depicts a second model for our nanopores. We consider the circle of points at the surface closest to the axis. In Fig. 3.13 we show R_1 and R_2, the two local radii of curvature. It follows immediately that for $R_1 < R_2$ there will be a Laplace pressure directed towards the axis of the pore. Since R_2 is $h/2$ we see that this amounts to the same prediction as the free energy model. Planar surfaces located near the pore have zero interface pressure difference. The pressure difference between points at the strongly curved surface inside the pore and points further away will lead to mass transport towards or away from the pore.

Within this model the critical radius $R_{critical}$ thus equals the radius of curvature of the aperture in the vertical direction R_2. In the experiments described in section 3.3.3 we have indeed observed different critical radii for various values of R_2. The curvature was approximated using the thickness of the oxide, as discussed in section 3.3.1. We found critical diameters of 25 nm $\pm$10 nm and 80 nm $\pm$ 20 nm for an oxide thicknesses of 20 nm and 50 nm respectively. These values are in good agreement with the model, considering the approximations made.

The rounding of square apertures as shown in Fig. 3.6 can now also be understood: The curvatures are strongest in the corners of the square, and this will lead to the highest Laplace-pressures towards the axis of the pore. These high forces lead to quick changes at the corners, as observed in the experiment.

We now explain the widening of a slit in silicon oxide during

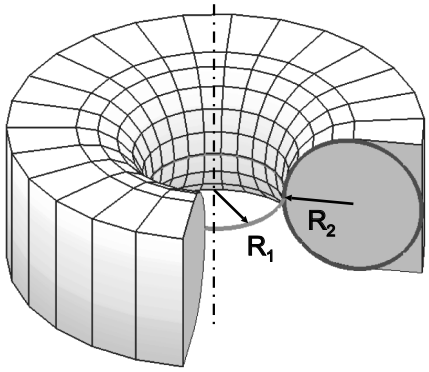

Figure 3.13: Approximation of our nanopore geometry. The two radii of curvature of the siliconoxide surface are shown for the points that are closest to the axis of the pore. Note that R_1 is equal to the radius of the pore.

irradiation, as shown in Fig. 3.9a. When we consider a point along the slit, away from the ends, we find that R_1 is effectively infinite, and thus there is no inward pressure. R_2 however is finite, and leads to a Laplace pressure that widens the slit. The effect at the end is more subtle: In addition to the widening effect for the long edges of the slit as discussed above, there is an inward pressure due to the corners of the slit where R_1 is small. In the experiment shown in Figs. 3.9b,c we see that the slit also expands at the end. Apparently the widening effect dominates, and shrinkage is only observed for pores smaller than the critical size.

3.5 Conclusion

In this chapter we have discussed a set of experiments that further improve our understanding of the mechanism driving the nanostructure deformations upon electron beam irradiation. We demonstrate that some pores shrink and others expand, based on their initial size. We conclude that the additional experiments and considerations further strengthen the conclusion of chapter 2: An electron beam of sufficient intensity fluidizes the silicon oxide, and as a consequence the material will deform, driven by the surface tension of the melt.

Acknowledgements

The work presented in this chapter was done in collaboration with Jianghua Chen, Sean Ling and Henny Zandbergen. We thank Emile van der Drift, Bert Goudena, Arnold van Run and Marc Zuiddam for assistance in clean-room processing and useful discussions.

Chapter 4

Translocation of double-strand DNA through a silicon oxide nanopore

Abstract

We report double-strand DNA translocation experiments using silicon oxide nanopores with a diameter of about 10 nm. By monitoring the conductance of a voltage-biased pore, we detect molecules with a length ranging from 2000 to 48000 base pairs. We find that the molecules can pass the pore both in a straight linear fashion and in a folded state. Experiments on circular DNA further support this picture. We sort the molecular events according to their folding state and estimate the folding position. As a proof-of-principle experiment, we show that a nanopore can be used to distinguish the lengths of DNA fragments present in a mixture. These experiments pave the way for quantitative analytical techniques with solid-state nanopores.

4.1 Introduction

Translocation of biopolymers such as polypeptides, DNA, and RNA is an important process in biology. Transcribed RNA molecules for example are transported out of the nucleus through a nuclear pore complex. Viral injection of DNA into a host cell is another example. Experimental and theoretical studies of this process have attracted considerable attention. Kasianowicz *et al.* [5] demonstrated that an α-hemolysin pore in a lipid membrane can be used to study the translocation process in vitro. By measuring the ionic current through a voltage-biased nanopore, they detect individual molecules that are pulled through the pore by the electric field. More recently, Li *et al.* [13, 21] showed that solid-state nanopores can also be used for similar experiments. Here we describe a set of translocation experiments with silicon oxide nanopores that were fabricated with the technique described in chapters 2 and 3. We present a detailed study of the translocation dynamics of double-strand DNA molecules with lengths ranging from 2000 to 48000 base pairs.

The dynamics of DNA translocation through nanopores is particularly relevant for potential analytical techniques based on nanopores. Rapid oligonucleotide discrimination on the single-molecule level has been demonstrated with α-hemolysin [22], and more recently solid-state nanopores were used for a first study of folding effects in double-strand DNA molecules [21]. Future applications of this technique may include DNA size determination, haplotyping, and sequencing.

The use of nanopores for the detection and analysis of single molecules is inspired by the working principle of a Coulter counter [23]: Particles suspended in an electrolyte solution are drawn through a small channel, separating two reservoirs. When a particle enters the channel, it displaces its own volume of solution, thereby increasing the electrical impedance of the channel. By applying a voltage over the channel, the passing particles are detected as current drops, and the magnitude of the current dip scales with the volume of the particle. This analytical technique has proven very effective in determining the concentration and size distribution of particles, down to the submicrometer size. The availability of nanometer-sized apertures has extended this technique to the single-molecule level. Such nanopores have been shown to detect polynucleotides, using pores with a diameter slightly larger than the cross-section of the molecule. The signal

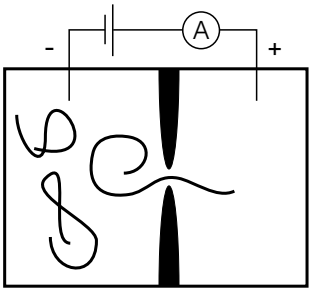

Figure 4.1: Schematic layout of the experiment: A charged polymer is electrophoretically driven through a nanometer-sized aperture, located between two reservoirs kept at a potential difference. The presence of a molecule inside the pore lowers the amount of conducting solution inside the pore. Passing molecules can thus be detected as short dips in the ionic current trough the pore.

now scales with the cross-section of the molecule, since only a small fraction of the length of the molecule occupies the sensing volume of the pore at any time during translocation. Figure 4.1 shows a typical experimental layout for such experiments. One of the main challenges is to obtain pores with a diameter comparable to the diameter of the polymer, about 2 nm for double-strand DNA.

The use of α-hemolysin has the advantage that it self-assembles and all pores are identical down to the atomic level. Such pores have been used most extensively, but there is also a large interest in synthetic pores. The fabrication of such pores requires an accuracy on the single-nanometer level, which is far from straightforward with existing techniques. Such an effort is justified however because of a number of potential advantages of solid-state pores over protein pores. Firstly, the dimensions of the pore can be varied to ensure optimal sensitivity. Secondly, solid-state nanopores are much more robust: They are expected to have a much longer lifetime, and experiments can be performed at high temperatures and at extreme pH values. Finally, solid-state pores allow additional device complexity, and incorporation of additional tools. For example, Li *et al.* [21] speculated that electrodes integrated within the nanopore could be used to detect tunnelling currents through molecules as they pass the nanopore, analogous to the working principle of a scanning tunneling

microscope. They aim to read off the base sequence of a single DNA molecule as it passes the detector inside the nanopore.

In this study, we report single-molecule detection of double-strand DNA using silicon oxide nanopores that were fabricated using a technique recently developed in Delft (see chapter 2). Linear double-strand DNA fragments of 11.5 kilobase-pairs (kbp) and 48 kbp and a circular DNA vector of 11.5 kbp were studied with our nanopore setup. We find strong evidence for translocation of folded DNA, where passage starts not at one of the ends of the molecule but somewhere in between [21]. A part of the molecule folds back onto itself, resulting in current blockades that are are larger in amplitude and shorter in time than simple linear translocation events. We present additional evidence for this picture with the detection of translocation of circular DNA molecules. These circular molecules can only pass the pore in a folded state. Indeed we observe qualitatively different statistics of the translocation events compared to linear molecules that are in good agreement with the model. The experiments demonstrate that double-strand DNA with a persistence length of about 50 nm can indeed pass an 8 nm pore in a folded fashion. The pore was slightly smaller than the 10 nm pores that were used for the experiments on linear DNA.

Finally, we present an experiment that demonstrates the remarkable sensitivity of a nanopore detector. We have used a nanopore to analyze the size distribution of a standard mixture of double-strand DNA fragments, ranging in length between 2 kbp and 24 kbp. In this proof-of-principle experiment, we analyzed translocation events of about 2500 individual molecules (about 30 fg = $3{\cdot}10^{-14}$ g or 4 zeptomol = $4{\cdot}10^{-21}$ mol), and demonstrate clear separation in length.

4.2 Materials and methods

4.2.1 Fabrication of solid-state nanopores

We use solid-state nanopores fabricated using a process reported in chapter 2. Starting from silicon-on-insulator (SOI) wafers (obtained from SOITEC, France), we first fabricate a free-standing silicon membrane using electron beam-lithography, reactive-ion etching and wet chemical KOH etching. Subsequently we fabricate pores of about 50 nm in this 340 nm thick silicon membrane by a second step of

electron-beam lithography and wet chemical KOH etching. This membrane is thermally oxidized to form a 40 nm thick, silicon dioxide layer on the surface of the membrane and pore. Surprisingly, we found that we can shrink the pore by exposure to a high dose of electrons, supplied by the imaging beam of a transmission electron microscope (TEM). The process can be observed in real time on the fluorescent screen of the microscope. This allows us to stop when the desired dimensions of the pore have been obtained, by blanking the electron beam (see Fig. 4.2 for a schematic device layout and two electron micrographs obtained during the shrinking process). This technique allows us to very reliably fabricate solid-state nanopores with any desired diameter, at least down to 2 nm. We used pores with a diameter of 10 nm for the experiments on linear DNA, and an 8 nm pore for the experiment on circular DNA.

4.2.2 DNA material

A 11.5 kbp 'charomid' vector was cloned into ecoli dh5-α bacteria, cultured, and purified using a commercial Mini-prep kit (Qiagen). It was subsequently restriction-digested using EcoRI and purified using phenol-chloroform extraction. The length of the digested plasmid was verified using gel electrophoresis. To obtain circular DNA of 11.5 kbp with a single nick, the nicking enzyme N.BbvCIA was used in stead of the EcoRI. The same protocol was used to purify this fragment. Linear λ-DNA with a length of 48 kbp was obtained commercially (Promega, Benelux). The standard mixture of DNA fragments produced by incubating λ-DNA with the HindIII restriction enzyme was also purchased from the same source. It contained fragments with a length of 23130 bp, 9416 bp, 6557 bp, 4361 bp, 2322 bp, 2027 bp, 564 bp and 125 bp.

4.2.3 Experimental set-up and techniques for DNA translocation experiments

TEM-fabricated nanopores were mounted in a fluidic setup. The nanopore device is clamped horizontally in between two parts of a Poly(dimethylsiloxane) (PDMS) cell, see Fig. 4.3. Each of these parts contains a fluidic reservoir of about 50 μl, and the nanopore is the only connection between the two reservoirs. Both reservoirs contain a

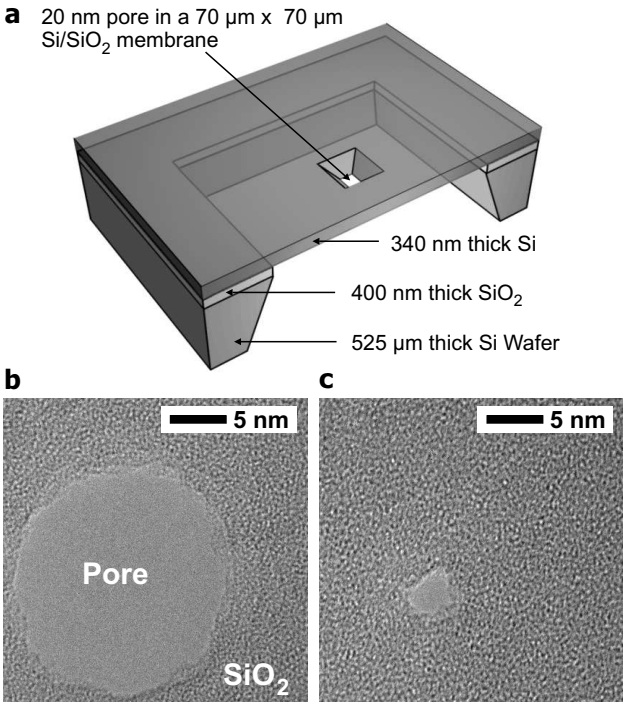

Figure 4.2: (a) Cross-sectional view of our sample layout. From silicon-on-insulator (SOI) wafers we fabricate free standing, silicon membranes with a thickness of 340 nm. A pore is etched in this membrane by wet KOH etching. Thermal oxidation of all silicon surfaces yields a pore with a diameter of about 20 nm, surrounded by 40 nm of silicon oxide. (b) Using the electron beam of a TEM microscope, we can effectively melt the silicon oxide causing the pore to shrink. Here we show an electron micrograph of a pore before the shrinking process. (c) Final image of a pore just before we blank the electron beam. The pore shown here has a diameter of about 3 nm.

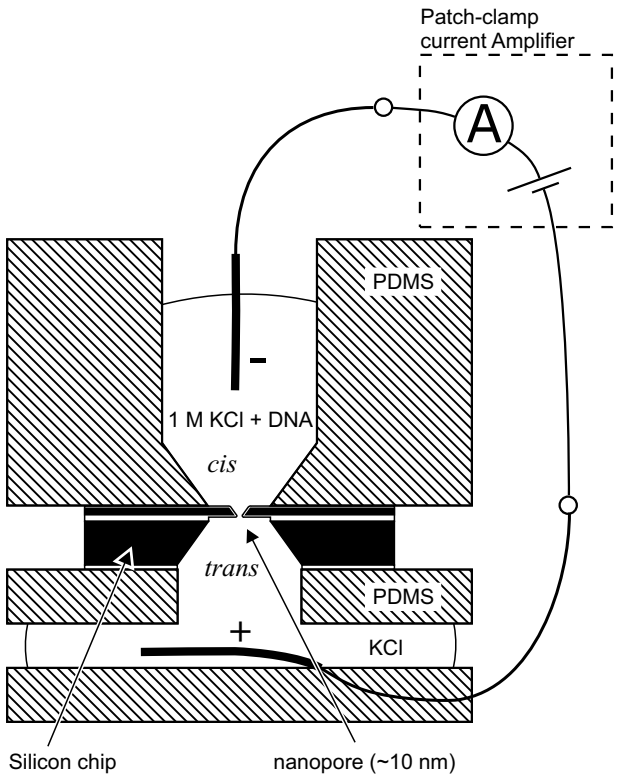

Figure 4.3: Cross-sectional view of the fluidic set-up (not to scale). Shown in light grey are two PDMS parts that contain the reservoirs. A silicon chip containing the nanopore is clamped horizontally in between. Both reservoirs contain a Ag/AgCl electrode for electrical contact. A patch-clamp current amplifier is used for the ionic-current measurements at high bandwidth.

Ag/AgCl electrode for electrical contact to the liquid. A patch-clamp amplifier (Axopatch 200B amplifier from Axon Instruments) was used to apply a voltage over the two electrodes and to detect and amplify the resulting ionic current. The signal is low-pass filtered using a four pole Bessel filter with a cut-off frequency of 10 kHz. The signal was then digitized (with an Axon 1322A digitizer) at 200 kHz and recorded to the hard disk of the computer. All experiments were performed at room temperature. We also recorded the current signal continuously on a Digital Audio Tape (DAT) with a Dagan DAS-75 recorder.

A well-known difficulty of small fluidic systems is priming it with the electrolyte solution. Incomplete priming can result in trapped air bubbles inside the nanopore, blocking the ionic current partially or even completely. We found that cleaning our samples for about 30 seconds in an oxygen plasma aids in wetting of our devices. This procedure cleans the sample from organic contamination and results in a hydrophilic SiO_2 surface. Immediately after the plasma treatment we mount our device in the setup and fill it with a degassed and filtered buffer solution (1.0 M KCl, 10 mM Tris-HCl, pH 8.0, 1 mM EDTA). Usually this procedure leads to a stable current signal, but occasionally additional oxygen-plasma cleaning was necessary before a stable, low noise signal was obtained.

In a typical experiment we add 1 μl to 5 μl of DNA solution (concentration between 100 to 500 ng/μl) to the *cis* reservoir of the setup, which contains between 20 μl and 50 μl of buffer solution. A negative voltage is applied to the *cis* side of the nanopore and we observe short dips in the ionic current, as shown in Fig. 4.4 for 11.5 kbp DNA. These events are caused by the translocation of DNA through the nanopore. Data recording was triggered when the current dropped about 80 pA below the open pore current, with a pre-trigger sampling-time of 2.5 ms.

4.2.4 Analysis of translocation events

Further analysis of individual events was performed using a dedicated Labview (a graphical programming language from National Instruments) program. For each recorded event, the open pore current was determined from the pre-trigger part of the measurement. During the experiment the open pore current slowly drifts due to small potential

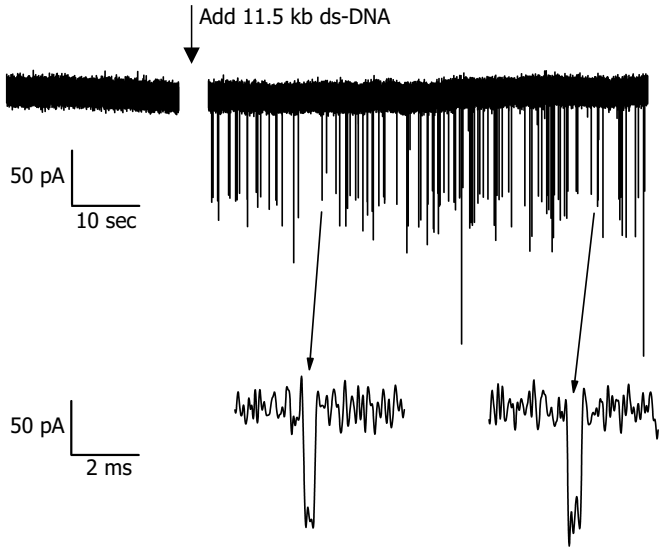

Figure 4.4: Measured ionic current versus time. After addition of DNA to the *cis*-side of the pore we clearly observe downward dips in the current. In the bottom panel, two individual events are shown at an increased time resolution.

drifts caused by the Ag/AgCl electrodes and concentration changes due to evaporation. To compensate for such drifts all further analysis was performed on currents relative to the open-pore current denoted as I_{baseline}.

Closer inspection of the current data suggests that on many occasions, single events consist in fact of one or more plateaus at discrete current levels, as the events for 48 kbp DNA depicted in Fig 4.5 clearly demonstrate. They can be classified into several types, as discussed below. Discrete current levels are further demonstrated in Fig. 4.6, where we show a histogram of 5 μs current samples relative to the baseline. Note that each count in this histogram corresponds to a single current measurement, not to a single event. A typical recorded time trace lasts about 6 ms and therefore generates roughly 1200 counts in the histogram. Fig. 4.6 compiles about 1600 time traces, or $2{\cdot}10^6$ counts. Sharp peaks at 0 pA, 150 pA, 294 pA, 434 pA, 569 pA and 699 pA are evident. The first peak at 0 pA is the open pore current, recorded before and after the event. We interpret subsequent peaks as corresponding to the presence of one or more double-strands of DNA inside the pore. Note that we observe events that have up to five ds-DNA within the pore simultaneously. Two effects can cause the presence of more than one double-strand inside the pore: Two or more molecules can translocate at the same time, or a single molecule can be folded to pass the pore more than once. Below, we argue that the latter holds.

It is interesting to note that the full width at half maximum of the peaks is nearly constant for all peaks, including the baseline peak. If the width of the peaks is caused by noise generated by the presence of a molecule in the pore, it would likely increase with increasing number of molecules. The near-constant width therefore indicates that the main cause of the noise is instrumental as opposed to the presence of a molecule in the pore.

The position of the peaks in this histogram is the basis for our event-fitting algorithm to allow sorting and automated analysis on a large number of events. At the position of the peaks in Fig. 4.6 we define discrete levels labeled from '0' to '5', and for each event we fit all current data to the nearest discrete level. If a certain level lasts shorter than 30 μs, we discard it and change it to the level directly following it. This procedure is performed because the data

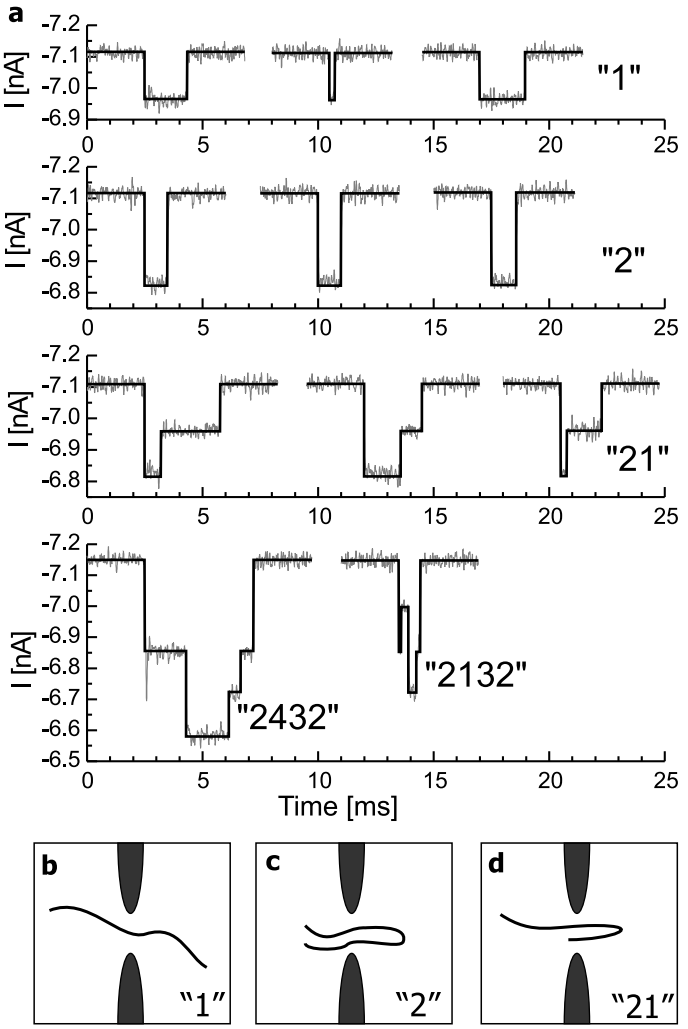

Figure 4.5: (a) Examples of recorded events for λ-DNA. The grey noisy line is the raw data, the black line is the result of a fitting algorithm discussed in section 4.2.4. The top panel shows events of type '1'. These events have a single plateau at the first level. Below are events of type '2'. These also have a single plateau, but twice as deep as '1'. The third panel shows events with two plateaus: First at the second level and then at the first. These events are labeled as '21' events. Bottom panel: Examples of more complicated event shapes. (b-d) Physical interpretations of various event types. Translocation is directed from left to right.

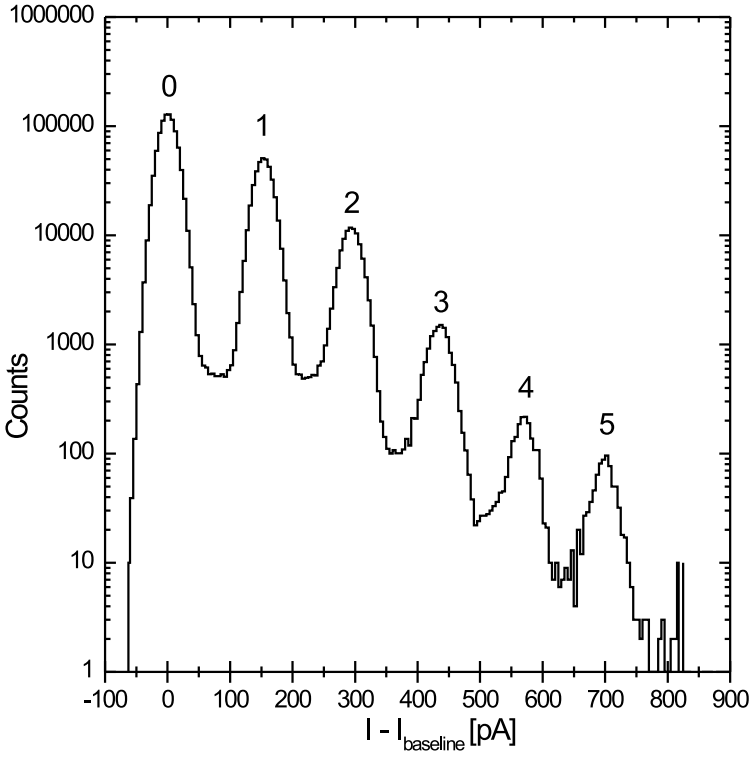

Figure 4.6: Histogram of 5 μs current samples, obtained from about 1600 recorded time traces, each about 6 ms long. For each event the baseline (open pore) current was determined from the pre-trigger part of the measurement. This value was subtracted and a histogram was calculated from all recorded 5 μs samples of the current, relative to the baseline.

was filtered at 10 kHz, and consequently levels shorter than 30 μs are likely to be caused by a slow response of the filter to a level change of more than one 'step'. Another cause for undesired short events is that occasionally the random noise reaches the threshold for a neighbouring level. The fitting procedure reduces each event to a sequence of one or more sub-events, where a sub-event is characterized by one of the 5 discrete levels of current blockade and its duration. Fig. 4.5a shows the measured signal for a number of events and the result of the described fitting procedure. We group similar events by the sequence of levels of its sub-events. Events of type '1' for example are simple blockades to the first level. Events of type '21' consist of two sub-events, first at the second level and subsequently the first level. This labeling allows us to study statistics of subsets of all measured events. Fig. 4.5b-d shows the physical interpretation of a number of event types.

For each event we determine the dwell time t_{dwell}, defined as the duration of the full event. Additionally, we integrate the raw measured current relative to the baseline, $\int (I(t) - I_{\mathrm{baseline}})\,\mathrm{d}t$. This we will call the 'area' of an event. From this integrated area we determine the average amplitude of the blockade I_{block}, defined as the area divided by t_{dwell}.

4.3 Results

4.3.1 Translocation of linear ds-DNA

First, we discuss experiments performed on linear double-strand DNA molecules, detected with a 10 nm pore. Two sets of experiments were performed, one on 11.5 kbp DNA and one using 48 kbp DNA. In both experiments, we used a bias voltage of -120 mV, applied to the *cis* side of the setup containing the DNA. The *trans* side was connected to ground. All the recorded events were analyzed using the procedure described in the preceding section. First, we look at the average amplitude and dwell times of all events. In Fig. 4.7a and 4.7e each point represents a single event. Fig. 4.7b and 4.7f show histograms of t_{dwell} and Fig. 4.7c and 4.7g show histograms of I_{block} for these two molecules. The results for the calculated event areas are plotted in Fig. 4.7d and 4.7h. As is clear from these figures, events are clustered together for both molecules. Both the dwell

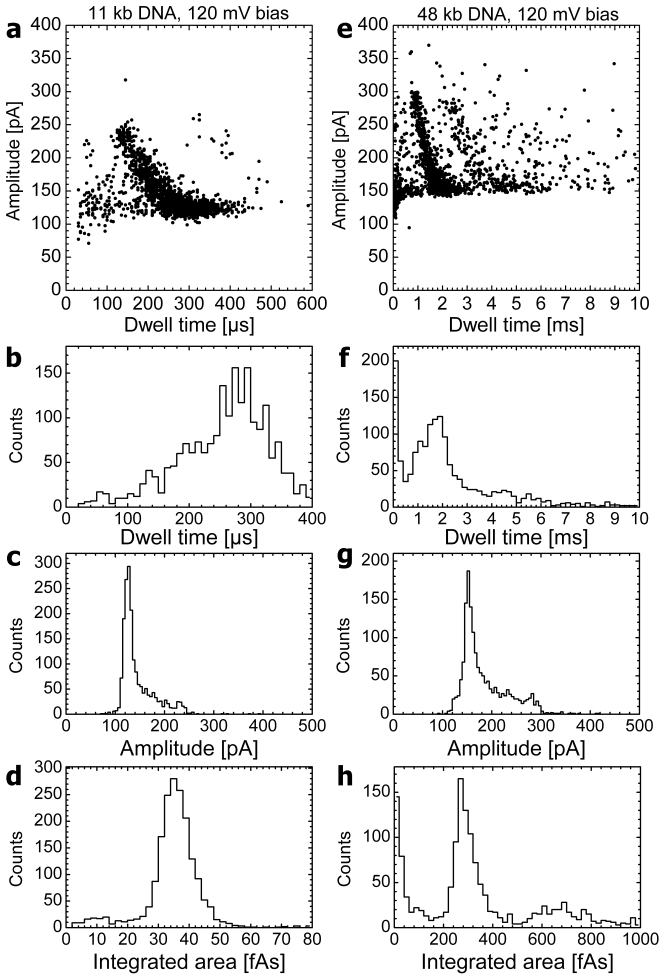

Figure 4.7: (a) Event scatter plot of 1855 events recorded at 120 mV bias with 11.5 kbp linear DNA molecules. For each event the dwell time and the average amplitude were determined. Each point in the graph corresponds to a single event. (b) Histogram of observed dwell times for 11.5 kbp DNA. (c) Histogram of observed amplitudes for 11.5 kbp DNA. (d) Histogram of observed areas for 11.5 kbp DNA. (e) Event scatter plot of 1598 events recorded at 120 mV bias with 48 kbp λ-DNA molecules. (f) Histogram of observed dwell times for 48 kbp DNA. (g) Histogram of observed amplitudes for 48 kbp DNA. (d) Histogram of observed areas for 48 kbp DNA.

time and amplitude distributions appear to be quite broad. The two are correlated though: The shorter the dwell time, the higher the amplitude I_{block}. Comparing the results for the two molecules we find a similar distribution of amplitudes for both: A peak near 140 pA and a tail up to 300 pA. The dwell-time histograms, however, are quite different: For the 48 kbp λ-DNA we find typical dwell times between 1 ms and 2 ms, about a factor of 7 longer than the 150 μs to 350 μs observed for the 11.5 kbp molecules. This difference is likely to be caused by the difference in contour length of the two molecules, and provides strong evidence that the observed blockades of ionic current are indeed caused by translocation of DNA molecules from the *cis* to the *trans* side of the pore. Note that the difference in contour length of these two molecules is about a factor of 4. The long molecules thus appear to translocate with a lower average velocity than the short ones. Our results are in good agreement with Li *et al.* [21], who attribute the spread of events to strands of DNA that are partially folded back onto themselves during translocation. It is interesting to note that a much fainter second band of events is apparent in Fig. 4.7e at roughly double the time scale as the first band. We speculate that complementary sticky ends present on the λ-DNA cause occasional binding of two DNA molecules. This would explain the second band of events at longer dwell times compared to the main band.

The sorting algorithm described in the methods section allows us to study well-defined subsets of all measured events. First we take a look at the most simple events, those of type '1'. These events are straightforwardly interpreted as simple linear translocations of molecules from one end to the other, without any folding. Fig. 4.8a and 4.8d show a scatter plot of events of type '1' for the 11.5 kbp and 48 kbp data sets respectively (plotted in grey). In Fig. 4.8b and 4.8e the histograms of t_{dwell} are plotted and in Fig. 4.8c and 4.8f, we show a histogram of the areas. In a similar way we analyzed events of type '2', which are interpreted as molecules folded exactly in the middle. It should be noted that λ-DNA has single-strand 'sticky ends' at both ends, and that these ends can bind to form circular DNA. Translocation events from circular molecules are expected to look identical to molecules folded exactly halfway (see also the data on circular DNA discussed below). The '2' results were plotted in black in the same graphs as the type '1' events for comparison. For both

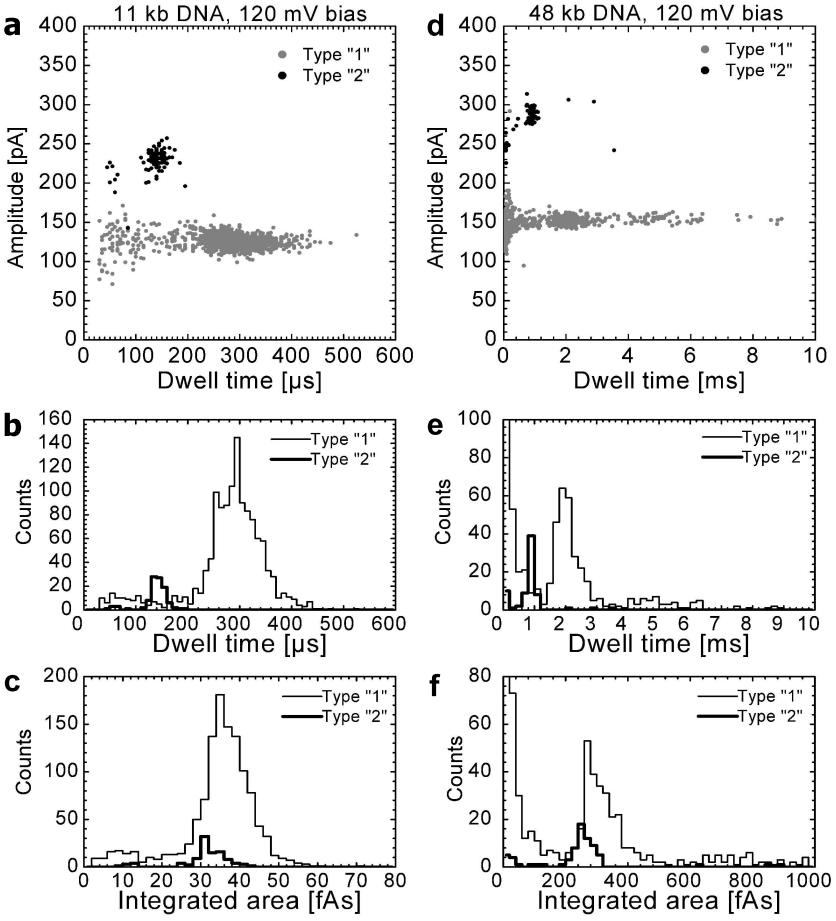

Figure 4.8: (a) Event scatter plot of type '1' (grey) and type '2' (black) events recorded at 120 mV with 11.5 kbp linear DNA molecules. (b) Histogram of observed dwell times for '1' and '2' events. (c) Histogram of the area (integrated signal) of events of type '1' and '2'. (d) Event scatter plot of type '1' (grey) and type '2' (black) events recorded at 120 mV with 48 kbp linear DNA molecules. (e) Histogram of observed dwell times for '1' and '2' events. (f) Histogram of the area (integrated signal) of events of type '1' and '2'.

11.5 kbp DNA ($N = 1855$)

Type	Number	% of total	t_{dwell} [μs]	width t_{dwell} [μs]	Area [fAs]	width Area [fAs]
'1'	1186	63.9	292	76	36.5	9.6
'2'	102	5.5	143	24	32.1	5.5
'21'	513	27.7	[a]	[a]	35.0	7.9
'12'	4	0.2	[b]	[b]	[b]	[b]

48 kbp DNA ($N = 1598$)

Type	Number	% of total	t_{dwell} [ms]	width t_{dwell} [ms]	Area [fAs]	width Area [fAs]
'1'	633	39.6	1.96	0.55	298	89
'2'	72	4.5	0.90	0.23	258	56
'21'	683	42.7	[a]	[a]	285	68
'12'	4	0.3	[b]	[b]	[b]	[b]

[a]) Wide non-Gaussian distribution.
[b]) Too few events were detected for reliable fitting.

Table 4.1: Summary of experimental results: Events detected for 11.5 kbp and 48 kbp DNA were sorted to type. The average dwell time and area were determined by fitting the appropriate histograms to a Gaussian.

data sets, we fitted a Gaussian to the peaks in the dwell time and the area histograms. The results are shown in Table 4.1. We see that, for both molecules, the dwell time of '2' events equals about half the time of the '1' events. Additionally, the areas are almost constant: If we look at the integrated area for both types of events displayed in Fig. 4.8c and Fig. 4.8f, we find a difference of less than 10% between type '1' and '2'. Apparently, the average velocity of the molecules is almost identical for folded and straight DNA translocations.

Another type of event that frequently occurs is the '21' event, i.e., blockades where we first observe a deep blockade at the second level, followed by a plateau at the first level. These events fall in between the '1' and '2' events in the scatter plot (Compare Fig. 4.9a and 4.9d to Fig. 4.8a and 4.8d). Now we define t_1 as the duration of the first sub-event (at level '2') and t_2 as the duration of the second sub-event (at level '1'). Fig. 4.9b and 4.9e show t_2 versus t_1 for 11.5 kbp

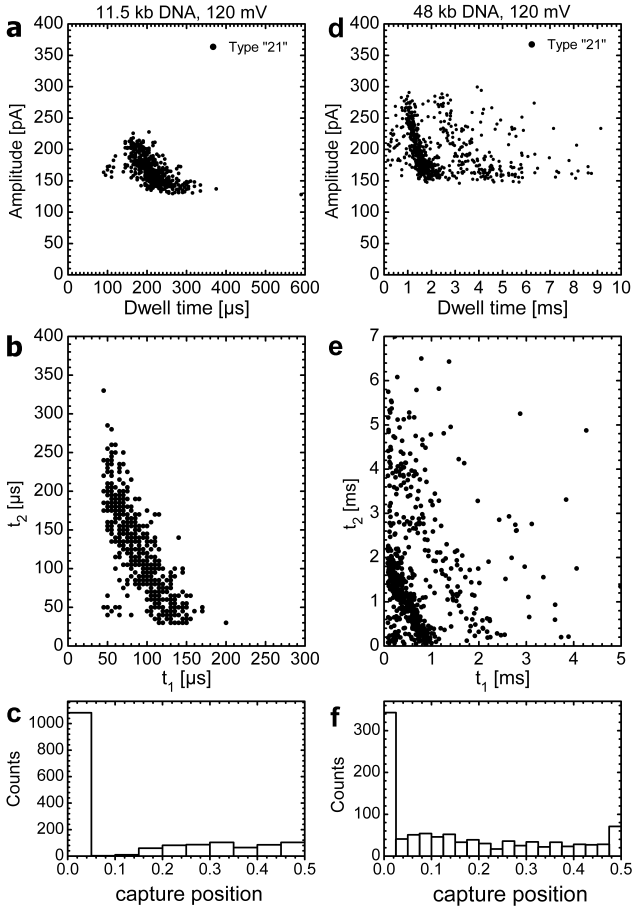

Figure 4.9: (a) Event scatter plot of type '21' events recorded at 120 mV for 11.5 kbp DNA. (b) The duration of the first (t_1) and second (t_2) plateau within the '21' type events were determined, and plotted as a scatter plot. (c) Calculated capture position for 11.5 kbp DNA. (d) Event scatter plot of type '21' events recorded at 120 mV for 48 kbp DNA. (e) The duration of the first (t_1) and second (t_2) plateau within the '21' type events were determined, and plotted as a scatter plot. (f) Calculated capture position for 48 kbp DNA.

and 48 kbp DNA, respectively. For both molecules, we observe a linear relation between the two. We interpret these '21' events in the following way: DNA passes the pore in a folded state. First, the double part of the molecule passes the pore, followed by the residual linear part of the molecule, see Fig. 4.5d. It is interesting to note that events of type '12' are rare, see Table 4.1. It thus appears that once translocation starts in a linear fashion, capture of the other end in the pore is quite unlikely.

In Table 4.1, we summarize our findings. It appears that more than 85% of events can be identified under the simple assumption that a molecule passes the pore either linearly or with a single fold. We now estimate the position of the fold along the molecule from the measured event. We define the capture position as x/L, where x is the distance from the folding point to the nearest end of the molecule and L is the total contour length. Linear, unfolded translocations of type '1' have a fold position of 0, and type '2' translocations a fold position of 0.5. To estimate the capture position from type '21' we assume that the first 'double' plateau is related to the passage of two double-strands with length x in parallel, and that the following single blockade is the residual part of the molecule with length $(L - 2x)$. Assuming constant velocity, the capture position can now be estimated as $t_1/(2t_1 + t_2)$. In the histogram in Fig. 4.9c and 4.9f we show the result of this analysis, compiling results for '1', '2' and '21' type events, for both 11.5 kbp and 48 kbp DNA respectively. Disregarding the positions 0 and 0.5 for the moment, we see a distribution that is roughly uniform within the experimental error. Note that the absence of events with a folding location around 0.1 in the case of 11.5 kbp DNA is caused by the finite time resolution of the electronics. Events of type '21' where the double part occupies the pore for less than about 50 μs are likely to be detected as '1' events.

Since DNA is coiled up randomly in solution, one would expect that the distribution of fold locations is completely flat. We see however that unfolded molecules (capture position 0) appear about 10 times more often than expected. Apparently, it is more likely to initiate the translocation of a DNA molecule at one of its ends than at another position. We speculate that the kink in the DNA that is necessary for entry in a folded state causes a considerable energy barrier in the translocation process. This may explain the difference

in frequency for folded and unfolded translocations.

Additionally, we find that for 48 kbp DNA, a fold position around 0.5 is about a factor of 2 more likely than other nonzero folding positions. This feature can be accounted for by the presence of a small fraction of λ-DNA molecules in a circular state. λ-DNA contains complementary 'sticky ends' of about 10 bases at both ends of the molecule, which promote the formation of circular DNA. We do not observe this feature for the 11.5 kbp sample, since the restriction enzyme that linearizes the vector leaves sticky ends of only 4 bases, which are too short for any detectable fraction of circular DNA. Complementary sticky ends of λ-DNA also explain the pronounced second band of events in Fig. 4.7. We attribute this to events that are caused by two λ-DNA molecules bound together.

4.3.2 Influence of the voltage driving the translocation

The driving force for the translocation process is the electrostatic force on the small part of the negatively-charged DNA molecule that is located inside the pore. This driving force can be varied by varying the bias voltage that is applied over the pore. To demonstrate the influence of the driving voltage on the translocation, the following experiment was performed. After collecting the translocation-data on 48 kbp linear λ-DNA at a voltage of 120 mV discussed above, we reduced the bias voltage to 60 mV, a factor of two lower. At this lower voltage, translocations occur much less frequently. Fig. 4.10a shows a scatter plot of dwell time and amplitude of the 307 events collected at this voltage. For comparison the results for translocation events recorded at 120 mV are shown again in Fig. 4.10d-f. The general shape of the distribution related to the folding of DNA is similar, but the magnitude of both time and amplitude have changed. We now find amplitudes between 75 pA and 150 pA, half of the 150 pA to 300 pA obtained for the 120 mV translocations. This is explained by the notion that passing molecules change the ionic conductance of the pore. Therefore a reduction of the driving voltage by a factor of two will lead to a reduction of the measured current by the same factor. The main peak in the dwell time histogram of the 60 mV data is between roughly between 2 and 4 ms, a factor of two longer than at 120 mV. Clearly, the reduced voltage gives rise to slower translocations. The data suggests that the dwell time is roughly inversely

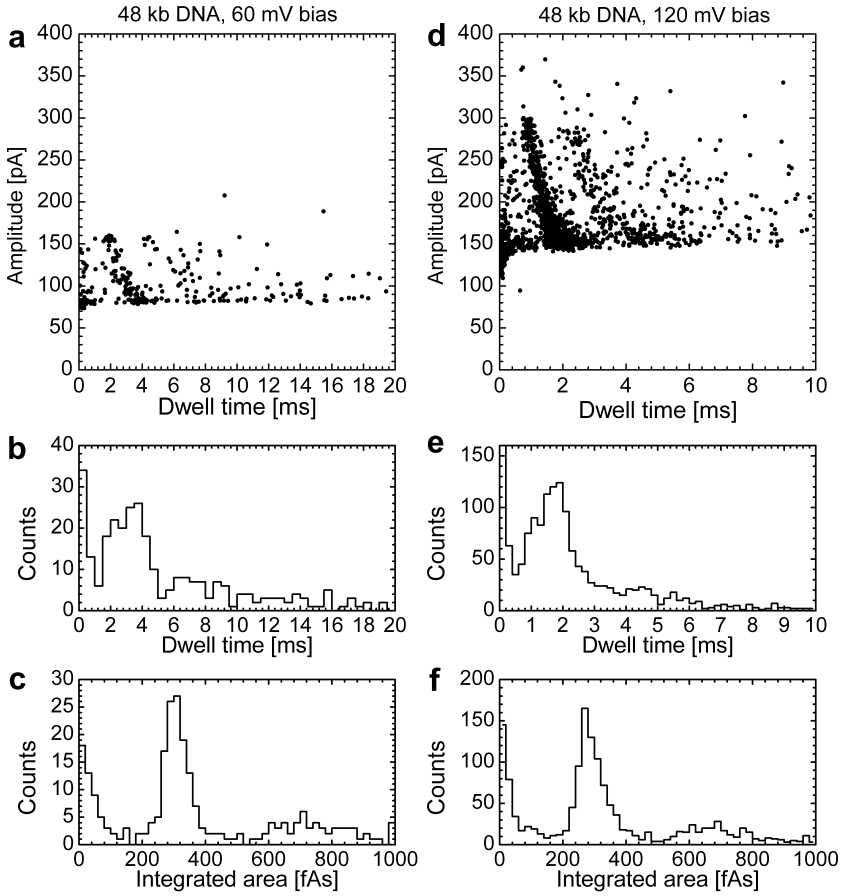

Figure 4.10: (a) Event scatter plot of events recorded at 60 mV with 48 kbp linear DNA molecules. (b) Histogram of observed dwell times at 60 mV. (c) Histogram of the area (integrated signal) of events at 60 mV (d) Event scatter plot of events recorded at 120 mV with 48 kbp linear DNA molecules. (e) Histogram of observed dwell times at 120 mV. (f) Histogram of the area (integrated signal) of events at 120 mV.

proportional to the voltage difference, but more data with a wider range of voltages is required to make this claim more quantitative. Note that the integrated-area histograms Fig. 4.10c and 4.10f are about equal.

4.3.3 Circular DNA translocation events

As a further test of the folding model, we conducted another experiment with circular double-strand DNA of 11.5 kbp length and an 8 nm pore. Circular DNA can exist in various isomers, since the loop can contain a number of different 'twists' [1]. This supercoiling effect has a large effect of the structure of the molecule. To circumvent these effects we worked with double-strand DNA with one nick: The backbone of one of the two strands contains a single break, allowing supercoils to relax. This way we can be sure to have DNA molecules in an identical state. Repeating our nanopore experiment with a bias voltage of -120 mV on this nicked circular DNA, we again observe clear blockage events. With the same data analysis described earlier, t_{dwell} and I_{block} were determined for all events, and the results are plotted in Fig. 4.11. The distribution of events appears to be qualitatively different from the distribution observed for linear molecules. Instead of a band of events, we detect primarily type '2' events. The average dwell time is around 190 μs and the amplitude is around 120 pA. The value for the dwell time agrees reasonably well with the value of 143 μs for type '2' events for the linear molecules. The value for the amplitude however significantly deviates from the 240 pA observed for the linear molecules. We attribute this difference to differences between the pores that were used. The diameter of the pore was 8 nm in this experiment, slightly smaller than the 10 nm pore that was used for the linear molecules. The length of the pores however is not well known and a sizeable difference could explain the difference in amplitudes.

4.3.4 Nanopore experiment on a polydisperse DNA mixture

The observation that the dwell time increases with increasing length of DNA suggests that nanopores can be used to determine the lengths of unknown fragments, analogous to traditional gel electrophoresis.

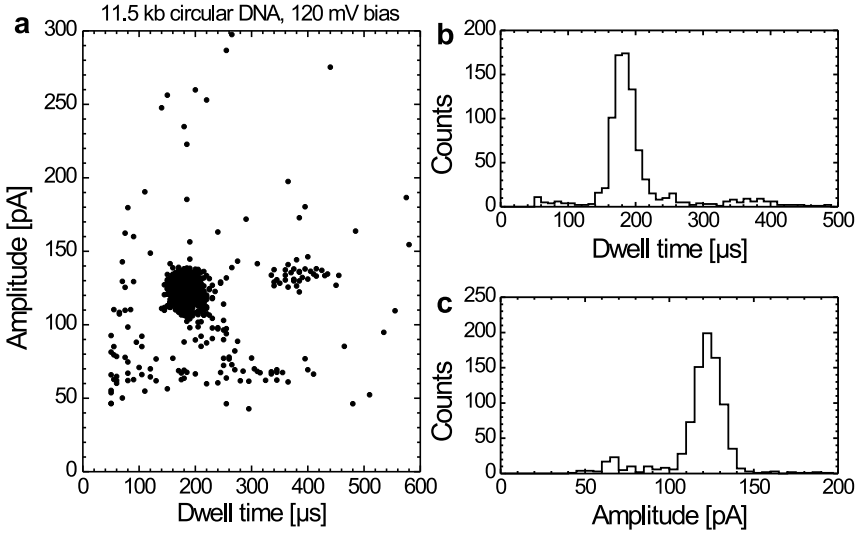

Figure 4.11: (a) Event scatter plot of events recorded at 120 mV with 11.5 kbp circular DNA molecules. (b) Histogram of observed dwell times (c) Histogram of the amplitudes.

As a first evaluation, we analyzed translocation events recorded on a mixture of DNA fragments with known sizes. A commercially available mixture of DNA 'markers' for gel electrophoresis was tested. The mixture contains fragments that remain after incubation of λ-DNA with the HindIII restriction enzyme. The mixture contains fragments of sizes: (1) 23130 bp, (2) 9416 bp, (3) 6557 bp, (4) 4361 bp, (5) 2322 bp, (6) 2027 bp, (7) 564 bp and (8) 125 bp . Because linear λ-DNA contains single-strand 'sticky-ends', fragments (1) and (4) can bind together to form effectively a 27491 bp fragment. We performed a gel electrophoresis experiment in order to determine the amount fragments bound in our sample. Fig. 4.12 shows the gel results for the mixture as supplied (left lane) and after a short heating to about 60°C (right lane). We find that indeed fragments (1) and (4) are bound together almost completely in the material before heating. We conclude that the following fragment sizes are present in the material as supplied: 27491 bp (1+4), 9416 bp (2), 6557 bp (3), 2322 bp (5), 2027 bp (6).

A nanopore translocation experiment was carried out in the man-

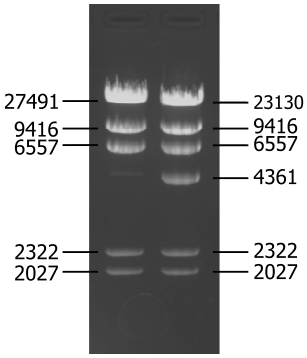

Figure 4.12: Gel electrophoresis on the DNA mixture. The left lane shows the DNA mixture as supplied, the right lane contains the same mixture that was heated to about 60°C and cooled shortly before loading. The nanopore experiments were performed on material as supplied. Note that without the heat treatment the fragments of 4361 bases and 23130 bases are bound together to a single molecule of 27491 bases.

ner reported in the preceding sections using the DNA mixture as supplied, without heating. Events were analyzed with the same protocol as discussed in section 4.2.4. First, we look at the distribution of dwell times for type '1' events (linear translocations without folding). The histogram shown in Fig. 4.13 shows the result of this analysis. Quite clearly we observe 4 peaks at 1 ms, 260 μs, 160 μs 45 μs, and we identify these peaks as caused by fragments (1+4), fragment (2) fragment (3) and fragment (5,6) respectively. The fragments (5) and (6) have a comparable length and probably cause a single peak in the histogram. Fig. 4.13b shows an integrated area histogram from all measured events, again showing at least four clear peaks.

4.4 Discussion

From the DNA-mixture experiment, it is apparent that the longer the DNA, the longer the translocation time. To make this claim more quantitative, we compile the average dwell-times observed for all linear type-'1' translocations in Fig. 4.14. We find a nonlinear behavior for the translocation time t_{dwell} as a function of the length L.

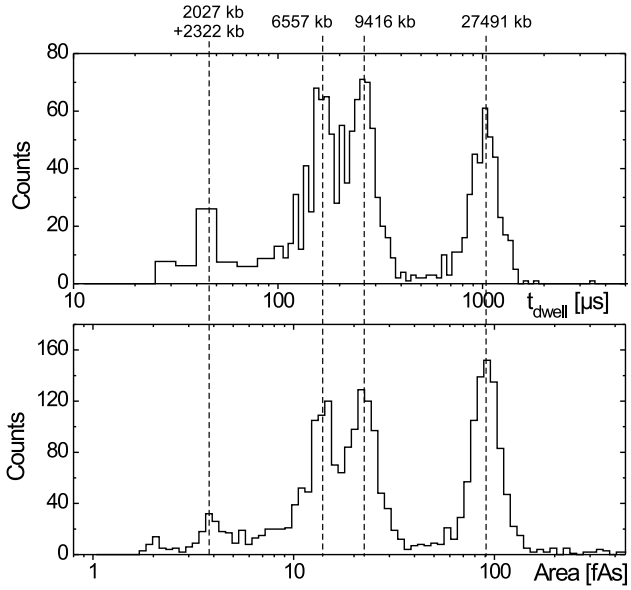

Figure 4.13: Top panel: Histogram of dwell times of type '1' events obtained with a mixture of DNA molecules. The four peaks can be identified with the longest fractions of DNA present in the mixture. Bottom panel: Histogram of the areas measured for all detected events.

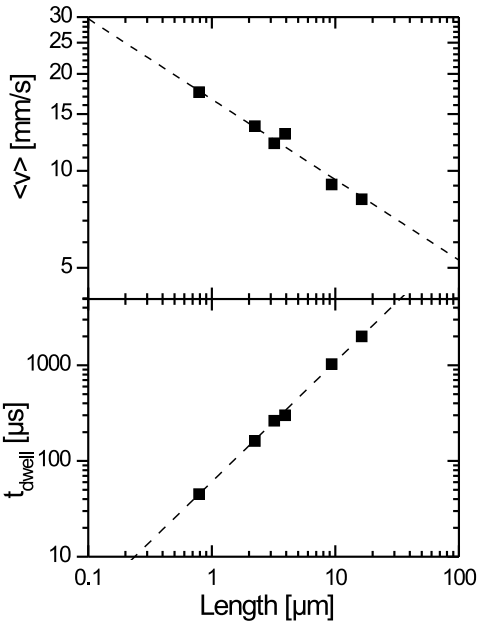

Figure 4.14: Average velocity and dwell time vs. DNA length. t_{dwell} was taken as the most probable dwell time for a molecule, i.e. the location of the peak in the dwell time histogram. The average velocity $\langle v \rangle$ is calculated as L/t_{dwell}.

The straight line on the log-log plot shows a power law ($t_{\mathrm{dwell}} \sim L^{\alpha}$) fit to the data, with an exponent α of 1.26. Fig. 4.14 also shows the average translocation velocity calculated as $\langle v \rangle = L/t_{\mathrm{dwell}}$ for all molecules.

We now compare these results to published data on single-strand DNA and RNA translocation through α-hemolysin. Firstly, there is a large difference in translocation velocity. At a driving voltage of 120 mV, nucleic acids thread the pore α-hemolysin at a rate of about 1 base per microsecond [22], equivalent to about 0.5 mm/s. This is much slower than the 10 mm/s that we observe for double-strand DNA. This effect can be explained by a difference in effective friction between the polymer and the pore. α-Hemolysin appears to have strong specific interactions with the passing polymers. We expect that DNA in solid-state pores experiences only hydrodynamic friction. Another difference is that the translocation time scales linearly

with length in the case of α-hemolysin [5, 24], for polymers longer than about 12 nucleotides. In chapter 5, we discuss the modeling of polymer translocation through nanopores in more detail and present a new model that explains the observed power-law scaling between the dwell time and DNA length.

4.5 Conclusions

To summarize, we have observed single-molecule DNA translocation events through silicon oxide nanopores fabricated by our new TEM shrinking technique. Using nanopores of about 10 nm diameter we have detected translocation events for DNA fragments of 11.5 kbp and 48 kbp. The distribution of both the event duration and their amplitude can be qualitatively well understood if we take folding of the molecules into account. A detailed analysis of the exact shape of the event can then be used to estimate the fold position. In future, similar techniques might be applied to address the folding of RNA or even polypeptides.

Moreover, we demonstrate that a nanopore-based detector can be used analyze polydisperse mixtures of DNA, with fragment sizes from 2 kbp to about 27 kbp. In this experiment we analyse the translocation of about 2500 individual DNA molecules ($3{\cdot}10^{-14}$ g) and find a clear separation in length. This result proves the remarkable sensitivity of nanopores, although the resolving power is not yet up to standards set by traditional gel electrophoresis.

Finally, analysis of all translocation data shows that for unfolded translocations, the duration t_{dwell} scales with the length L as $t_{\mathrm{dwell}} = L^{\alpha}$, with an exponent α of 1.26. This behavior is in disagreement with existing models for translocation, and suggests that a different mechanism dominates the translocation dynamics in these experiments. Understanding the underlying physics of the translocation process is relevant for the development of future nanopore-based detectors.

Acknowledgements

The nanopores for this research were fabricated in collaboration with Jianghua Chen and Henny Zandbergen. We would like to thank the

groups of D. Branton and J.A. Golovchenko at Harvard University for their hospitality and advice on nanopore experiments. We also thank John van Noort, Peter Veenhuizen, Nynke Dekker, Dick Korbee and Kees Storm for their support and discussions.

Chapter 5

Fast DNA translocation through a solid-state nanopore

Abstract

We report translocation experiments on double-strand DNA through a silicon oxide nanopore. DNA fragments with seven different lengths between 2000 to 96000 base pairs have been electrophoretically driven through a 10 nm pore. We find a power-law scaling of the translocation time versus length, with an exponent of 1.26 ± 0.07. This behavior is qualitatively different from the linear behavior observed in similar experiments performed with protein pores. We propose a new theoretical model which is based on a force balance between the driving force and the Stokes drag on the coiled-up polymer. The model is valid for translocation that are fast compared to the characteristic relaxation time of the polymer. We show that this is the case in our experiments and derive a power-law scaling with an exponent of 1.18, in excellent agreement with our data.

5.1 Introduction

Translocation of biopolymers such as polypeptides, DNA, and RNA is an important process in biology. Transcribed mRNA molecules for example are transported out of the nucleus through a nuclear pore complex. Viral injection of DNA into a host cell is another example. Translocation of DNA and RNA can be studied in vitro, as demonstrated by Kasianovic *et al.* [5] using an α-hemolysin pore in a lipid membrane. By measuring the ionic current through a voltage-biased nanopore, one can detect individual single-strand molecules that are pulled through the pore by the electric field. Li *et al.* [13, 21] showed that solid-state nanopores can also be used for such experiments. We report a set of experiments with silicon oxide nanopores on double-strand DNA with various lengths. Surprisingly, we find a nonlinear scaling between the translocation time τ and the polymer length L, in contrast to the linear behavior for all experiments with α-hemolysin [5, 24]. In our experiments we find a clear power-law relation $\tau = L^{1.26}$, for DNA fragments from 2000 to 96000 base pairs. We propose a new model for translocations that are fast compared to the polymer relaxation times. While a complete model for translocation should in principle include hydrodynamic, steric, electrostatic and entropic effects, our model is based on the assumption that hydrodynamic-drag effects dominate in the fast regime. We find excellent agreement with our experimental data.

5.2 Experimental results

Figure 5.1a shows the experimental layout for translocation studies. At the heart of the setup is a solid-state-nanopore device, fabricated by shrinking a 20-50 nm pore in silicon oxide in a transmission electron microscope to a final size of 10 nm [25]. The nanopore is situated in an insulating membrane which separates two macroscopic reservoirs filled with an aqueous buffer solution. When a voltage bias is applied over the membrane in the presence of DNA molecules in the negative compartment, the DNA is electrophoretically drawn through the pore due to its negative charge. The detection technique is simple and elegant: A polymer inside the pore lowers the amount of conducting solution present inside the pore and thus reduces the

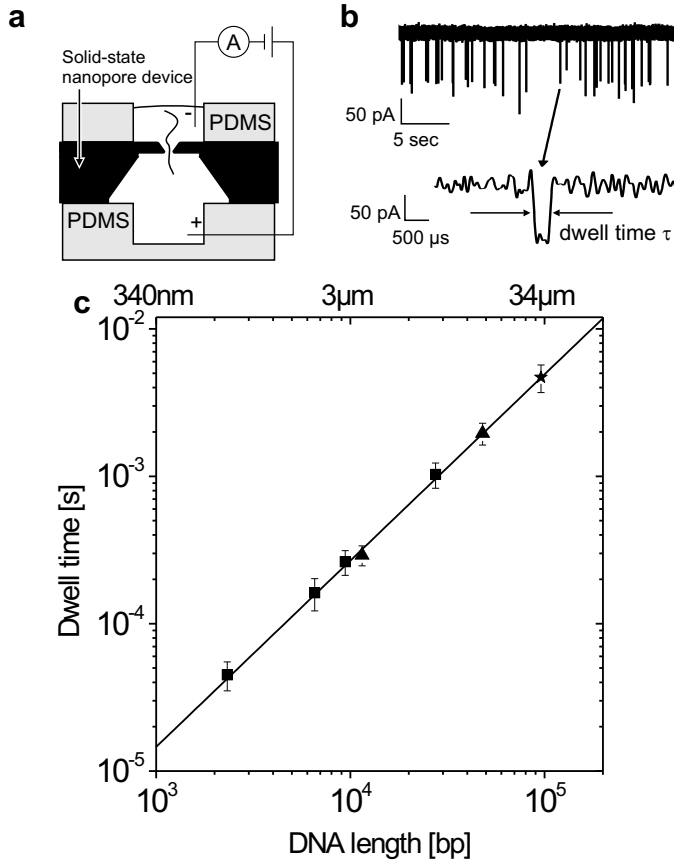

Figure 5.1: (a) Cross-sectional view of the experimental setup (not to scale). A negatively-charged DNA molecule is electrophoretically driven through a 10 nm aperture in a silicon device, which is located between two reservoirs kept at a potential difference. Both reservoirs are filled with an aqueous buffer solution (1 M KCl, 10 mM Tris-HCl pH 8.0, 1mM EDTA). (b) Measured ionic current versus time, after the addition of 4 μm (11.5 kbp) DNA to the top reservoir. An individual event is shown with increased time resolution. (c) Dwell time vs. polymer length. Square datapoints (■) were collected on a mixture of DNA fragments, as discussed in section 4.3.4. Triangular (▲) data points are obtained in two separate experiments on DNA of 11.5 kbp and 48 kbp respectively. The point at 96 kbp (★) was obtained from dimers of 48 kbp λ DNA. The line shows the result of a power-law fit to the data.

ionic conductivity between the reservoirs. Passing molecules are thus detected as short dips in the ionic current, which is induced by the externally applied voltage (see Fig. 5.1b). Analogous to Li *et al.* [21], we find that the molecules with a diameter of about 2 nm can pass the 10 nm pore either in a linear or in a folded fashion. Using an event sorting algorithm discussed in the previous chapter, we analyse only the linear unfolded translocation events in this work. Fig. 5.1b shows an example of such a linear translocation event, detected with 11.5 kbp linear DNA. The width of the dip is interpreted as the duration of the translocation. We performed three experiments, all at room temperature: One on linear 11.5 kbp DNA, one on linear 48 kbp λ-DNA (here we detected both individual molecules and dimers of two molecules bound with complementary sticky ends), and one on a mixture that contains 27491 bp, 9416 bp, 6557 bp, 2322 bp, and 2027 bp fragments. In the last experiment, the length difference between the 2322 bp and 2027 bp fragments could not be resolved experimentally. The durations of individual linear events were collected in a histogram for each experiment. Figure 5.1c shows the dwell time (determined as the peak position in these histograms) versus polymer length for all seven DNA fragments that were studied. The full width at half maximum of the peaks are taken as error bars. We find a clear power-law scaling of the dwell-time τ with the length L, $\tau \sim L^{\alpha}$, with a value of 1.26 ± 0.07 for the exponent α. Details of the experiments are discussed in chapter 4. It is interesting to note that our results are in good agreement with those reported by Li *et al.* [21]. She has studied the translocation of 3000 bp and 10000 bp DNA through a 10 nm silicon nitride nanopore, and finds translocation times of 100 μs and 400 μs respectively.

5.3 Slow versus fast translocations

The translocation process consists of two separate stages. First, there is the capture stage. A DNA molecule initially in solution in the negative reservoir has to come close enough to the pore to experience the electrostatic force and get pulled in. We assume that the reservoirs are good ionic conductors, and the driving force is only felt in the direct vicinity of the pore. Capture is thus a stochastic process, since the pore has to be reached by diffusion. In this work, we focus on

the second stage, where the DNA passes the pore until it has reached the other side. We assume that an end of the DNA has entered the pore and calculate the time required for complete translocation.

We now address the dependence of this duration on the length of the polymer. To this end, we consider a linear polymer consisting of N monomers, each of which has a Kuhn length b. This polymer is partially threaded through a narrow pore. Time $t = 0$ sets the moment of initial capture. We will let $L(t)$ denote the contour length of the untranslocated part of the polymer, so that $L(0) = Nb \equiv L_0$. The dwell time τ is therefore determined by $L(\tau) = 0$. A second time scale in the problem is the characteristic relaxation time scale of the translocating polymer. This Zimm time [26], given by

$$t_Z \approx 0.4 \frac{\eta R_g^3}{k_B T} \tag{5.3.1}$$

can be considered an upper bound on the time it takes the polymer to relax to an entropically and sterically favored configuration. In this expression, η is the solvent viscosity and R_g is the so-called radius of gyration of the polymer. This is the radius of the typical blob-like configuration that the polymer will assume in a good solvent, and it scales with the polymer length as

$$R_g \sim L^\nu \tag{5.3.2}$$

which defines the Flory exponent ν. It depends on the dimensionality of the system, and theoretically a value of 0.588 is found for self-avoiding polymers in a good solvent [27].

In previous experiments on the α-hemolysin proteinaceous pore, it was found that the translocation velocity depends on the base sequence of the polynucleotide. At room temperature, the measured velocity is about 0.8 μs per base or slower [22]. A 100-base, single-stranded DNA fragment therefore takes around 80 μs to fully translocate. When we compare this to the Zimm time for the same polymer fragment, about 0.2 μs, we see that relaxation is much quicker than the translocation. We denote such events, for which $\tau \gg t_Z$, as *slow* translocations.

The criterion for slow translocation is evidently not met in our experiments on sold-state nanopores. A full λ-phage genome (48.5 kbp, or 16.5 μm of double-stranded DNA) is found to take only

around 2 ms to traverse a 10 nm SiO_2 pore. The Zimm time for this molecule, in comparison, is about 700 ms, clearly much longer than the translocation time. We therefore refer to this second regime, where $\tau \ll t_Z$, as *fast* translocations. We should point out that an important reason for the fastness of our system is the fact that we use double-stranded DNA, which has a much larger persistence length than single-stranded DNA and consequently has a long relaxation time.

5.4 Prior work on slow translocations

Most previous work has focussed on slow translocations. While a full review is beyond the scope of this chapter it is useful to briefly recall some of the most relevant insights. The basic process as depicted in Fig. 5.1a may at first glance appear simple, but modeling the system is far from straightforward. Processes that in principle have to be considered include the electrostatics of the driving force, both hydrodynamic and contact friction of the polymer inside the pore, specific interactions between the polymer and the pore (such as hydrogen bonding and hydrophobic interactions), hydrodynamic drag of the dangling polymer outside the pore, and diffusive motion of the polymer as a whole.

In the absence of driving, the process reduces to the 1D diffusion of a particle over a barrier, and the translocation time scales with the length as $\tau \sim L^2$ [28]. The case of high friction is of particular relevance to the α-hemolysin pore, which appears to have strong specific interactions with the passing DNA. This translates into a high effective friction coefficient inside the pore, and is the primary reason why translocation is slow in these systems. Even at high driving forces the translocation is entirely limited by the rate at which single bases can pass through the pore, and it is therefore intuitively clear that the translocation time should scale linearly with the polymers length, $\tau \sim L$.

Lubensky and Nelson [29] have argued that for single-stranded DNA and RNA through α-hemolysin, the criterium for slow translocation is indeed satisfied for polymer lengths up to hundreds of nucleotides. They show that the Zimm time for a polynucleotide of roughly 300 bases is comparable to the translocation time per nu-

cleotide, which justifies the use of diffusive models to describe the translocation of polynucleotides up to those lengths. Experiments by Kasianowicz [5] and Meller [24] have shown that the translocation time does indeed scale linearly with the contour length for homopolymers in the range of 12 to 400 bases, in good agreement with the prediction for strongly driven, slow translocation.

5.5 Fast translocations

In strong contrast, our results on double-stranded DNA through solid-state nanopores show a significant *non*linear dependence of the translocation velocity on the polymer length, as evidenced by Fig. 5.1c. We find a power-law dependence, $\tau \sim L^{\alpha}$, with α=1.26 $\pm$ 0.07. This behavior is observed over the entire range of lengths probed, covering almost two decades. The shortest detected molecules were 2000 bp long, which corresponds to a Zimm time of just over 2.3 ms. The translocation time however was found to be 50 μs, significantly shorter. The same is found for the longer molecules - for the 48.5 kbp λ DNA the observed translocation time of 2 ms is much shorter than the Zimm time, which in this case is approximately 700 ms. Evidently, these events can be considered fast translocations for all lengths considered.

To our knowledge, only Kantor and Kardar [28] have addressed the regime of fast polymer translocation. They argue that the translocation time scales as $N^{1+\nu}$ when the process is driven by a difference in chemical potential, which is essentially the same as a localized force at the pore. This thus predicts an exponent of around 1.6, in disagreement with the experimental results. In the following section, we present a new model for fast translocations, which appears to capture the experimental results better. The principal difference with Kantor and Kardar's approach is that we explicitly take hydrodynamic friction effects into account.

5.6 Model

We now estimate the magnitudes of the possibly relevant forces, following Lubensky and Nelson. First, we consider the driving. As stated, a potential difference across the pore exerts a highly localized

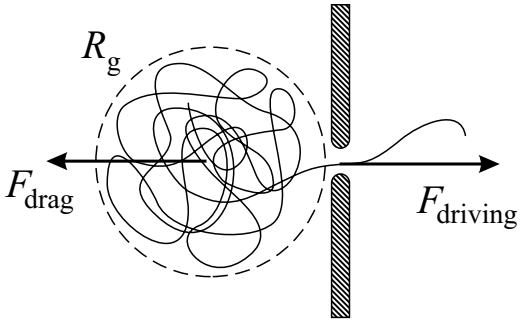

Figure 5.2: At time t the DNA on the left side of the pore has a radius of gyration of R_g, indicated by the dashed line. The balance between the two dominating forces determines the dynamics: A driving force that locally pulls the DNA through the pore and a viscous drag force that acts on the entire DNA blob.

force on the negatively charged DNA molecule. We assume the potential drop to occur entirely inside the pore, and therefore only the part of the polymer inside experiences the driving force. This force can then be estimated as $F_{\text{driving}} = 2eV/a$, where e is the elementary charge, V is the potential difference and $a = 0.34$ nm is the spacing between nucleotides. A bias voltage of 120 mV, as is typically used in experiments, thus produces a force of around 110 pN. This value is an upper bound of the actual force, as screening effects may greatly reduce the effective charge on the DNA, and thereby the driving force. Simulations of Manning condensation on double-stranded DNA yield charge reductions values between 53% and 85% [3, 4]. Barring complete screening however, we can consider our DNA translocations to be strongly driven which justifies ignoring diffusive contributions.

In the absence of specific DNA-pore interactions, the viscous drag per unit length in the pore can be estimated as $2\pi\eta rv/(R-r)$, where R is the pore radius, r is the polymer cross-sectional area, η the solvent viscosity and v is the linear velocity of the polymer inside the pore. Substituting typical values ($\eta = 1.10^{-3}$ Pa·s, $r = 1$ nm, v=10 mm/s, R=5 nm and a pore depth of 20 nm) we can estimate this drag force to be around 0.3 pN, decidedly smaller than the driving force. We feel this constitutes an essential difference between solid-

state pores and protein pores: In sufficiently shallow solid state pores the effect of hydrodynamic friction inside the pore is negligible.

Finally we estimate the hydrodynamic drag on the untranslocated part of the polymer, outside the pore. To this end, we approximate the untranslocated part as a sphere of radius R_g (see Fig. 5.2). As the polymer threads through the pore, the center of mass of this sphere moves towards the pore at a velocity $\mathrm{d}R_g/\mathrm{d}t$, and thus by Stokes' law should experience a drag force of $6\pi\eta R v = 6\pi\eta R_g \mathrm{d}R_g/\mathrm{d}t$, which for typical parameters yields a drag force of about 24 pN. Clearly, in this case the hydrodynamic part of the polymer outside the pore is the dominant force counteracting the driving force. We therefore choose to model fast translocation dynamics as determined only by the cumulative effect of driving at the pore and hydrodynamic friction outside.

Figure 5.2 depicts the simplified system that we consider. The part of the polymer inside the pore experiences a driving force to the right, while the length of polymer before the pore is coiled up. The pore is sufficiently small to allow only linear (*i.e.* unfolded) passage of a single molecule at a time.

As the polymer is pulled through the pore, the blob before the entrance shrinks in size, and thus its center of mass moves towards the pore with a velocity

$$v_{\mathrm{blob}} \sim \dot{R}_g = L^{\nu-1}\dot{L}, \tag{5.6.1}$$

where the dot denotes a time derivative. Motivated by our consideration of the relative magnitudes of the counteracting forces, we propose that the principal effect of hydrodynamics is to resist motion with a Stokes drag on the DNA coil that is proportional to its radius times the velocity,

$$\begin{aligned} F_{\mathrm{drag}} &\sim R v_{\mathrm{blob}} = R_g \dot{R}_g \\ &\sim L^{2\nu-1}\dot{L}. \end{aligned} \tag{5.6.2}$$

Force balance must be met at all times, and since there are only two major forces, the driving force should balance the hydrodynamic friction: $F_{\mathrm{drag}} = -F_{\mathrm{driving}}$. As the driving force is constant during the whole process, the same holds for F_{drag}. Thus we can extract the linear velocity $v_{\mathrm{lin}} = -\dot{L}$ of the DNA inside the pore from Eq. (5.6.2):

$$v_{\mathrm{lin}} = -\dot{L} \sim -L^{1-2\nu}, \tag{5.6.3}$$

which allows us to obtain the dwell time τ by integration,

$$\tau = \int_0^\tau \mathrm{d}t = \int_{L(0)}^{L(\tau)} \frac{\mathrm{d}t}{\mathrm{d}L}\,\mathrm{d}L = \int_{L_0}^{0} v_{\mathrm{lin}}^{-1}(L)\,\mathrm{d}L$$

to yield

$$\tau \sim L_0^{2\nu}. \tag{5.6.4}$$

On the basis of this model we thus predict a power-law relation between the dwell time τ and the contour length L_0. Taking the theoretical value of 0.588 for the Flory exponent ν, we find an exponent of $\alpha = 2\nu = 1.18$ for this model. This is in excellent agreement with our experiments, where we find power-law scaling with an exponent of 1.26 ± 0.07.

5.7 Concluding remarks

We have obtained a simple and elegant model description that appears to describe our data well. There are several effects we neglect but which could have an additional influence on the process that we consider. For instance, we ignore any friction experienced by the DNA that has already passed the pore. We also expect that an electro-osmotic flow will be generated inside the pore. This effect is caused by an electrophoretic force on the ions screening the charge on the surface of our pore. As silicon oxide is known to be negatively charged in water, there is a surplus of positive ions near the surface. These positive ions generate a flow of water inside the pore, slowing down the DNA that moves in the other direction. While we have not explored the consequences of these possibilities, the observed agreement between theory and experiment suggests that at least for the fast polymer translocations considered here, the hydrodynamic drag does indeed dominate the dynamics. Identification and understanding of the dominant effects in polymer translocation through nanopores is relevant not only for biological processes, but also for potential analytical techniques based on nanopores. Rapid oligonucleotide discrimination on the single-molecule level has been demonstrated with α hemolysin [22], and more recently solid-state nanopores were used to study folding effects in double-stranded DNA molecules [21] (see also chapter 4). Future applications of this technique may include DNA size determination, haplotyping and sequencing.

Acknowledgements

The theoretical work presented in this chapter is done in close collaboration with Cornelis Storm and Jean-François Joanny at the Curie Institute in Paris. We would like to thank Nynke Dekker, Sean Ling, John van Noort and Peter Veenhuizen for their support and discussions.

Chapter 6

Insulating behavior for DNA molecules between nanoelectrodes at the 100 nm length scale

Abstract

Electrical transport measurements are reported for double-strand DNA molecules located between nanofabricated electrodes. We observe the absence of any electrical conduction through these DNA-based devices, both at the single-molecule level as well as for small bundles of DNA. We obtain a lower bound of 10 TΩ for the resistance of a DNA molecule at length scales larger than 40 nm. It is concluded that DNA is insulating. This conclusion is based on an extensive set of experiments with variation of key parameters such as base-pair sequence [mixed sequence and homogeneous poly(dG)·poly(dC)], length between contacts (40 nm to 500 nm), substrate (SiO_2 and mica), electrode material (gold and platinum), and electrostatic doping fields. Discrepancies with other reports in the literature are discussed.[1]

[1]This chapter has been published in Applied Physics Letters:
A. J. Storm, S. J. T. van Noort, S. de Vries and C. Dekker *Insulating behavior for DNA molecules between nanoelectrodes at the 100 nm length scale.* Appl. Phys. Lett. **79**, 3881-3883 (2001).

6.1 Introduction

Recently, a number of contradicting findings were reported regarding the charge transport properties of DNA [30]. Experiments appeared to indicate metallic [10, 31, 32], semiconducting [33–35], and insulating [11, 36] electronic properties. These transport experiments were inspired by electron-transfer experiments where one attaches donor and acceptor groups at both ends of DNA molecules and characterizes their electronic coupling through the DNA. Such experiments by Barton [37] and others showed that electron transfer is possible in DNA over distances of several nanometers. Some direct transport experiments have suggested that transport is also possible over much larger length scales of the order of a micron [10, 31, 32, 35]. In this Letter, we report transport measurements on both individual DNA molecules as well as small DNA bundles (up to tens of molecules) that are connected on both sides to metallic electrodes. Our technique relies on well-defined electrodes with spacings in the range of 40 nm to 500 nm. Using state-of-the-art Atomic Force Microscope (AFM) imaging we report for the first time images of individual DNA molecules positioned between electrodes. We find no evidence for any electronic conductivity for DNA molecules with various lengths and base pair sequences. Based on a set of experiments with a number of different sample layouts, we come to the conclusion that DNA at the single-molecule scale is insulating at length scales larger than 40 nm.

6.2 Experiments and results

As an example of a typical result of our work, Fig. 6.1 shows a tapping-mode AFM height image of one of our devices with mixed-sequence double-strand DNA between gold electrodes spaced by 300 nm. On the SiO_2 in between the electrodes, individual DNA molecules are clearly discernable. Details on assembly of this device are given below. The apparent height of the DNA is about 0.5 nm, and the width is about 10 nm, limited by the AFM tip-radius. These values are typical for single DNA molecules [38]. From the height, width, and persistence length determined from the images, we conclude that indeed individual DNA molecules are connected between our electrodes. No conductance was found for this device. The bias

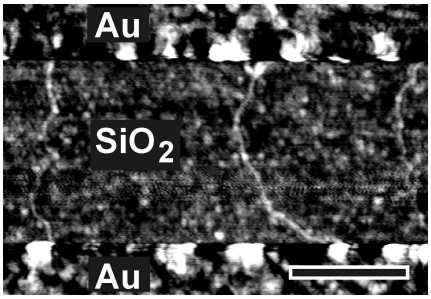

Figure 6.1: Tapping-mode AFM height image of three DNA molecules connected between two gold electrodes that are separated by 300 nm. Scale bar: 200 nm. The measured resistance of this device was higher than 10 TΩ.

voltage was slowly increased to 10 V and the observed currents remained below the noise level of about 1 pA. From this experiment we thus obtain a lower bound of 10 TΩ for the resistance of this device, where a total number of about 10 DNA molecules were connected in parallel between the electrodes.

The outcome of this experiment is in clear disagreement with a number of previously reported experiments. To investigate whether our result is due to the intrinsic electronic properties of DNA or due to external conditions, a series of experiments was conducted where a number of key parameters were varied, viz., the base-pair sequence of the DNA, the type of substrate, the distance between the electrodes, and the contact material. An attempt was also made to dope the DNA electrostatically with an external gate electrode.

The basic sample layout for all experiments discussed in this chapter is similar: DNA molecules are deposited from an aqueous buffer solution onto a substrate patterned with pairs of closely spaced thin metallic lines that are connected to larger pads which facilitate contact to the electrical equipment. The electrodes are fabricated using electron-beam lithography and subsequent lift-off. Noble metal (platinum and gold) films were used as electrode material. Metal thickness was about 15 nm, evaporated on top of a 3 nm titanium sticking layer. After lift-off, residues of the organic poly(methyl methacrylaat) double-layer resist were removed by immersion in fuming nitric acid. DNA molecules were deposited from a 20 mM HEPES buffer

solution (pH 6.5). DNA concentrations were in the range of 1 ng/μl to 250 ng/μl, and 5 mM of $MgCl_2$ was added to promote DNA adhesion to the surface. A droplet of about 3 μl is deposited on the substrate for about 20 seconds, after which the sample is rinsed with deionized water and dried in a flow of nitrogen gas. The presence of DNA molecules is confirmed by AFM imaging. Electrical transport measurements were performed at room temperature under ambient conditions.

The first set of experiments discussed here was performed on DNA with a mixed sequence immobilized on a silicon oxide substrate. Because DNA binds only weakly to the SiO_2 and is easily rinsed off, we used DNA modified with thiol (-SH) groups at both ends of the molecule. The sulfur atom of the thiol group will bind strongly to the platinum or gold of the electrodes, which chemically anchors the molecule to the metal at its terminal ends. Double-strand DNA with a $(CH_2)_6SH$ group at each 5' terminal phosphate was obtained by performing PCR (polymerase chain reaction) with λ-DNA as a template using thiolated primers, following the recipy of Hegner *et al.* [39] Dithiothreitol (DTT) was added to prevent oxidation of the thiols during PCR. Using this technique, DNA fragments of 900 and 4500 base pairs were obtained and purified, with lengths of 300 nm and 1.5 μm respectively. These fragments contain a mixed sequence of bases, and are representative for natural DNA. Figure 6.1 shows an AFM image of the 1.5 μm fragments positioned on Au electrodes spaced by 300 nm. Because the DNA is much longer than the distance between the electrodes, a considerable length of DNA overlaps with both electrodes which will facilitate a good electrical contact. As mentioned above, no electron transport was observed for this sample. The same absence of conductance was observed for a number of similar samples with electrode spacing in the range of 200 nm to 500 nm.

Considerable effort was put into the fabrication of smaller spaced electrodes, without losing the possibility to image in-between the electrodes using AFM[2]. Figure 6.2(a) shows DNA located across a gap of about 40 nm. In this experiment we deposited DNA from a 1 ng/μl solution of thiolated PCR fragments of 900 base pairs length. AFM inspection showed a small amount of DNA material between the elec-

[2]The small nanoelectrodes as reported by D. Porath [33] do not allow AFM imaging between the electrodes.

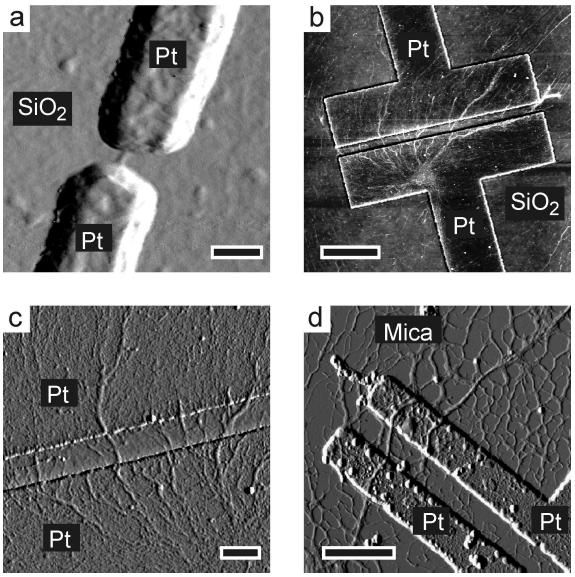

Figure 6.2: AFM images of DNA assembled in various devices. (a) Mixed-sequence DNA between platinum electrodes spaced by 40 nm. Scale bar: 50 nm. (b) Height image of poly(dG)·poly(dC) DNA bundles on platinum electrodes. Distance between electrodes is 200 nm, scale bar is 1 μm. (c) High magnification image of the device shown in (b). Several DNA bundles extend clearly over the two electrodes. Scale bar is 200 nm. (d) Poly(dG)·poly(dC) DNA bundles on platinum electrodes fabricated on a mica substrate. Scale bar is 500 nm. For all these devices, we observe an absence of conduction.

trodes. From the width and height of the DNA it is estimated that at most 5 DNA molecules are present in parallel between the electrodes. No charge transport was observed for bias voltages up to 10 V. From this experiment we again find a lower bound for the device resistance of 10 TΩ.

Experimental [40] and theoretical [34] studies on DNA charge transport suggest higher transport rates for poly(dG)·poly(dC) DNA as compared to mixed-sequence DNA. To investigate this issue experimentally, we assembled devices with poly(dG)·poly(dC) DNA molecules with an average length of several microns.[3] No thiol groups

[3]Material obtained from Amersham Pharmacia Biotech.

were present on this molecule. It was found that DNA is immobilized on the SiO_2 surface after rinsing and drying for relatively high DNA concentrations of about 100 ng/μl in buffer solutions of 20 mM HEPES and 5 mM $MgCl_2$. Reactive-ion etching before metal deposition was used to level the surface of the platinum electrodes to the same height as the SiO_2 substrate, in order to prevent kinks in the DNA and to minimize tip convolution effects. Figure 6.2(b) shows poly(dG)·poly(dC) molecules on electrodes spaced by 200 nm. Figure 6.2(c) shows a magnification of the image displayed in fig. 6.2(b). Due to the high concentration, not only single molecules are observed, but also thicker bundles of molecules, estimated to have at least 10 parallel strands of DNA. No conduction was found for these samples either. We estimate that in this experiment there are roughly 50 DNA molecules connected in parallel. Similar results were obtained on devices with a spacing of 100 nm.

Additionally we attempted to electrostatically dope the DNA with additional charge carriers in order to increase the conductance. This was done by applying a gate voltage to the silicon substrate with respect to one of the electrodes. No increase of conductance was found for gate voltages in the range of -50 V to +50 V. The thickness of the silicon oxide was 200 nm.

Finally we discuss the possible influence of the substrate. Both Kasumov et al. [10] and Cai et al. [34] report a finite DNA conductance in devices where the DNA was immobilized on mica substrates. Using a slightly modified fabrication recipe, we were able to fabricate patterned electrodes on mica substrates, with an electrode spacing of 200 nm. Figure 6.2(d) shows poly(dG)·poly(dC) molecules between platinum contacts on mica. DNA was deposited from a high-concentration buffer solution with approximately 250 ng/μl DNA. Under these conditions, DNA self-assembles into networks similar to those observed in the work of Cai *et al.* [34] Subsequent electrical transport experiments showed a high resistance of about 1 TΩ, a typical value that we also find for mica devices before DNA deposition. In a flow of dry nitrogen gas, this value was found to increase. We therefore attribute this background conduction to the thin water layer present on the hydrophilic mica [41].

6.3 Conclusions

We conclude that DNA is insulating at length scales larger than 40 nm, with a 10 TΩ lower bound for the resistance of a DNA molecule. Our experiments were performed using straightforward lithography, standard DNA buffer conditions, and high-resolution sample characterization using AFM imaging. The suggested formation of an electronic p-band [42] appears not to occur over length scales of 40 nm or larger, even for homogeneous poly(dG)·poly(dC) sequences. Most theoretical models assume that the charge transport rate through DNA decays exponentially with distance [7]. Experimental evidence for an exponential decay is reported by Cai *et al.* [34] Our findings are therefore not necessarily in disagreement with DNA charge transport experiments performed on the scale of a few nanometers, where relatively high transport rates have been reported [33, 37].

Our results are in agreement with results of De Pablo *et al.* [11] and Braun *et al.* [36], who also find the absence of electronic transport through DNA. Clear disagreement is found with the work of Kasumov *et al.* [10] and Fink *et al.* [32] who report a high conductivity of λ-DNA on the scale of 0.5 μm. For a single DNA molecule with a length of about 500 nm, they observe typical resistances of about 300 kΩ and 3 MΩ respectively, which is at least 6 orders of magnitude lower than observed in our experiments. In the experiments by Fink *et al.*, a small DNA bundle is freely suspended in vacuum, but Kasumov *et al.* used a layout similar to ours. Kasumov *et al.* used electrodes consisting of thin rhenium film covered with sputtered carbon on a mica substrate. We use platinum and gold contacts instead, but we do not see how this difference can lead to the dramatically different experimental results. Cai *et al.* [34] find a resistance of about 200 GΩ for bundles of poly(dG)·poly(dC) at a length scale of 200 nm. If we compare this value to our lower boundary of 1 TΩ for similar bundles of 200 nm length, there is only a slight discrepancy.

Our results clearly limit the use of bare DNA as a conducting molecular wire. The self-assembling properties of DNA, however, may be very useful for nanotechnology, for example as a scaffold to construct self-assembled electronics based on the technique of DNA metallization discussed by Braun *et al.* [36].

Acknowledgements

We thank E. Yildirim, H.W.Ch. Postma, K.A. Williams, B. Rousseeuw, A.K. Langen-Suurling, and R.N. Schouten for experimental assistance and discussions. This research was financially supported by the Dutch Foundation for Fundamental Research on Matter (FOM) and the European Community IST-FET project "DNA-based electronics".

Chapter 7

Electrochemistry at lithographically fabricated nanometer-scale electrodes

Abstract

The miniaturization of electrodes improves the capabilities of analytical cyclic voltammetry and various techniques have been reported to fabricate electrodes down to nanometer dimensions. We report a new technique to make electrodes in the 15 nm to 200 nm range in a controlled way using silicon nanofabrication. Electron microscopy has been used to address the size and geometry of the devices. We measured the diffusion-limited current with cyclic voltammetry and determine empirically its dependence on the electrode size. We find that our data cannot be understood with a simple planar-disk electrode model. Much better agreement is found with a more detailed calculation that takes our electrode geometry into account explicitly. This demonstrates that relying on a simplified electrode model can introduce large systematic errors in the electrode size as determined from the diffusion limited current.

7.1 Introduction

It is widely recognized that the miniaturization of electrodes extends the capabilities of cyclic voltammetry as an analytical technique. This stems ultimately from the higher diffusive particle flux that can be maintained at small electrodes, resulting in faster equilibration and increasing sensitivity to heterogeneous electrode kinetics. A wide array of techniques have now been reported that allow fabrication of electrodes with reported lateral dimensions of a few nanometers. A particularly successful approach, originally motivated by scanning electrochemical microscopy (SECM) applications, consists in selectively coating atomically sharp metal tips with an insulator such as wax [43], polyimide [44] or electrophoretic paint [45–47]. In addition to SECM, such electrodes have been used for example to study the role of supporting electrolyte at nanoelectrodes [47] and to evaluate heterogeneous rate constants [48].

Despite continuous improvement of the preparation methods, however, knowledge of, and control over the geometry of these electrodes remains very limited. Techniques based on coating with electrophoretic paint, for instance, rely on successive coats of insulator being applied, with little control over the structure of the insulator after each iteration. Since the precise waveform in cyclic voltammetry (from which kinetics information is extracted) is influenced by the shape of the electrode, incomplete knowledge of this geometry can introduce large systematic errors in the determination of rate constants.

Several techniques have been employed to deduce partial information about electrode geometry. For example, Fan, Kwak and Bard [49] analyzed the dependence of the diffusion-limited current as a function of the distance between an electrode and a nearby surface using a SECM apparatus. They showed that the data could best be fitted by assuming that the metal electrodes are recessed electrode in the surrounding insulator. More recently, Watkins *et al.* [48] independently determined both the real surface areas and the effective diffusion-limited radii for electrodes insulated with electrophoretic paint. They concluded that while the response of some electrodes is consistent with that expected for ideal shrouded hemispherical electrodes, many show significant departure from this simple assumption. Because of these significant variations between electrodes fabricated

using nominally identical processes, using such electrodes for precise quantitative analysis would require screening each electrode individually. This is not practical for routine work, especially since the characterization techniques are not necessarily compatible with further use of the electrode.

Here we present a method for the controlled fabrication of electrodes with dimensions between 15 nm and 200 nm using electron-beam lithography and associated techniques. The electrodes consist of a nanometer-scale opening in an insulating membrane that is blocked on one side with metal. The main advantages of this technique are that the size of the electrodes can be tuned controllably, that the shape of the electrodes is essentially identical for devices prepared using the same process, and that this shape can be determined with relatively high accuracy. In addition, the metal of the electrode is deposited in vacuum from a pure metal target and is never covered with an insulator, eliminating the risk of contamination.

We present voltammetric data for electrodes with a range of sizes, and show that both the size dependence and the precise shape of the voltammograms can be understood in terms of diffusion and Butler-Volmer electrode kinetics provided that the precise shape of the electrode is properly taken into account. This provides a direct illustration of how simplifying assumptions about geometry can introduce large errors in the analysis of steady-state voltammetry data.

7.2 Materials and methods

7.2.1 Electrode fabrication

The electrodes are fabricated using standard processes from semiconductor industry. In short, we etch pores in a silicon membranes using a process developed by Gribov *et al.* [14]. The silicon surface of the pore and the membrane are then oxidized. Finally, the electrode is formed by deposition of a noble metal layer. Below we describe the key steps in this fabrication process.

We start with commercially available Silicon-On-Insulator wafers[1] with a diameter of 100 mm. The wafer consists of a sandwich of a 525 μm thick handle wafer, a buried silicon-oxide layer of 400 nm

[1]Obtained from SOITEC, 38190 Bernin, France

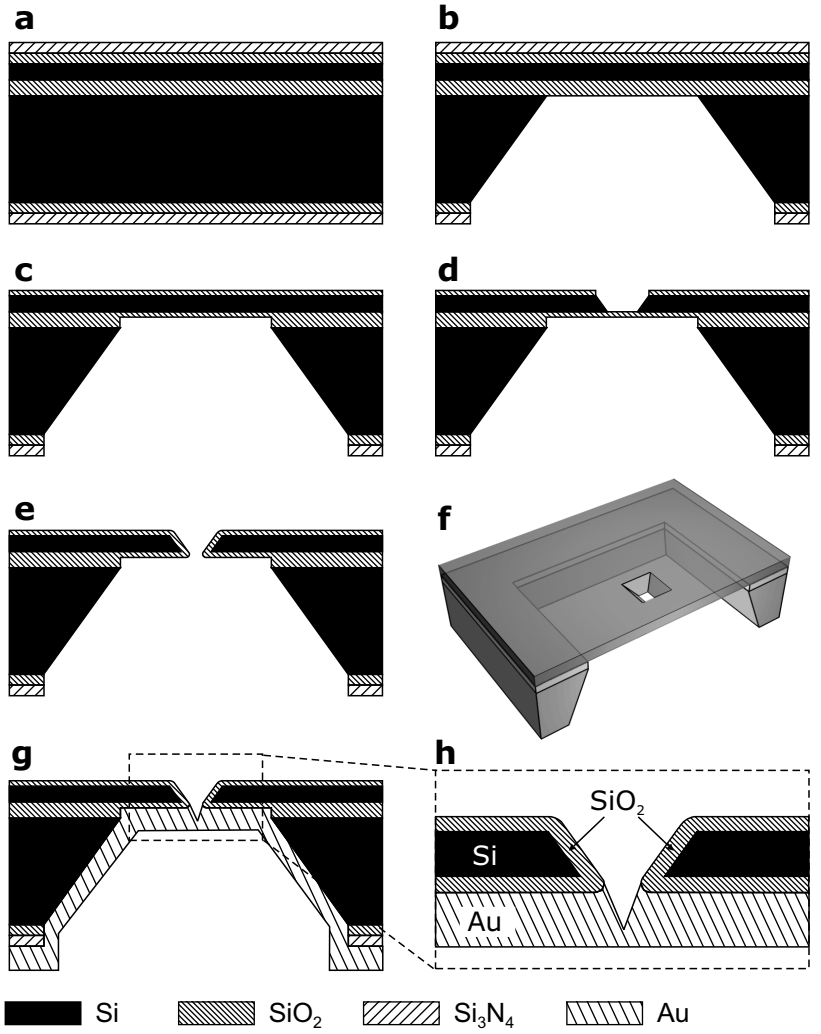

Figure 7.1: (a-e) Cross-sectional views of our electrodes at various stages of the fabrication process. See section 7.2.1 for a description. (f) Three dimensional, cross-sectional view of the structure at the stage depicted in panel e. (g) After evaporating gold from the bottom the electrode is formed at the aperture of the pore. Note that the silicon device is shown lighter for clarity. (h) Detail of the final structure shown in panel g.

and a silicon device layer of 340 nm thick. Both the handle wafer and the thin device layer are ⟨100⟩ silicon single crystals and are p-doped with a conductivity of 20-30 Ωcm. The wafer is covered on both sides with a 100 nm thick silicon oxide layer and subsequently a 100 nm Si_3N_4 layer, both using chemical vapour deposition (CVD). Figure 7.1a shows a cross-section of our wafer after this step. We then perform electron-beam lithography and subsequent CHF_3 plasma etching to open up squares of about 800 μm in the silicon nitride layer covering the handle wafer. We strip the residual resist and remove the silicon oxide in these squares with buffered hydrofluoric acid (BHF). Anisotropic wet KOH etching (300 gr/l, 80 °C) results in pyramid shaped holes through the handle wafer, as shown in Figure 7.1b. This is a standard microfabrication technique, based on strong differences in etch rates for the various silicon crystal directions [20]. This etching step slows down significantly at the buried oxide layer, and the wafer is removed from the KOH before this layer is consumed. A quick dip in hydrochloric acid before rinsing and drying prevents residues on the wafer. The silicon nitride layer covering the device layer is removed with a SF_6 plasma etch. Using BHF we etch the silicon oxide layers that cover the silicon membranes on both sides. The bare silicon membrane is then covered again with a 40 nm thick silicon oxide layer, resulting in the structure shown in Figure 7.1c. In a second electron-beam lithography step we pattern a single square of about 400 nm on each membrane. This pattern is transferred to the silicon oxide layer by CHF_3 plasma etching. We now etch through the silicon device layer in 2 minutes using again KOH (330 gr/l, 60°C), see Figure 7.1d for the result. Directly following this step we rinse in diluted hydrochloric acid and open up the pore by removing the silicon oxide using BHF. By thermal oxidation a layer of silicon oxide is grown on all silicon surfaces. The surface of the pore and the membrane is now covered with silicon oxide layer 15 nm to 40 nm thick, as shown in Figures 7.1e,f. The final size of the pores ranges from completely closed to about 200 nm, depending on the exact size of the lithographically-defined square.

These pores can easily be located and imaged using a scanning electron microscope (SEM, both a Philips XL30s-FEG and a Hitachi S900 microscope were used). From the electron micrograph we can determine the exact size. These microscopes are known to deposit

amorphous carbon-rich contamination on the specimen, which is removed by oxygen-plasma cleaning. To obtain electrodes from our pore structure we evaporate a 5 nm thick chromium layer (purity 99,998% obtained from Kurt J. Lesker, Clairton, PA, USA) followed by a gold layer (purity 99,999% obtained from the same supplier) of at least 300 nm. Both layers were deposited using a system from AJA international (North Scituate, MA, USA) without breaking vacuum to prevent oxidation of the chromium. The chromium is necessary for a proper sticking of our thick gold layer to the silicon oxide. The gold layer was chosen to be thick enough to close our pores completely to obtain our well-defined, sub-micron electrodes. In the experiments the only contact between the metal and the solution is at the nanometer-sized gold electrode at the bottom of the pyramid-shaped pore. The silicon oxide prevents electrochemical reactions with the silicon membrane.

7.2.2 Chemicals

The measurements were carried out in aqueous solution with 1 mM ferrocenylmethyltrimethylammonium ($FcTMA^+$) as redox-active species, 1mM PF_6^- as the counter-ion, and 1 M KCl as supporting electrolyte. The ferrocene was purchased in the form of ferrocenylmethyltrimethylammonium iodide crystals from Lancaster (Eastgate, White Lund, Morecambe, England). Because the iodide counter-ion reacts with gold, it was replaced with PF_6^- using the following procedure. First 25mg of ferrocene-TMA^+-iodide was dissolved in 2 ml Milli-Q water and the result was mixed with 100 μl 5M ammonium hexafluorophosphate, NH_4PF_6 (Aldrich, Milwakee, WI, USA). PF_6^- forms a poorly soluble salt with ferrocene-TMA^+ which precipitates, after which it can be separated by centrifugation from the solution now containing predominantly NH_4^+, PF_6^- and I^-. The pellet was then re-dissolved in Milli-Q water. These steps were repeated 2-3 times with a smaller concentration of NH_4PF_6 and once with water. This resulted in a pellet that was nearly free of iodide (less than 0,1%). This pellet was dissolved in 60ml Milli-Q water to yield a 1mM ferrocene-TMA^+ solution.

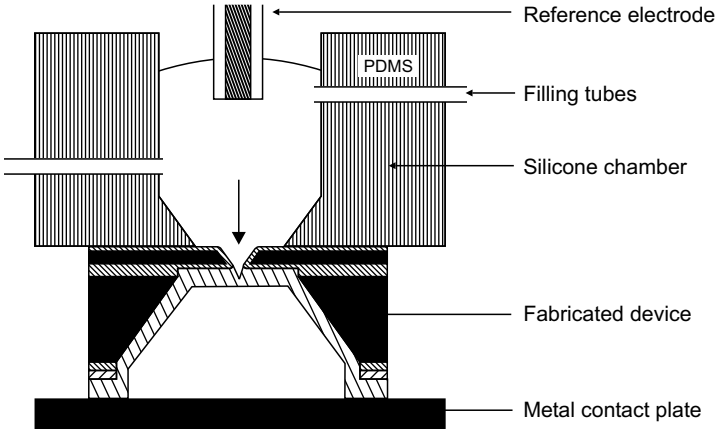

Figure 7.2: Schematic diagram of the measurement apparatus (not to scale). The vertical arrow indicates the point where liquid makes contact with the nanoelectrode.

7.2.3 Electrochemical apparatus

As illustrated in Figure 7.2, a small (about 200 μl) liquid cell was formed above each electrode by pressing a cylindrical chamber made of silicone elastometer (Sylgard 184, Dow Corning) against the surface of the silicon wafer. The cell had a circular opening at the top (diameter 4 mm) for positioning a reference electrode and a smaller (diameter 100-300 μm) circular opening at the bottom. The latter reduced the contact area between the liquid and the silicon oxide surface and thus the capacitance between the solution and the underlying silicon. A stereo microscope (Olympus) and a three-axis manipulator (Newport) were used to align the bottom cell opening with the electrode. Two teflon tubes connected to holes in the walls of the liquid cell allowed easy substitution of the working solution. All cyclic voltammetry data were recorded in a two-electrode configuration using a Keithley 6430 sub-femtoampere sourcemeter with remote preamplifier. The instrument was controlled via the built-in GPIB interface using in-house Labview software. All electrochemical potentials were measured with respect to a Ag/AgCl reference electrode (model RE-6, BAS). The liquid cell and preamplifier were placed in a home-built Faraday cage.

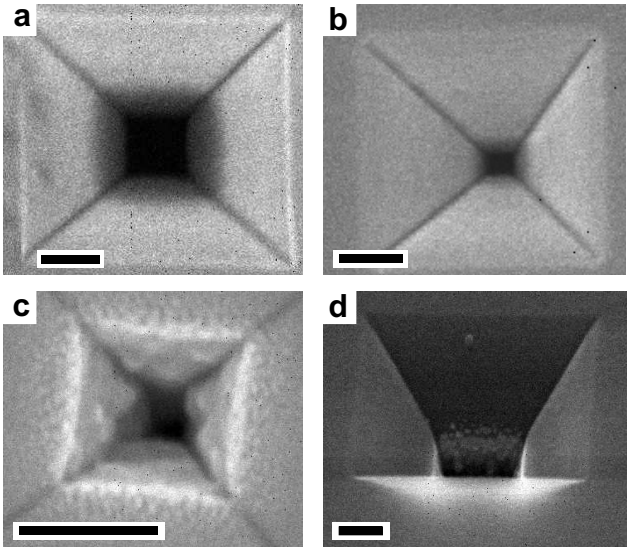

Figure 7.3: (a-b) Scanning electron microscope images of two pores prior to metal deposition. (c-d) Images of two completed electrodes viewed at normal incidence to the surface (c) and at a 45° angle (d). In each image the scale bar represents 100 nm.

7.3 Results and discussion

7.3.1 Scanning electron microscopy

Figures 7.3a,b show scanning electron microscope (SEM) images of pores in silicon/silicon oxide membranes before metal deposition. The inverted pyramid shape of these pits is due to the KOH anisotropic etch by which the pore was formed, with the four faces corresponding to the (111) planes of the crystalline silicon. From such images the actual dimension of each individual device was determined before metal deposition. This procedure has the important advantage that the metal surface remains free of the carbon contamination that would result if the electrode was imaged after metallization.

Figures 7.3c,d show SEM micrographs of two devices after metal deposition. The metal surface accessible through the pore in the insulating membrane has the same inverted pyramid shape as the pore itself. The gold layer exhibits a rough, granular structure with bumps

of about 10 nm in size; such roughness is typical for gold deposited at room temperature. In addition, small islands of metal form near the edge of the metal electrode. These appear to be electrically disconnected from the electrode, an observation that is supported by the voltammetry measurements discussed below.

7.3.2 Steady-state cyclic voltammetry

Typical voltammograms are shown in Figures 7.4a and b for two electrodes. At a potential of 0.45 V a reduction wave is observed, as expected. At potentials below this wave, a linear dependence of the current i on the electrode potential E is also observed. This component of the current is also observed in measurements on silicon membranes where neither pore nor electrode has been fabricated, and is attributed to a leakage current through the silicon oxide layer. This linear component has been subtracted from the data before further analysis was conducted, as illustrated in Figure 7.4b.

In order to permit further analysis, we fitted the measured voltammograms to the functional form corresponding to diffusive mass transport coupled to Butler-Volmer heterogeneous electrode kinetics [50],

$$i(E) = \frac{i_{\text{lim}}}{1 + e^{-nF(E-E^{0\prime})/RT} + \lambda^{-1} e^{nF(\alpha-1)(E-E^{0\prime})/RT}}. \qquad (7.3.1)$$

Here E is the applied electrode potential, $E^{0\prime}$ is the formal reaction potential, F is the Faraday constant, $n = 1$ is the number of electrons transferred per molecule, α is the transfer coefficient, i_{lim} is the diffusion-limited steady-state current, and λ is the so-called dimensionless rate constant.

Eq. 7.3.1 is applicable to any electrode geometry provided that the concentration can be considered constant over the electrode surface [51]. Great care must however be taken in the quantitative interpretation of the parameters λ and i_{lim} when dealing with non-hemispherical electrodes since their values are influenced by both the size and, more subtly, the shape of the device. Because the smallest electrodes reported here have lateral dimensions greater than 10 nm and the fact that ferrocene-TMA^+ has rapid kinetics, however, we expect $\lambda^{-1} \ll 1$ and kinetic effects are not expected to severely affect the shape of the measured voltammograms. We therefore concentrate on the interpretation of the limiting current i_{lim}.

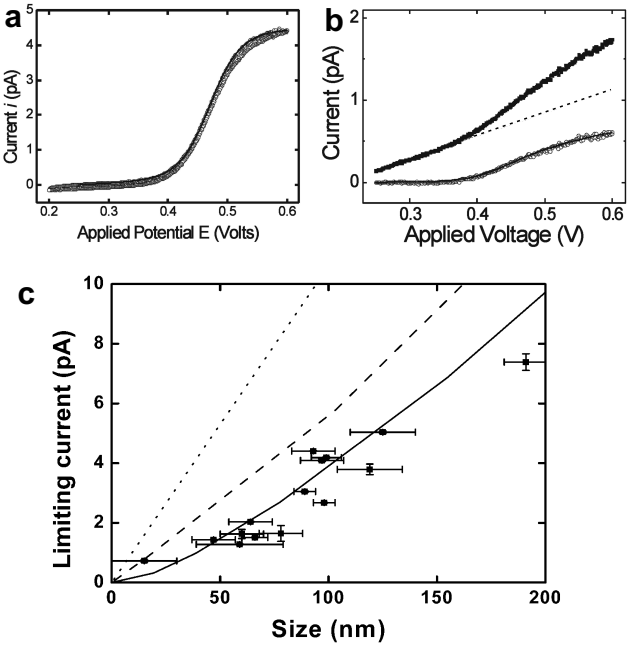

Figure 7.4: (a) Cyclic voltammogram for an electrode with lateral size $l = 100$ nm. A positive and a negative sweep are shown. The solid line represents a fit of the positive sweep to Eq. 7.3.1. (b) Solid symbols: same for an electrode with $l = 15$ nm. For clarity only the positive sweep is shown. Part of the current is due to the parasitic conductance of the silicon oxide membrane, and is subtracted (open symbols) to obtain the response of the electrode. The solid line is a fit to Eq. 7.3.1. (c) Limiting current $i_{\rm lim}$ versus measured electrode size l for 15 electrodes. The values of $r_{\rm eff}$ corresponding to $i_{\rm lim}$ are also shown. The lines represent calculations of the limiting current based on the diffusion equation; see text for details (dotted line, $h_o = h' = 0$ nm; dashed line, $h_o = 310$ nm, $h' = 0$ nm; solid line, $h_o = 310$ nm, $h' = 40$ nm).

For a hemispherical ultramicroelectrode of radius r, the limiting current i_{lim} is simply given by $i_{\text{lim}} = 2\pi nC^*FDr$, where C^* is the bulk concentration and D is the diffusion constant. For electrodes of arbitrary shape, an effective electrode radius r_{eff} can be defined as

$$r_{\text{eff}} = \frac{i_{\text{lim}}}{2\pi nC^*FD}. \tag{7.3.2}$$

For most common non-hemispherical geometries, for example planar or recessed electrodes, the value of r_{eff} is smaller than half the lateral size of the electrode. This simply reflects the fact that such electrodes are less accessible to solution than hemispherical electrodes of the same size.

Figure 7.4c shows the measured limiting current i_{lim} as well as the corresponding r_{eff} versus the measured side length l of each device for 15 different devices. i_{lim} decreases monotonically with decreasing l, as expected. Contrary to the simplest expectations, however, i_{lim} is not simply proportional to l, instead decreasing more rapidly with decreasing l.

7.3.3 Theoretical determination of the limiting current

At sufficiently high overpotential, the redox current is limited only by mass transport. In this section we show that the unconventional dependence of the limiting current i_{lim} on electrode size l observed in Figure 7.4c can indeed be fully understood by considering solutions to the diffusion equation,

$$\frac{\partial c(\vec{r})}{\partial t} = D\nabla^2 c(\vec{r}), \tag{7.3.3}$$

where D and $c(\vec{r})$ are the diffusion constant and the concentration of Fc-TMA$^+$, respectively. The corresponding electrical current density is $nFD\nabla c(\vec{r})$, where F is the Faraday constant and $n = 1$ is the number of electrons transferred per molecule. Because analytical solutions to Eq. 7.3.3 only exist for relatively simple geometries such as spheroidal electrodes, we have obtained numerical finite-element solutions. We first present these numerical results, and then give a simple analytical analysis that provides a straightforward interpretation of the key features of the exact calculations.

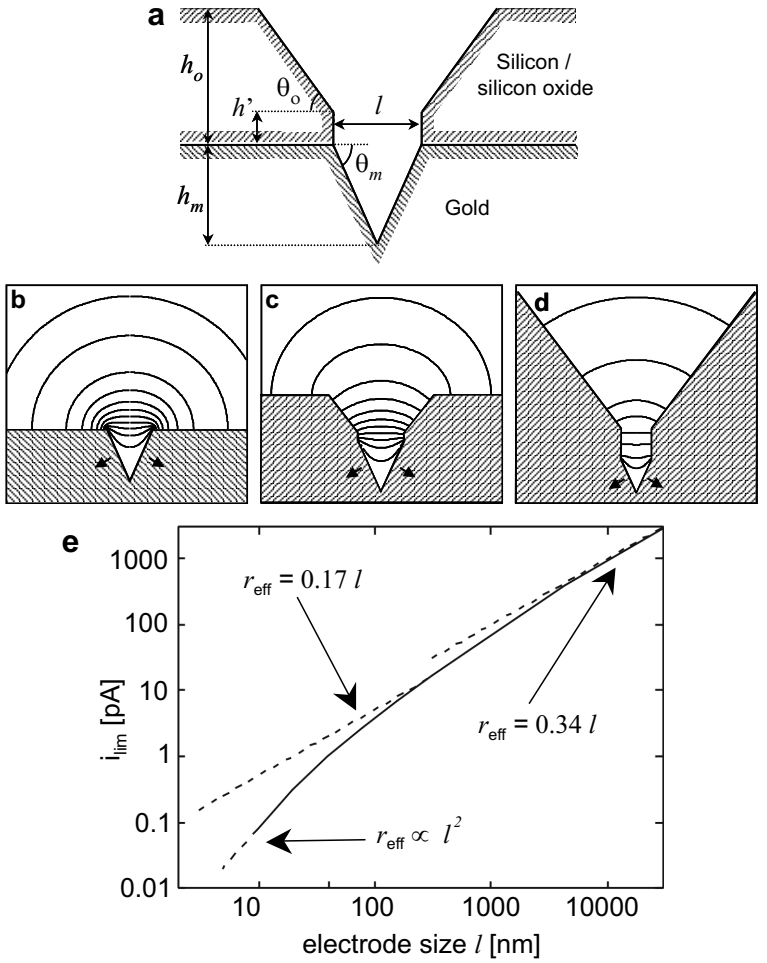

Figure 7.5: (a) Geometry model used for the simulations. The figure is a two-dimensional cut through the center of the structure; the calculation is performed in three dimensions. (b) Contour plot of $c(\vec{r})/C^*$. The data are plotted on the same two-dimensional plane as in a, and correspond to the cases $h_o/l = h'/l = 0$. The contour lines correspond to $c(\vec{r})/C^* = 0.02$, 0.1, 0.2, 0.3, 0.4, 0.5, 0.6, 0.7, 0.8, 0.9 and 0.95. (c) Same as b for the case $l/h_o = 8$, $h'/h_o = 0.13$. (d) Same as b for the case $l/h_o = 1$, $h'/h_o = 0.13$. The contour lines correspond to $c(\vec{r})/C^* = 0.02$, 0.1, 0.3, 0.5, 0.7, 0.8, 0.9 and 0.95. (e) Calculated diffusion-limited current $i_{\rm lim}$ versus electrode size l in geometry shown in panel (d). There are three main regimes; see text for details.

The three-dimensional geometry model of our devices that was used for calculations is shown in Figure 7.5a. The geometry parameters of this model and their numerical values are the thickness of the insulating membrane above the electrode h_o (310 nm in our experimental devices), the lateral size of the pore l (15-200 nm), the angles θ_o (54.7° for the (111) planes of silicon) and θ_m (66° as estimated from SEM images at different angles), and the thickness h' of a region near the electrode where the silicon oxide walls rise vertically. The latter is due to the finite thickness of the silicon oxide around the pore. While the exact shape and extent of this region is difficult to determine exactly from SEM images, a good estimate is vertical walls with a height equal to the thickness of the silicon oxide, $h' = 40$ nm. The height of the metal region, h_m, is not an independent parameter: it is set by the values of l and θ_m. In this geometric model the roughness of the silicon oxide and of the gold (a few nm) as well as the rounding of sharp edges have been ignored.

Note that the geometry of each device is not independent of its lateral size l. If, for example, the lateral size of the electrode l is halved, then h_m is also halved. On the other hand, the values of h_o and h' remain constant since they are fixed by the thickness of the membrane. The ratios h_o/l and h'/l are thus doubled. As we argue below, this change in geometry is at the origin of the nonlinear dependence of r_{eff} on l in Figure 7.4c.

The numerical calculations were performed using Femlab (Comsol AB, Stockholm). Steady-state solutions to Eq. 7.3.2 were obtained over a finite three-dimensional volume with a hemispherical outer boundary. This boundary was sufficiently far from the electrode that the diffusion profile was to a very good approximation spherically symmetric at the boundary. The numerical solution inside the finite volume could thus be matched at the outer boundary to the analytical solution for spherical diffusion in an infinite volume. The solutions thus correspond to the steady-state current. The simulations use $FDC^* = 50$ pA/μm. This value was determined from a measurement of the steady-state current at a standard 10 μm diameter disk electrode and using the expression $i = 4FDC^*r$, where r is the radius of the electrode.

The computed value of the limiting current versus electrode size l are shown in Figure 7.4c together with the experimental data.

The computed values of the limiting current are in agreement with the data within experimental error. For comparison, Figure 7.4c also shows calculations for simpler geometries than those of Figure 7.5a, namely, the cases where the insulating membrane is neglected ($h_m = 0$ nm) and where the membrane has the normal thickness but the constriction near the membrane is neglected ($h_m = 310$ nm, $h_m = 0$ nm). The calculated limiting currents for these geometries do not describe the experimental observations. In particular, they fail to take into account the suppression of the limiting current for the smallest electrodes.

It is clear from these data that, contrary to disk or spherical electrodes, the limiting current is not simply proportional to the lateral dimension l of the electrode. The origin of the suppression of the current for small electrodes is easy to understand qualitatively. For large electrodes ($l \gg h_m$), the thickness of the membrane is negligible. The diffusion profile (shown in Figure 7.5b) then effectively corresponds to spherical diffusion with a correction due to the fact that the electrode is not hemispherical. In this regime the limiting current is simply proportional to l, and the numerical calculations indicate that $r_{\text{eff}} = 0.34l$. When l becomes comparable to h_m, however, the concentration gradient in the oxide region becomes large enough that a significant fraction of the total change in concentration between bulk and the electrode surface occurs across the thickness of the membrane (plotted in Figure 7.5c). The total current is therefore suppressed. This suppression becomes increasingly pronounced as the ratio l/h_m decreases, until the regime $l/h_m \ll 1$ is reached. In the latter case most of the concentration drop between bulk and the electrode surface occurs in the inverted pyramid hole in the silicon. Diffusion becomes effectively spherical again, albeit with a reduced solid angle corresponding to that of the inverted pyramid. In this regime, we thus again have $I_{\text{lim}} \propto l$, but with a reduced proportionality constant $r_{\text{eff}}/l = 0.17$. This regime is not fully developed in our devices because an additional suppression of the current occurs when l becomes comparable to the last remaining length scale in the problem, h_l. The narrow channel near the electrode is then the dominant barrier to diffusion. There is once again a gradual suppression of the current with decreasing l, with the exception that the ration r_{eff}/l does not become constant again in the limit $l \ll h_l$. This is because

diffusion in the h_l channel is linear instead of spherical. Therefore $i_{\mathrm{lim}} \propto l^2$ in this regime. This trend is clearly visible in the theoretical plot of Figure 7.5e.

7.4 Conclusions

Our results directly demonstrate that metal electrodes with lateral dimensions below 100 nm can be fabricated using lithography techniques, and that the performance of these electrodes for voltammetry measurements can match that of electrodes made with more conventional techniques. One advantage of our approach is that the metal layer, deposited from a pure target under high vacuum conditions, is never exposed to an insulating layer during the fabrication process, and therefore remains free of contaminants. More importantly, the fabrication approach provides detailed knowledge of the geometry of the devices. As we have illustrated, lack of such knowledge can introduce systematic errors in the interpretation of voltammetry data, in particular in the evaluation of rate constants from wave-shape analysis. Lithographically fabricated electrodes thus provide a powerful tool alongside more conventional types of nanoelectrodes for use in high-precision, quantitative analysis of voltammetric data.

Several improvements to the devices described here can be envisaged. First, their geometry could be modified so that the metal electrode presents a convex or flat surface to the solution, facilitating diffusion. This can probably be achieved by careful annealing or by filling the pore with a sacrificial material before metal deposition. Second, the thickness of the silicon oxide away from the pore could be increased so as to reduce the parasitic capacitance and conductance associated with this layer. Third, the lateral size of the electrodes could be decreased further. As this is determined by the size of the pore in the silicon oxide membrane, and a technique for controllably fabricating such pores with a 2 nm diameter has recently been reported [25] it is likely that electrodes with a diameter of a few nanometers can be fabricated in the future using this process. Such nanoelectrodes with a well-controlled geometry will pave the way for accurate measurements of heterogeneous rate constants.

Acknowledgements

The research presented in this chapter was done in collaboration with Dennis van den Broek, Serge Lemay and Dirk Heering. This research was funded by the 'Stichting voor Fundamenteel Onderzoek der Materie (FOM)', which is financially supported by the 'Nederlandse Organisatie voor Wetenschappelijk Onderzoek (NWO)'.

Bibliography

[1] B. Alberts et al., *Molecular Biology of the Cell.*, Garland Publishing, New York, 1994.

[2] J. D. Watson and F. H. C. Crick, Nature **171**, 737 (1953).

[3] S. Padmanabhan, B. Richey, C. F. Anderson, and M. T. Record, Jr., Biochemistry **27**, 4367 (1988).

[4] G. Ravishanker et al., Rev. Comp. Chem. **11**, 317 (1997).

[5] J. J. Kasianowicz, E. Brandin, D. Branton, and D. W. Deamer, Proc. Natl. Acad. Sci. U. S. A. **93**, 13770 (1996).

[6] M. Akeson, D. Branton, J. J. Kasianowicz, E. Brandin, and D. W. Deamer, Biophys. J. **77**, 3227 (1999).

[7] J. Jortner, M. Bixon, T. Langenbacher, and M. E. Michel-Beyerle, Proc. Natl. Acad. Sci. U. S. A. **95**, 12759 (1998).

[8] J. Chen and N. C. Seeman, Nature **350**, 631 (1991).

[9] M. R. Arkin et al., Science **273**, 475 (1996).

[10] A. Y. Kasumov et al., Science **291**, 280 (2001).

[11] P. J. de Pablo et al., Phys. Rev. Lett. **85**, 4992 (2000).

[12] S. Howorka, S. Cheley, and H. Bayley, Nat. Biotechnol. **19**, 636 (2001).

[13] J. L. Li et al., Nature **412**, 166 (2001).

[14] N. N. Gribov, S. J. C. H. Theeuwen, J. Caro, and S. Radelaar, Microelectron. Eng. **35**, 317 (1997).

[15] G. S. Chen, C. B. Boothroyd, and C. J. Humphreys, Philos. Mag. A **78**, 491 (1998).

[16] G. S. Chen, C. B. Boothroyd, and C. J. Humphreys, Appl. Phys. Lett. **62**, 1949 (1993).

[17] P. M. Ajayan and S. Iijima, Phil. Mag. Lett. **65**, 43 (1992).

[18] G. I. Taylor and D. H. Michael, J. Fluid. Mech. **58**, 625 (1973).

[19] M. Lanxner, C. L. Bauer, and R. Scholz, Thin Solid Films **150**, 323 (1987).

[20] P. Rai-Choudhury (Ed.), *Handbook of Microlithography, Micromachining and Microfabrication*, SPIE Optical Engineering Press, Bellingham, WA, 1997.

[21] J. L. Li, M. Gershow, D. Stein, E. Brandin, and J. A. Golovchenko, Nature Mat. **2**, 611 (2003).

[22] A. Meller, L. Nivon, E. Brandin, J. Golovchenko, and D. Branton, Proc. Natl. Acad. Sci. U. S. A. **97**, 1079 (2000).

[23] R. W. DeBlois and C. P. Bean, Rev. Sci. Instrum. **41**, 909 (1970).

[24] A. Meller, L. Nivon, and D. Branton, Phys. Rev. Lett. **86**, 3435 (2001).

[25] A. J. Storm, J. H. Chen, X. S. Ling, H. W. Zandbergen, and C. Dekker, Nature Mat. **2**, 537 (2003).

[26] M. Doi and S. F. Edwards, *The Theory of Polymer Dynamics.*, Clarendon Press, Oxford, 1986.

[27] J. C. le Guillou and J. Zinn-Justin, Phys. Rev. Lett **39**, 95 (1977).

[28] Y. Kantor and M. Kardar, preprint, cond-mat/0310521 (2003).

[29] D. K. Lubensky and D. R. Nelson, Biophys. J. **77**, 1824 (1999).

[30] C. Dekker and M. A. Ratner, Physics World **14**, 29 (2001).

[31] Y. Okahata, T. Kobayashi, K. Tanaka, and M. Shimomura, J. Am. Chem. Soc. **120**, 6165 (1998).

[32] H. W. Fink and C. Schönenberger, Nature **398**, 407 (1999).

[33] D. Porath, A. Bezryadin, S. de Vries, and C. Dekker, Nature **403**, 635 (2000).

[34] L. T. Cai, H. Tabata, and T. Kawai, Appl. Phys. Lett. **77**, 3105 (2000).

[35] A. Rakitin et al., Phys. Rev. Lett. **86**, 3670 (2001).

[36] E. Braun, Y. Eichen, U. Sivan, and G. Ben-Yoseph, Nature **391**, 775 (1998).

[37] S. O. Kelley and J. K. Barton, Science **283**, 375 (1999).

[38] S. J. T. van Noort, K. O. van der Werf, B. G. de Grooth, N. F. van Hulst, and J. Greve, Ultramicroscopy **69**, 117 (1997).

[39] M. Hegner, P. Wagner, and G. Semenza, FEBS Lett. **336**, 452 (1993).

[40] M. Bixon et al., Proc. Natl. Acad. Sci U. S. A. **96**, 11713 (1993).

[41] R. Guckenberger et al., Science **266**, 1538 (1994).

[42] D. D. Eley and D. I. Spivey, Trans. Faraday Soc. **58**, 411 (1962).

[43] L. A. Nagahara, T. Thundat, and S. M. Lindsay, Rev. Sci. Instrum. **60**, 3128 (1989).

[44] P. Sun, Z. Zhang, J. Guo, and Y. Shao, Anal. Chem. **73**, 5346 (2001).

[45] C. J. Slevin, N. J. Gray, J. V. Macpherson, M. A. Webb, and P. R. Unwin, Electrochem. Commun. **1**, 282 (1999).

[46] J. L. Conyers, Jr. and H. S. White, Anal. Chem. **72**, 4441 (2000).

[47] S. Chen and A. Kucernak, J. Phys. Chem. B **106**, 9396 (2002).

[48] J. J. Watkins et al., Anal. Chem. **75**, 3962 (2003).

[49] F. R. F. Fan, J. Kwak, and A. J. Bard, J. Am. Chem. Soc. **118**, 9669 (1996).

[50] C. G. Zoski, *Modern Techniques in Electroanalysis.*, P. Vanyset (Ed.); Wiley, New York, 1996.

[51] K. B. Oldham, J. Electroanal. Chem. **323**, 53 (1992).

Summary

Nanotechnology can be defined as the development and use of devices with dimensions on the nanometer level. In this thesis the physical properties of single molecules are addressed using existing and newly developed fabrication techniques for silicon-based devices. The ability to fabricate devices with dimensions on the scale of molecules allows us to probe the properties of individual molecules. This thesis covers three research subjects.

Firstly, we address the polymer dynamics of DNA threading through a small pore. Such nanopores have proven to be an exciting new class of sensors for the detection and analysis of biopolymers such as DNA. Protein-based nanopores in a lipid membrane have been used extensively for translocation experiments of single strand DNA and RNA. In contrast we use solid-state nanopores for our experiments, that allow single molecule detection of double-strand DNA, which is too big to fit through the protein-based pores.

In chapter 2 we report a new technique for fabricating silicon oxide nanopores with single-nanometer precision and direct visual feedback. First, a pore with a size between 20 nm and 50 nm is etched in a free-standing silicon membrane. The surfaces of the membrane and pore are then thermally oxidized to grow a silicon oxide layer of about 40 nm. Surprisingly, the size of the pore can now be reduced in a transmission electron microscope, with an electron beam of sufficient energy. We conclude that the silicon oxide is fluidized by the electron beam and deforms due to its surface tension. The process takes place during imaging with the microscope and can be stopped when the desired size has been reached by blanking the beam.

A further study of this remarkable effect is presented in chapter

3. The effect of an electron beam on various silicon oxide nanostructures is studied and we find that all observations are in good agreement with the proposed model of surface-tension driven mass transport. In-situ studies of the composition of the specimen before and after modification also confirm our hypothesis that the silicon oxide deforms upon radiation. A TEM closed nanopore contains silicon oxide at the location where initially the pore was situated. We find no evidence for carbon contamination during our experiments.

Pores fabricated with this new technique are used for double-strand DNA translocation experiments, as reported and discussed in chapter 4. The pore separates two macroscopic reservoirs filled with buffer solution. A potential difference is applied across the two reservoirs and the ionic current that flows through the pore is measured using a high-bandwidth current amplifier. After addition of double-strand DNA to the reservoir kept at a negative potential, short depressions in the ionic current are observed. Such signals are interpreted as the passage of individual DNA molecules through the pore. The negatively charged molecules are forced through a pore by the electric force. The polymer inside the pore displaces some of the conducting electrolyte solution and this causes a reduction of the ionic conductivity of the pore during passage.

We observe various types of translocation signals, which we interpret as translocation of molecules that are folded in various ways. Such events can occur because the pore is about 10 nm and thus the double-strand DNA with a diameter of about 2 nm can pass the pore in a folded state. Additionally we demonstrate that a nanopore can be used to determine the composition of a mixture of DNA fragments with various sizes. The duration of translocation was determined for DNA fragments in the range from 2000 base pairs to 48000 base pairs. We find that the dwell time τ scales with the length L as $\tau \sim L^{\alpha}$, with a value of 1.26 ± 0.07 for the exponent α. The average velocity of the polymer decreases from about 20 mm/s for 2000 bp to about 8 mm/s for 48000 bp.

In chapter 5 we discuss a new theoretical model for polymer translocation. We show that DNA translocation through our solid-state nanopores is fast compared to polymer relaxation times, and as a consequence the long part of the polymer outside the pore has to be taken into account explicitly. The model is based on a force

balance between the electrostatic driving force and the viscous drag on the polymer. We indeed find a power-law scaling of the translocation time versus the length with an exponent of 1.18, which is in good agreement with our data.

A second focus of this thesis concerns electrical transport properties of individual DNA molecules in the dry state. Various experimental groups have addressed this issue, with results ranging from insulating to almost metallic behavior. We made a comprehensive study of devices with DNA molecules deposited on nanofabricated electrodes spaced by 40 nm to 500 nm. The presence of DNA molecules is confirmed with atomic force microscopy. We observe the absence of any electrical conduction in these devices. We varied a number of parameters such as base-pair sequence (mixed sequence and homogeneous poly(dG)·poly(dC)), length between contacts (40 to 500 nm), substrate (silicon oxide and mica), electrode material (gold and platinum) and electrostatic doping fields. We conclude that DNA is insulating on this scale, which severely limits the application of bare DNA for molecular electronics.

The third subject is discussed in chapter 7. It deals with electrochemistry on nanometer-scale electrodes. These nanoelectrodes were fabricated by deposition of gold on to silicon-oxide-nanopore devices. Pores between 15 nm and 200 nm were closed completely by the metal. A total of 15 devices was electrochemically characterized. We find that the diffusion-limited electrochemical current scales nonlinearly with the lateral electrode size. This result is in disagreement with the planar disk-electrode model, which is often used for nanoscale electrodes. Good agreement however is found with calculations of the diffusion-limited current that take our particular electrode layout into account. Parameters in this model are measured from electron micrographs of our devices. Our results show that the precise geometry of electrodes has a large effect on the electrochemistry, and that lack of such knowledge can introduce significant systematic errors. Estimating the size of nanoelectrodes from the diffusion limited current alone, which is common practice, is thus not reliable. We conclude that lithographically fabricated electrodes are a powerful tool for use in high-precision, quantitative voltammetry.

Arnold J. Storm
Delft, March 2004

Samenvatting

Nanotechnologie betreft de ontwikkeling en het gebruik van strukturen op nanometer-schaal. In dit proefschrift hanteren we dergelijke technieken voor het bepalen van de fysische eigenschappen van individuele moleculen. Om hiervoor instrumenten met de vereiste precisie te fabriceren, hebben we niet alleen gebruik gemaakt van bestaande technieken, maar ook nieuwe technieken ontwikkeld. In dit proefschrift komen drie onderwerpen aan de orde: het gedrag van DNA-moleculen die door een kleine opening worden getrokken, de elektrische geleiding van individuele DNA-moleculen en tot slot de karakterisering van elektroden op nanometer-schaal voor elektrochemische toepassingen.

Recent is ontdekt dat openingen op nanometer-schaal gebruikt kunnen worden voor de detectie en analyse van bio-polymeren, zoals bijvoorbeeld DNA. Voor dit soort experimenten zijn tot op heden vooral gaten gebruikt die verkregen zijn door het eiwitcomplex α-hemolysin te assembleren in een lipidenmembraan. De experimenten beschreven in dit proefschrift daarentegen zijn gedaan met openingen gemaakt in siliciumoxide. Dit heeft als voordeel dat we de grootte zelf kunnen kiezen. Dergelijke gaten gebruiken we voor de detectie van individuele dubbelstrengs DNA-moleculen, die te dik zijn voor detectie met behulp van gaten gevormd uit proteïnen.

In hoofdstuk 2 beschrijven we een nieuw ontwikkelde techniek voor de fabricage van gaten in siliciumoxide met een precisie van één nanometer. Om te beginnen etsten we een gat tussen de 20 en 50 nanometer in een vrijstaand silicium membraan. Op het oppervlak van het geperforeerde membraan lieten we vervolgens een laag siliciumoxide groeien van ongeveer 40 nanometer dik. Tijdens het af-

beelden van deze gaten met een elektronenmicroscoop zagen we een opmerkelijk verschijnsel: de diameter van de gaten nam af tijdens het belichten met de elektronenbundel. Op basis van verscheidene experimenten aan dit effect concluderen we dat de elektronenbundel het siliciumoxide vloeibaar maakt, waarna het vervormt door de oppervlaktespanning. Het proces vindt plaats tijdens het afbeelden en kan direct worden gestopt als de gewenste grootte is bereikt door de elektronenbundel uit te zetten.

In hoofdstuk 3 bestuderen we dit verschijnsel in meer detail. Uit experimenten op nanostructuren met verschillende vormen blijkt dat het effect van de bundel in overeenstemming is met het in hoofdstuk 2 gepresenteerde model. Ook metingen aan de samenstelling van het materiaal rondom de gaten voor en na de modificatie laten hierin geen significante veranderingen zien. Hieruit concluderen we dat het preparaat inderdaad vervormt. Daarnaast hebben we zeer lokaal de samenstelling bepaald van het 'nieuwe' materiaal dat een verkleind gat heeft opgevuld. Hier detecteerden we duidelijk siliciumoxide. Dit resultaat sluit de depositie uit van koolstofrijke verontreiniging, een bekend verschijnsel in de elektronenmicroscopie, als een mechanisme dat het krimpen van gaten zou kunnen verklaren.

De nieuwe techniek hebben wij gebruikt voor metingen aan dubbelstrengs DNA-moleculen die zich door de gefabriceerde gaten heen bewegen. Het resultaat van deze metingen wordt besproken in hoofdstuk 4. Een enkel gat scheidt twee reservoirs gevuld met geleidende bufferoplossing. Er wordt vervolgens een spanningsverschil aangelegd tussen deze twee reservoirs en de ionenstroom die door de opening vloeit wordt gemeten met een stroomversterker met hoge bandbreedte. Vervolgens wordt DNA toegevoegd aan het negatieve compartiment en zien we dat er korte verlagingen van de stroom optreden. De interpretatie is dat deze signalen worden veroorzaakt door DNA-moleculen die door de opening van het ene naar het andere reservoir bewegen. De drijvende kracht hiervoor is de elektrostatische kracht die de negatief geladen moleculen ondervinden als gevolg van het spanningsverschil. De ruimte die het DNA inneemt in de opening is niet beschikbaar voor de geleidende bufferoplossing, met als gevolg een hogere elektrische impedantie en dus een lagere ionenstroom door het gat.

Zelfs als er maar één soort DNA-moleculen aanwezig is in de

oplossing meten we verschillende signalen in de stroom door het gat. We verklaren dit effect door aan te nemen dat de DNA-moleculen met een diameter van 2 nm niet alleen lineair, maar ook gevouwen de opening kunnen passeren. Dit is mogelijk omdat de opening een diameter heeft van 10 nm en er dus voldoende ruimte is voor gevouwen DNA-moleculen. Daarnaast laten we zien dat zo'n gat ook gebruikt kan worden voor het analyseren van de lengtes van DNA-fragmenten in een mengsel. De tijdsduur nodig voor volledige passage werd bepaald voor alle DNA-fragmenten (2000 tot 48000 baseparen (bp)). Experimenteel laten we zien dat de verblijfstijd van de moleculen schaalt met een machtwet als functie van de lengte. De exponent in deze machtwet is 1.26 ± 0.07. De gemiddelde snelheid van het DNA in het gat neemt af van ongeveer 20 mm/s voor 2000 bp tot ongeveer 8 mm/s voor 48000 bp.

In hoofdstuk 5 presenteren we een nieuw theoretisch model voor het proces waarbij DNA door een kleine opening wordt getrokken. Bij gaten zoals wij die gebruikt hebben, voltrekt dit proces zich zeer snel ten opzichte van de relaxatietijd van het DNA-polymeer. Daarom moeten we het deel van het DNA dat zich buiten het gat bevindt expliciet meenemen in het model. Het model is gebaseerd op een krachtbalans tussen de elektrostatische trekkracht en de hydrodynamische wrijving op de kluwen DNA voor de opening. Het voorspelt een schaling van de verblijfstijd met de lengte als een machtwet met exponent 1.18. Dit resultaat komt zeer goed overeen met de experimenten beschreven in hoofdstuk 4.

Het tweede onderwerp van dit proefschrift komt aan bod in hoofdstuk 6 en betreft de elektrische eigenschappen van individuele DNA-moleculen in droge toestand. Verscheidene onderzoeksgroepen hebben zich met dit vraagstuk bezig gehouden en de resultaten lopen sterk uiteen. Isolerend, halfgeleidend en metallisch gedrag van DNA is gerapporteerd in de literatuur. Wij hebben een uitgebreide set metingen verricht aan preparaten waarbij individuele moleculen zijn aangebracht tussen twee metalen elektroden op een oppervlak met een onderlinge afstand van 40 nm tot 500 nm. De aanwezigheid van DNA-moleculen tussen de elektroden is aangetoond met behulp van een atomaire kracht microscoop. In geen van de preparaten konden we een meetbare stroom detecteren door het DNA. Dit gedrag zagen we bij alle preparaten waarbij we de volgende experimentele

parameters varieerden: de samenstelling van het DNA (gemengd en poly(dG)·poly(dC)), de lengte tussen de contacten (40 tot 500 nm), het substraat (siliciumoxide en mica), het materiaal van de elektrode (goud en platina) en extern aangebrachte elektrostatische velden om lading te induceren op het DNA. We concluderen dat DNA isolerend is op deze lengteschaal. Dit resultaat beperkt de mogelijke toepassingen van DNA in moleculaire elektronica.

Het derde en laatste onderwerp "elektrochemie aan nanometerschaal elektroden" wordt behandeld in hoofdstuk 7. We hebben dergelijke nanoelektroden gefabriceerd door een dikke laag goud aan te brengen in gaten van 15 nm tot 200 nm in siliciumoxide, zodanig dat de gaten volledig gesloten zijn met het metaal. In totaal hebben we 15 verschillende elektroden elektrochemisch gekarakteriseerd. We laten zien dat de diffusie gelimiteerde elektrochemische stroom niet-lineair schaalt met de grootte van de elektrode. Dit resultaat is niet in overeenstemming met het vlakke-schijf elektrode model, dat vaak gebruikt wordt voor elektroden op nanometer-schaal. Wel kwam het resultaat van onze metingen goed overeen met berekeningen van de diffusie-gelimiteerde stroom in een geometrie die overeenkomt met onze preparaten. De parameters in dit model zijn bepaald door middel van fotografische opnamen van de preparaten gemaakt met een elektronenmicroscoop. Dit resultaat laat duidelijk zien dat de exacte geometrie van het preparaat een groot effect heeft op de elektrochemische stroom, en dat de afwezigheid van gedetailleerde informatie hierover kan leiden tot grote systematische fouten. In het bijzonder is het schatten van de grootte van een elektrode enkel uit de diffusie gelimiteerde stroom zeer onbetrouwbaar. We concluderen dat lithografisch gedefinieerde elektroden belangrijke voordelen hebben voor precieze, quantitative voltammetrie.

Arnold J. Storm
Delft, maart 2004

Nawoord

Dit proefschrift beschrijft het resultaat van zo'n vier jaar experimenteel onderzoek, eerst in de quantum transport groep (QT) van Hans Mooij, en later in de moleculaire biofysica groep (MB) van Cees Dekker. Velen hebben mij met raad en daad bijgestaan, en zonder volledigheid na te streven wil ik enkele van hen hier met name noemen.

In de eerste maanden heeft Danny Porath mij met veel enthousiasme ingewijd in de nanofabricage. Dit voorbereidende werk werd verricht in een stofvrije ruimte, gevuld met apparatuur ontwikkeld voor het maken van computerchips. Het vinden van de juiste processen is een zeer tijdrovende zaak, maar gelukkig was er altijd wel iemand te vinden voor hulp en advies. Emile van der Drift, Marc Zuiddam, Bernard Rousseeuw, Gilles Gobreau, Bert de Groot, Anja van Langen, Arnold van Run, Arjan van Zuuk en Tony Zijlstra hebben ervoor gezorgd dat de apparatuur 24 uur per dag beschikbaar was, en stonden altijd voor me klaar. Ook heb ik veel over silicium nanofabricage geleerd van onder andere Leonid Gurevich, Zhen Yao, Henk Postma, Hannes Mayer en Jeong-O Lee. Experimenteel onderzoek is onmogelijk zonder goede technici. Bram van den Ende hield het 'Ultra Technical System' draaiende en was altijd bereid mijn samples te bonden. In MB was Dick Korbee een goede hulp bij het ontwerpen en bouwen van mijn experimentele opstelling. Het werken met biomoleculen vereist vaardigheden die (nog) geen deel uit maken van het natuurkunde onderwijs. Simon de Vries en later Nynke Dekker hebben me de nodige basiskennis biologie bijgebracht, en analisten Esengül Yildirim en Peter Veenhuizen hebben bijgedragen met, onder andere, mooie zuivere DNA-oplossingen.

De samenwerking met John van Noort heb ik als zeer plezierig ervaren. Dankzij zijn ervaring met het afbeelden van DNA-moleculen kwam het onderzoek in een stroomversnelling. Ook denk ik met veel plezier terug aan onze trip naar Yosemite National Park in California, na afloop van de Biophysical Society meeting in San Francisco. Met Nathan Kemeling heb ik vele uren doorgebracht in de cleanroom. In de veel te warme meetkelder van QT hebben we samen wonderbaarlijke metingen verricht aan de DNA-samples. Alhoewel de resultaten niet zijn opgenomen in dit proefschrift, wil ik Marko Dorrestijn bedanken voor zijn experimenten aan DNA-cluster interacties.

Een belangrijk keerpunt in mijn onderzoek dank ik aan Henny Zandbergen. We ontdekten dat een elektronenmicroscoop gebruikt kon worden om gaten die aanvankelijk te groot waren voor mijn experimenten, zeer gecontroleerd te verkleinen. Samen met Jianghua Chen hebben we deze techniek veelvuldig toegepast, en hebben we menig uurtje achter de microscoop doorgebracht. Ook Paul Alkemade wil ik hier bedanken voor zijn hulp bij het prepareren van zeer dunne siliciumoxide membranen met zijn focussed ion beam. De vele gigabytes aan filmpjes van krimpende gaatjes zijn vakkundig bewerkt door Jouk Jansen.

De fijne kneepjes van het werken met de nano-gaatjes heb ik geleerd tijdens mijn bezoekje aan Harvard University. De groepen van Branton en Golovchenko waren zeer gastvrij en stonden een kijkje in de keuken van de pioniers op dit gebied toe. Met name Derek Stein, die later naar MB is gekomen, wil ik hartelijk bedanken voor het demonstreren van zijn technieken, en het beantwoorden van mijn lange lijst vragen.

Ik heb het genoegen gehad om samen te mogen werken met Sean Ling. Zijn analytisch vermogen heeft geleid tot een gedetailleerd begrip van het glasblazen op nanoschaal, en zijn enthousiasme voor de natuurkunde werkte bij meer zeer aanstekelijk. Ook heb ik met veel plezier samengewerkt met Serge Lemay en afstudeerstudent Dennis van den Broek om nanoelektroden te maken voor elektrochemie.

Het onderzoek zat niet altijd mee, maar gelukkig waren er mijn ouders, mijn vrienden en natuurlijk mijn lieve vrouw Sandra om me door de beruchte OIO-dips heen te helpen.

Niet in de laatste plaats wil ik drie ‘Kezen’ bedanken, die alledrie een belangrijke rol hebben gespeeld de afgelopen jaren. Allereerst

mijn promotor Cees Dekker, die met zijn goede neus voor talent een zeer stimulerende groep wetenschappers bijeen heeft gebracht. Ik ben hem dankbaar dat ik daar de afgelopen jaren deel van mocht uitmaken. Tijdens het onderzoek heb ik veel vrijheid gekregen, en ik wil hem bedanken voor de mogelijkheid om mijn eigen weg te vinden. Ten tweede wil ik mijn broer Kees bedanken. Niet alleen heeft hij een belangrijke bijdrage geleverd aan de interpretatie van de experimentele data, ook bij het schrijven van dit proefschift heb ik veel steun aan hem gehad. Grote delen tekst heeft hij doorgenomen en voorzien van commentaar en adviezen. Als laatste wil ik mijn zoontje Kees bedanken, die me thuis altijd opwachtte met een lach en vrolijk gebrabbel.

Arnold J. Storm
Leiden, maart 2004

List of publications

- A. J. Storm, J. H. Chen, X. S. Ling, H. W. Zandbergen, and C. Dekker *Fabrication of solid-state nanopores with single-nanometre precision.* Nature Materials **2**, 537 (2003)
- A. J. Storm, S. J. T. van Noort, S. de Vries and C. Dekker *Insulating behavior for DNA molecules between nanoelectrodes at the 100 nm length scale.* Applied Physics Letters **79**, 3881-3883 (2001)
- A. J. Storm, W. A. Bosch, M. J. de Groot, R. Jochemsen, F. Mathu, and G. Nieuwenhuys, *A New Superconducting Reference Device for Thermometry below 1000 mK.* Physica B **284**, 2008-2009 (2000).
- P. Mohandas, D. I. Head, R. L. Rusby, G. Schuster, A. Hoffman, D. Hechtfischer, B. Fellmuth, P. Strehlow, L. Pitre, Y. Hermier, G. Bonnier, M. J. de Groot, A. J. Storm, R. Jochemsen, G. J. Nieuwenhuys, W. Bosch, and A. Forbes *A European ultralow temperature scale.* Physica B **284**, 2004-2005 (2000).
- M. E. W. Eggenkamp, V. A. Shvarts, R. Blaauwgeers, A. J. Storm, R. Jochemsen, G. Frossati, *On the possibility of observing third sound on ^{3}He.* Journal of Low Temperature Physics **110**, 299-304 (1998).
- A. J. Storm en H. W. Zandbergen. Patent 1022855 submitted. 'Werkwijze en inrichting voor het gecontroleerd vervaardigen van openingen op nanometerschaal.'

Publications based on chapters 3,4,5,7 are in preparation.

Curriculum vitae

Arnoldus Jan Storm

3 dec. 1974	Born in Groenlo, the Netherlands.
1987 - 1993	Atheneum at the 'Erasmus College' in Zoetermeer.
1993 - 1998	M.Sc. in physics at Leiden University. Undergraduate research in the low-temperature physics group of prof.dr. G. Frossati. Subject: Search for superconducting fixed points for the new ultra-low temperature scale
1998 - 1999	Scientist at the 'Nederlands Meetinstituut', the Dutch standards laboratory, in their 'Temperature and Radiation' section. A calibration facility for contact thermometers in the 15 mK to 1 K range was realized. It was used to evaluate prototypes of a newly developed superconducting reference device for dissemination of a new low-temperature scale.
1999 - 2004	Ph.D. research at the Delft University of Technology in the Molecular Biophysics group of prof.dr. C. Dekker. Subject: Single-molecule experiments on DNA using novel silicon nanostructures.